UNIVERSITY OF COPENHAGEN
FACULTY OF SCIENCE

Master's Thesis

Improvements in Simulation Based Reconstruction for Neutrino Telescopes

Low-energy reconstruction in the IceCube Upgrade using DirectReco

Jonathan Jegstrup

Supervisor: D. Jason Koskinen
Co-Supervisor: Tom Stuttard

Submitted: May 20, 2021

Abstract

The IceCube Observatory is a large neutrino detector buried in the ice at the South Pole. It will soon deploy an upgrade to the current detector array, The IceCube Upgrade, which will enhance the current detectors ability to study low energy neutrinos by use of its denser instrumentation and the new multi-PMT optical modules. Precise reconstruction methods are needed for the IceCube Upgrade in order to fully take advantage of the improved sensitivity. Currently, the operating reconstruction methods in IceCube do not work for the Upgrade due to the new multi directional photon sensors. DirectReco is a likelihood based reconstruction method that produces event hypothesis by direct simulation, and can be an option for reconstruction in the Upgrade.

This work aims to help improve DirectReco to work for the IceCube Upgrade and low energy reconstructions. DirectReco was improved by the change of its photon acceptance method to now work for multi-PMT modules. DirectReco was tested on electron cascades in a detector emulating the Upgrade detector with one of the new optical modules. The testing showed problems in the minimizer movement as well as a bimodality in the minimizer iterations, with larger iterations showing better performance. A reconstruction of electrons was done with 915 events, with ranging energies between 10 GeV to 50 GeV. Taking the high iteration population, the upper 1σ bound for the vertex position was 3.3 m from the truth, with z having less than 1 m. For the energy ratio of reconstruction to truth, the upper bound was 0.65. For the zenith angle it was 0.5 rad and the azimuth angle 1.8 rad. The ratio of events that did better than the seed was worst for the azimuth angle at 0.622 and best for z with 0.940. DirectReco is expected to get improved results, if the former mentioned issues can be resolved. Comparison to current reconstructions is not possible since non of the other analysis level reconstruction methods work for the Upgrade.

Authors Contributions

My contributions for this thesis was mainly in the aid of developing the DirectReco reconstruction for the IceCube Upgrade, which includes everything presented in Section 8. This includes the method for calculating the light yield in the multi-PMT optical modules in DirectReco, the implementation of hole ice in DirectReco and I introduced log binning in DirectReco which improved the stability of the energy likelihood space. I did initial investigations into the bimodality of the nmini distribution and the premature termination of the minimizer presented in section 8.2.5 and 8.2.4. I tested several parameters in DirectReco which showed no improvement in the performance or fixed the two issues. I made a reconstruction run with 915 events and analysed them in Section 8.3.2.

Separate from DirectReco I modified the GCD files to create custom detectors, explained in Section 7.1 and implemented a more realistic D-Egg wavelength acceptance curve into simulation seen in Section 7.2.

Not part of the write up of this thesis, I constructed a simulation chain without noise generation from which 50 000 noiseless electron events were generated to be used by Linea Hedemark in her mDOM noise analysis.

Acknowledgements

This has been a tough year of working mostly from home, but even so, I have greatly enjoyed the 9 months I have spend with the IceCube group at NBI. I have learned a lot about what it is like to work in a big collaboration, I have learned tons about the interesting science of experimental particle physics which I had very limited knowledge about before starting, and I have gotten the experience of being part of an incredible group.

I would like to thank Jason who gave me the opportunity to be part of this group, answered my many questions about particle physics and helped me navigating my way through this project.

I would also like to thank Tom, who has been a great help with guiding me through the jungle of the IceCube software, as well as giving tons of ideas for pushing the project forwards.

A thanks goes out to to the two other master students, Sofus and Kasper, whom I have shared an office with and with whom I shared the collective experience of writing a thesis with. A special thanks to Kasper for the many talks we have had about simulation and reconstructions when everything was getting too complicated.

Thanks to Tania for organizing the junior journal club, which provided a space for less formal talk as well as a place to hear about any new and interesting topics in science. Tania also gave us cake on the day of hand in, which was greatly appreciated.

The always cheery mood of both Kathrine and Tania kept the spirits high, especially when the hand in date was nearing, so a big thanks for that.

A collected thanks goes out to the whole of the group, including Markus, James, Linnea and Étienne, for without everyone, this experience would not have been the same. The few social activities we have had, have been great, and I wish we could have had more.

Contents

1 Introduction

Neutrinos are some of the most abundant particles in our universe, with more trillions of them going through our bodies every second [1]. They are created from many different sources, ranging from supernova explosions of dying stars to radioactive decay in the earth. But even though they are abundant, they have proven to very elusive, evading observation until 1956 where they were first observed [2]. Neutrinos rarely interact, and as such, observing them has proven to be extremely difficult.

For this reason, detectors have been built that try to increase the amount of neutrino interactions in their inner detector volumes by making the detectors huge. One such detector is the IceCube Observatory. It is a neutrino detector which is buried deep into the ice on the Southern Ice Pole. The detector uses photomultiplier tubes in order to capture the light being emitted by the secondary particles produced when a neutrino interacts with the ice particles. A small section of IceCube is called DeepCore which has a denser instrumentation than the rest of IceCube, allowing it to observe low energy neutrinos down to 10 GeV [3]. To lower the energy sensitivity even more, an upgrade to the current IceCube detector is planned which will install even denser instrumentation, more advanced optical modules and calibration devices in the ice. The ability to observe low energy neutrinos is important because it makes it possible to study one of the neutrino's weirdest attributes, neutrino oscillation. As neutrinos travel from their source, they have a probability of having changed their flavor to one of the other two existing neutrino flavors when observed. Unfortunately, it is not easy to know if a neutrino has interacted in the detector. All the detector sees is light, which can come from many different sources, most of which are atmospheric muons in the case of IceCube. To be able to understand what emitted the light in the detector, one has to reconstruct the particles from the observed light. Reconstruction of particles aim to extract the type of particle, energy, which direction the particle came from, the position at which it interacted, and more, just from the observed light in the detector.

My work tries to aid in the development of one such algorithm, called DirectReco. Specifically, my focus was on the IceCube Upgrade reconstruction using DirectReco.

In Section 2, I will introduce neutrinos in more detail, in Section 3 I will describe some of the important processes that leads to the observation of the neutrino in the detector. Section 4 will describe the IceCube Observatory, as well as DeepCore and the IceCube Upgrade. In Section 5 the Monte-Carlo simulation used for the analysis will be explained and in Section 6 reconstruction will be explained with a focus on DirectReco. The analysis

starts with some smaller projects, some of which were also used for the main analysis, and will be presented in Section 7 while the main analysis into DirectReco will be presented in Section 8. The main analysis section, will also include the results of a DirectReco reconstruction of 915 electron events in the energy range 10-50 GeV, and some future prospects. Finally, Section 9 will be for concluding remarks.

2 Neutrinos

2.1 History

The existence of the neutrino was first proposed by Wolfgang Pauli in December 1930 [4]. It was a letter to participants of a nuclear conference, that he could not himself attend. In his letter, he shares his idea of a new particle, that had never been observed, with non-zero mass, neutral electric charge and with a spin of 1/2. The idea sprang from a problem that was troubling physicists at the time. When observing β-decay the experiments did not agree with the theory. It was expected that a nucleus under β-decay, would result in a secondary nucleus differing from the original by 1 charge unit, and either an electron or positron, depending on the change of charge of the nucleus, described as the process

$$(A, Z) \rightarrow (A, Z \pm 1) + e^{\mp}, \tag{2.1}$$

where A is the mass number and Z the atomic number. The expected kinetic energy of the electron would then be well defined as $E_{k,e} = M_i - M_f - m_e$, where M_i is the initial mass of the nucleus, M_f, the final state nucleus mass and m_e the mass of the electron. But when observing the kinetic energy of an electron emitted from a β-decay, they did not measure the expected discrete energy but rather a continues β-spectra with a maximum energy of $E_{k,e}$. This energy discrepancy seemed to violate the law of conservation of energy. This is when Pauli very cautiously proposes his bold idea, that an never observed particle might exist

> *I admit that my remedy may seem almost improbable because one probably would have seen those neutrons*[1]*, if they exist, for a long time. But nothing ventured, nothing gained [...]* [5]

Enrico Fermi then proposed a model in 1934, which could successfully explain the spectra of electrons, or positrons, observed in the beta-decay [6]. The beta-decay is now understood as,

$$n \rightarrow p + e^- + \bar{\nu}_e, \tag{2.2}$$
$$A(Z, N) \rightarrow A(Z + 1, N - 1) + e^- + \bar{\nu}_e, \tag{2.3}$$
$$A(Z, N) \rightarrow A(Z - 1, N + 1) + e^+ + \nu_e, \tag{2.4}$$

[1] Pauli called these particles neutrons. They would later be called neutrinos, and the neutral nucleon particle would take the name, neutron.

and it could predict the inverse beta-decay

$$\bar{\nu_e} + p \rightarrow e^+ + n, \tag{2.5}$$
$$\nu_e + n \rightarrow e^- + p. \tag{2.6}$$

The first detection of neutrinos took several more years, but in July 1956 Clyde Cowan, Frederick Reines, Francis B. "Kiko" Harrison, Herald W. Kruse, and Austin D. McGuire, published their paper in which they finally confirmed the detection of neutrinos [2].

2.2 Neutrinos in the Standard Model

Neutrinos are elementary particles of the Standard Model (see Fig. 2.1). The Standard Model is a theory used in particle physics which describes all known elementary particles as well as three of the four known forces. It can be divided into two main classes, *elementary bosons* and *elementary fermions*.

Of the 5 elementary bosons there are the three force mediating particles called the Gauge bosons with a spin of 1, and then there is the Higgs boson with a spin of 0. The Higgs particle is the excitation of the Higgs field that gives mass to the elementary particles. It was observed for the first time in 2012 in the Large Hadron Collider [7].
The gauge bosons, also known as the force carriers, are the particles that are responsible for the three forces, *the strong force*, *the weak force*, and *the electromagnetic force*. Particularly the photon is the mediating particle for the electromagnetic interactions, the gluon is the particle mediating the strong interaction and the Z and $W^{\pm}$ bosons are the mediating particles for the weak interactions. In an interaction, the particles will exchange these gauge bosons resulting in the three forces as we know them.

The Standard Model also describes the antiparticles. An antiparticle is a particle with the same mass but with a opposite charge of its corresponding particle. For example, the elementary fermions consists of 12 particles and 12 antiparticles[2].

The fermions can be divided into six *quarks* and six *leptons*. Quarks have both color charge and electric charge. Combinations of specific quarks are what makes up all hadrons. The semi-stable combination of three quarks make up the baryons. Two up quarks and one down quark can combine to make a proton, and two down quarks and one up quark can combine to make a neutron. To make mesons an equal number of quarks and antiquarks

[2]Here, assuming the neutrinos are not Majorana particles, and therefore their own antiparticle.

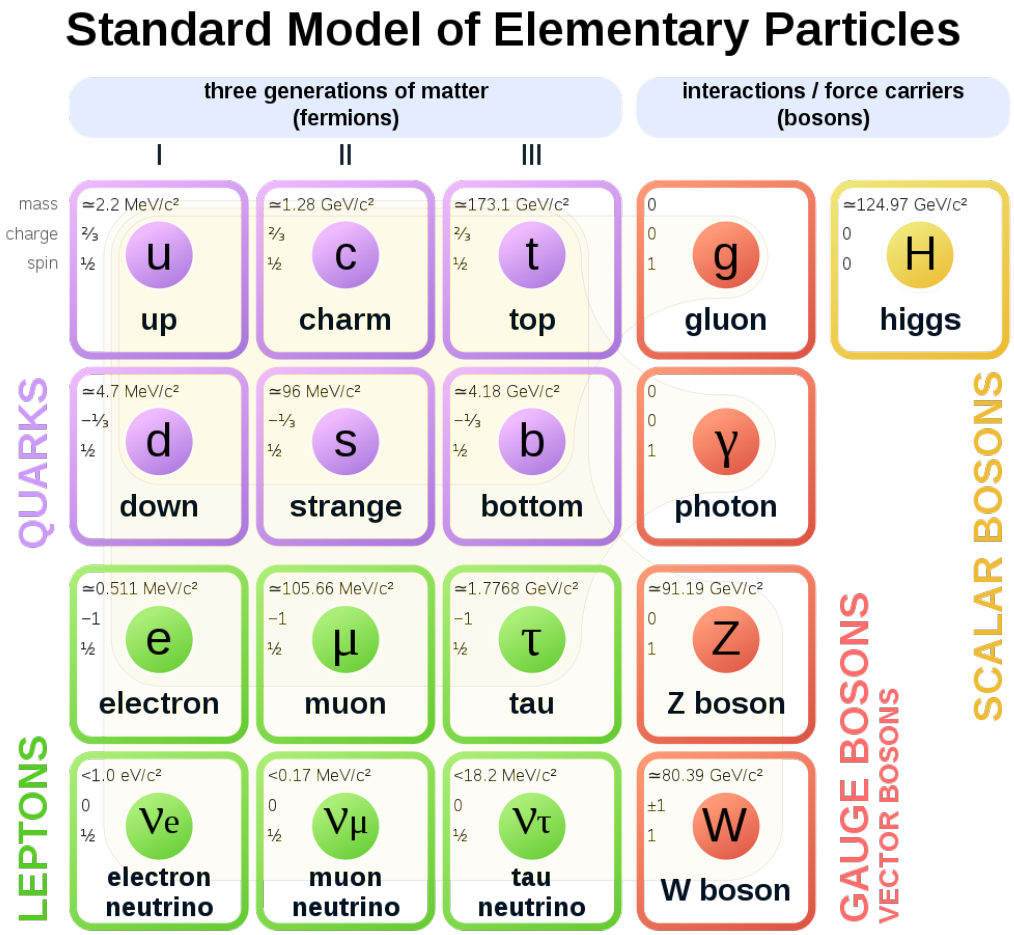

Figure 2.1: The current Standard Model. From [8]

have to combine. Because of their color charge they couple to gluons which mediate the strong force, and it is this force the holds the quarks together so they can make up the hadrons. And because of their electric charge, they couple to photons, which mediate the electromagnetic force.

The leptons have no color charge, but three of them have electric charge. The leptons consists of the three charged particles, the electron e^-, the muon μ^- and the tau τ^-, and the corresponding three neutral neutrinos, the electron neutrino ν_e, the muon neutrino ν_μ and the tau neutrino ν_τ. These leptons are divided into generations, such that the electron and electron neutrino are in the same generation, the muon and muon neutrino are in the same, and the tau and tau neutrino are in the same generation. Part of each generation are also their corresponding antileptons. Each generation has a

quantity called the *lepton number* tied to it. For leptons these number are either 1 or 0 whereas for antileptons they are -1 or 0. As an example, the electron by itself has the lepton numbers $L_e = 1$, $L_\mu = 0$ and $L_\tau = 0$, which would be exactly the same for the electron-neutrino since they are in the same generation. The positron, the antiparticle of the electron, would have $L_e = -1$, $L_\mu = 0$ and $L_\tau = 0$. These lepton numbers are postulated to be conserved in all interactions.

The three leptons with charge couple to photons, $W^\pm$ and Z^0 bosons and therefore interact electromagnetically as well as through the weak force. Their electromagnetic interactions are clearly seen by the electrons coupling to the nucleus of atoms.

Neutrinos have neither color charge nor electric charge and therefore do not interact through the strong or electromagnetic force but they do interact through the weak force. The weak force has an incredibly small range, which means the neutrinos rarely interact. The names of the neutrino flavors are directly related to their respective charged lepton partners, and are defined by their interaction with the weak force (see Section 2.3).

All the neutrinos as well as the electron are stable particles, but the muon and the tau will decay. For the muon, and anti-muon, it decays as

$$\mu^+ \to e^+ + \nu_e + \bar{\nu}_\mu, \tag{2.7}$$
$$\mu^- \to e^- + \bar{\nu}_e + \nu_\mu, \tag{2.8}$$

which can be seen as both obeying lepton number conservation and charge conservation. The tau lepton with its larger mass has more final states that it can decay to. These decay modes, and their respective probabilities are

$$\tau^- \to \mu^- + \bar{\nu}_\mu + \nu_\tau \qquad [\sim 18\%], \tag{2.9}$$
$$\tau^- \to e^- + \bar{\nu}_e + \nu_\tau \qquad [\sim 17\%], \tag{2.10}$$
$$\tau^- \to \nu_\tau + X \qquad [\sim 65\%], \tag{2.11}$$

where X can by any combination of hadrons that are allowed by the conservation laws.

2.3 Neutrino Interactions

Neutrinos are extremely elusive particles. They only interact through the weak force and can therefore travel large distances through matter without interacting. This makes them good cosmic messengers as they are not affected by magnetic fields like charged particles and therefore travel in straight lines in space-time, and unlike photons, neutrinos are rarely absorbed in gas

clouds since they rarely interact with matter. Unfortunately, when we wish to observe the neutrinos, these attributes works against us. We must rely on the small chance that the neutrinos interact in the detectors that are built. Fortunately, neutrinos are very abundant in our universe, with a flux of the order $\sim 10^{11}\,\mathrm{cm}^{-2}\mathrm{s}^{-1}$ that reach the earth every seconds [1], which by the assumption that a human is a flat disk with a diameter of 1 m, is about 100 trillions of neutrinos that pass through our bodies.

When the elusive neutrino finally interacts it does so through the weak force, where there are 2 types of interaction exchanges. The neutrinos can either interact by an exchange of the neutral Z^0 boson, called a neutral current (NC) interaction, or by either of the charged $W^{\pm}$ bosons, called charged current (CC) interactions. These bosons are both very massive particles [9] with masses

$$M_W = 80.6\,\mathrm{GeV/c^2}, \tag{2.12}$$
$$M_Z = 91.2\,\mathrm{GeV/c^2}, \tag{2.13}$$

differing from the photon and gluon bosons which do not have mass. The dominant decays of these massive bosons leads to jets of hadrons but leptonic decays are also prevalent

$$W^+ \to \ell^+ + \nu_\ell, \tag{2.14}$$
$$W^- \to \ell^- + \bar{\nu}_\ell, \tag{2.15}$$
$$Z^0 \to \ell^+ + \ell^-, \tag{2.16}$$
$$Z^0 \to \nu_\ell + \bar{\nu}_\ell, \tag{2.17}$$

where ℓ describes the flavor of the neutrino and the type of charged lepton.

The neutral current interaction only transfers the 4-momentum between the particles, one such interaction in the general form could be

$$\nu_\ell + N \to \nu_\ell + X, \tag{2.18}$$

where N is a nucleon and X is any set of hadrons allowed by the conservation laws.This can be seen with a neutral current interaction with deuterium

$$\nu_\ell + d \to \nu_\ell + p + n, \tag{2.19}$$

where ν_ℓ is any neutrino flavor, d is a deuterium and p and n are protons and neutrons. For a charged current interaction, this reaction would result in a charge exchange, such as

$$\nu_e + d \to e^- + p + p. \tag{2.20}$$

2.4 Helicity and Chirality

Helicity and chirality are two closely related quantities of a particle that are described with handedness. The helicity of a particle is a description of the relation between a particles momentum and its spin. If the spin of the particle is aligned with the direction of the momentum then the particle is right handed, if the spin is not aligned, then it is left handed (see Fig. 2.2). For any massless particle its helicty is Lorentz invariant. From any reference

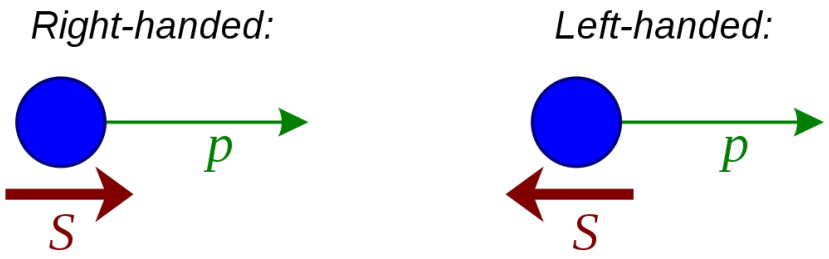

Figure 2.2: Illustration of the two possible cases of helicity. From [10]

frame, the particle's helicity is the same, though this is not inherently true for all particles. A particle with mass cannot travel at the speed of light, and therefore an observer traveling faster than the particle will see the direction of momentum being opposite than for a stationary observer. This results in the two observers seeing the same particle with two different helicities.

The chirality of a particle is a quantity that is Lorentz invariant. In the limit where $v = c$ the chirality of a particle is the same as the helicity. So for massless particles, helicity and chirality is the same, but for massive particles the two are not necessarily the same. A massive particle can be right handed chiral and have left handed helicity without breaking any laws.

Before 1957, all physical phenomena was believed to symmetric under parity. That is, a physical phenomena would be identical, if the spatial coordinates where inverted at the origin. Such a transformation would invert the momentum, but would leave the spin untouched. If there was symmetry under parity, then nature should see no difference between a left handed rotation or a right handed rotation. Parity conservation, had been shown to be the case for the strong force and the electromagnetic force, but that year, Chien-Shiung Wu et al. conducted an experiment which showed that this was not true for the weak interactions [11].

In the experiment $^{60}_{27}$Co atoms were polarized to point in one direction. The cobalt atoms are unstable and will decay under the weak force so that the

cobalt becomes nickel and emits an electron and an anti-electron-neutrino. The nickel is then in an excited state and will also decay emitting two photons. So the total reaction would be

$$^{60}_{27}\mathrm{Co} \rightarrow ^{60}_{28}\mathrm{Ni} + e^- + \bar{\nu}_e + 2\gamma. \tag{2.21}$$

Since the electromagnetic force is parity invariant, the photons could be used as a control. If parity was conserved, the electrons would be measured to be emitted equally forwards and backwards, like the photons were. But the electrons were observed to only be emitted in one direction, showing that parity was indeed violated in the weak force.

After parity violation in the weak force had been established, a new theory was developed which states that weak interaction only acts on left handed chiral states of particles and on right handed chiral states of antiparticles.

2.5 Neutrino oscillations

Neutrinos were for some time believed to be massless. This belief was, in part, because neutrinos have only been observed to have left handed helicity. Since the weak force only couples to left handed chiral states, the neutrino will have left handed chirality, and for massless particles chirality and helicity is the same.

This belief that neutrinos were massless, was found to be wrong. The experiment that broadly started the discussion of neutrino masses was known as the Homestake Experiment. The aim of the experiment was to test the theory that fusion of hydrogen to helium was the source of light from the sun. From this fusion reaction, 2 electron neutrinos would also be emitted which should, in theory, be able to be observed on earth. The first results were revealed in 1968 [12] and showed only a third of the expected neutrinos. That led many people to believe that either the calculations were wrong or the experimental setup was wrong. This was the start of *The Solar Neutrino Problem*.

It took until 2001 before the reason for the missing neutrinos was finally solved [13]. The new results in 2001 showed that the total number of neutrinos of any three flavors was equal to the number of predicted electron neutrinos. It was discovered that neutrinos had changed their flavor by traveling from the core of the sun to the earth. This change of flavor is what is now called neutrino oscillations.

When neutrinos interact they do so as a neutrino flavor ν_e, ν_μ, ν_τ but as they propagate they do so in a superposition of the three definite mass

eigenstates ν_1, ν_2, ν_3. These three mass eigenstates' phases advance differently because of their different mass, which is why the probability of a neutrino interacting as a specific flavor changes over time. The relationship between the flavor eigenstates and the mass eigenstates can be expressed from the Pontecorvo-Maki-Nakagawa-Sakata (PMNS) matrix [14, 15]:

$$U = \begin{bmatrix} U_{e1} & U_{e2} & U_{e3} \\ U_{\mu 1} & U_{\mu 2} & U_{\mu 3} \\ U_{\tau 1} & U_{\tau 2} & U_{\tau 3} \end{bmatrix}, \tag{2.22}$$

$$|\nu_\alpha\rangle = \sum_i U^*_{\alpha j} |\nu_j\rangle , \tag{2.23}$$

$$|\nu_j\rangle = \sum_\alpha U_{\alpha j} |\nu_\alpha\rangle , \tag{2.24}$$

where α represents neutrino flavor and j represents mass state.

Equations 2.23 and 2.24 describe the relation for a stationary particle. Adding time evolution to the mass eigenstate, it becomes

$$|\nu_j, t\rangle = e^{-iHt} |\nu_j, 0\rangle , \tag{2.25}$$

$$= e^{-iE_j t} |\nu_j, 0\rangle , \tag{2.26}$$

written in natural units $c = h = 1$, and where H is the Hamiltonian and t is time. The energy E_j of the mass state can be described as the square root of the sum of the square of mass and momentum:

$$E_j = \sqrt{p_j^2 + m_j^2}. \tag{2.27}$$

Neutrinos have been measured to have a very low mass ($m_\nu < 1.1\,\text{eV}$)[16], so they will propagate at relativistic speeds, which allows for the assumption that $t \approx L$, with L being the length traveled. Eq. 2.27 can be simplified by binomial expansion and higher order terms can be dropped under the assumption that $m_j << p_j$, as well as the setting $p = E$, where E is the total energy of the particle. With these assumptions, and dropping the constant term $\exp(-ipL)$, Eq. 2.26 can be written as

$$|\nu_j, L\rangle = e^{-i\frac{m_j^2 L}{2E}} |\nu_j, 0\rangle , \tag{2.28}$$

describing the wavefunction of the mass eigenstate. From this equation it can be seen that the wavefunction oscillates at different speed given the mass. The flavor state from Eq. 2.23, with time evolution can then be written as

$$|\nu_\alpha, L\rangle = \sum_j U^*_{\alpha j} e^{-i\frac{m_j^2 L}{2E}} |\nu_j, 0\rangle . \tag{2.29}$$

With the flavor wavefunction it is posible to calculate the probabillity of a flavor oscillating to a different flavor after a given time t (or length travelled L) from

$$P(\nu_\alpha \to \nu_\beta) = \left|\langle \nu_\beta, 0 | \nu_\alpha, L\rangle\right|^2, \tag{2.30}$$

$$= \left(\sum_j U^*_{\alpha j} e^{-i\frac{m_j^2 L}{2E}} U_{\beta j}\right)\left(\sum_k U_{\alpha k} e^{-i\frac{m_k^2 L}{2E}} U^*_{\beta k}\right) \tag{2.31}$$

This expression can be expanded further, and using the unitarity closure relations and normalization constraints it can be written as

$$P(\nu_\alpha \to \nu_\beta) = \delta_{\alpha\beta} - 4\sum_{i<j} \Re(U^*_{\alpha i} U_{\beta i} U_{\alpha_j} U^*_{\beta j}) \sin^2\left(\frac{\Delta m^2_{ji} L}{4E}\right) + 2\sum_{i<j} \Im(U^*_{\alpha i} U_{\beta i} U_{\alpha_j} U^*_{\beta j}) \sin\left(\frac{\Delta m^2_{ji} L}{2E}\right), \tag{2.32}$$

where δ_{ji} is the Kroneckers delta and Δm^2_{ji} is the mass squared difference, $\Delta m^2_{ji} = m^2_j - m^2_i$. From this equation it is clear, that if there were no difference in neutrino mass states, there would be no oscillations. The only term contributing to the probability is $\delta_{\alpha\beta}$, which is zero for any $\alpha \neq \beta$. Neutrino oscillations have been measured multiple times [17], so neutrinos are expected to have masses. A useful reparameterization of the mixing matrix is using trigonometric functions and mixing angles. By using simplifications of the energy resolution and threshold of neutrino detectors and assuming only 3 neutrino flavor states and mass states, the probability of a muon neutrino oscillating is given by

$$P(\nu_\mu \to \nu_\mu) = 1 - 4\sin^2\theta_{23}\cos^2\theta_{13}\left(1 - \sin^2\theta_{23}\cos^2\theta_{13}\right)\sin^2\left(\frac{\Delta m^2_{32} L}{4E}\right), \tag{2.33}$$

$$P(\nu_\mu \to \nu_e) = 4\sin^2\theta_{23}\cos^2\theta_{13}\sin^2\theta_{13}\sin^2\left(\frac{\Delta m^2_{32} L}{4E}\right), \tag{2.34}$$

$$P(\nu_\mu \to \nu_\tau) = 4\sin^2\theta_{23}\cos^2\theta_{13}\cos^2\theta_{23}\cos^2\theta_{13}\sin^2\left(\frac{\Delta m^2_{32} L}{4E}\right). \tag{2.35}$$

It is worth noting that the mixing angle θ_{13} is relatively small compared to θ_{23}, which is why these expressions are often shown as functions of only θ_{23} and Δm^2_{23}. The probability of oscillating from a muon netrino to an electron neutrino is usually also very small.

3 From Creation to Detection

As described in Section 2, neutrinos interact very rarely, and only do so by interactions of the weak force. This makes the aim of observing these particles difficult. Since they cannot be observed directly, secondary particles from neutrino interactions must be studied instead, and the neutrino properties must be inferred from these. But before one can detect the neutrinos, they have to reach the detector from the many different sources that they are produced in.

3.1 Neutrino Sources

The neutrinos that arrive at earth, come from many different sources, most of which are outside of the earth. Cosmological neutrinos are relics from the early epochs of the universe, similar to the photons from the cosmic microwave background. Some neutrinos are produced in the violent supernova explosions of dying stars, when their core collapses. Our sun, and other stars, produce large amounts of neutrinos in their fusion reactions inside their core. The neutrinos that are produced inside our sun, constitutes a large part of the neutrinos flux on earth. Some highly energetic neutrinos, $E_\nu \gtrsim 10^{12}\,\text{eV}$, are called the astrophysical neutrinos, which are believed to be produced in Active Galactic Nuclei (AGN) [6].

The neutrinos which are of most importance to this thesis, are the atmospheric neutrinos. These neutrinos are produced in the earths atmosphere from interactions of cosmic rays. Cosmic rays are highly energetic protons and atomic nuclei whose origin is astrophysical sources, such as our sun, our galaxy or distant galaxies. When these cosmic rays enter the atmosphere, they interact and produce many secondary particles in particle showers, some of which are neutrinos. These neutrinos are important because when they are observed on earth, the direction of the incoming neutrino will tell us the distance in which it has traveled, and with a low enough energy, it is possible to do oscillation analysis on these neutrinos. The sensitivity of the current IceCube Observatory allows the observation of neutrinos from these atmospheric neutrinos and from astrophysical neutrinos. The flux of the many types of neutrinos, including some I did not mention, can be seen in Fig. 3.1.

3.2 Particle showers

Particle showers describe the phenomena of producing secondary particles which subsequently produce even more particles, resulting in a cascade of particles. This is either an *electromagnetic shower* or a *hadronic shower*.

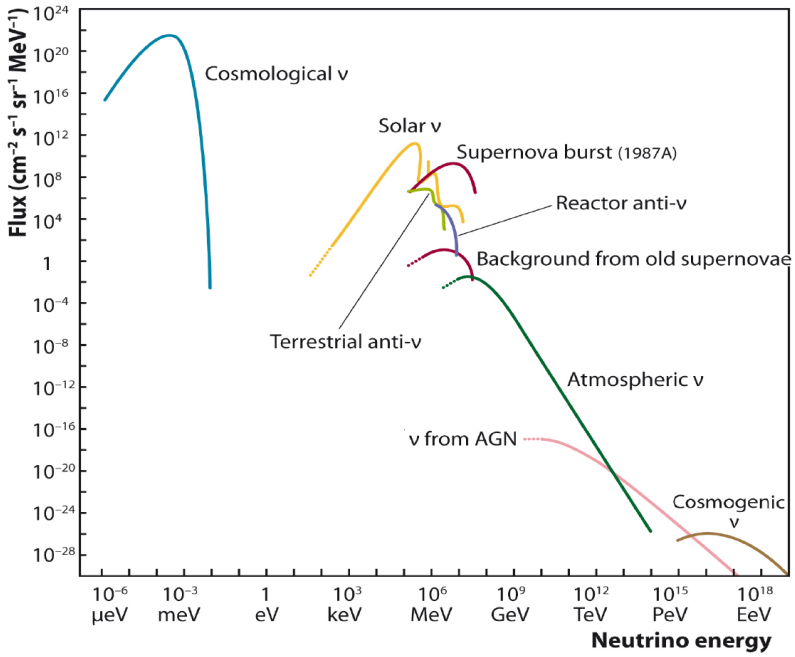

Figure 3.1: The flux of neutrinos at the Earth from different sources. From [18].

From the production of multiple particles, these secondary particles will have less energy than the initial particle, and at some point there will be no more energy for producing particles and the shower will stop.

An electromagnetic shower is the simpler of the two, and usually starts as an electron, positron or photon enters a material. When a photon interacts with matter it can produce an electron and positron pair in a process called pair production. These electrons or positrons can then subsequently emit light through Cherenkov radiation or *bremsstrahlung*[3], where bremsstrahlung describes the process of emission of electromagnetic radiation from the deceleration of a charged particle by other charged particles. If these photons are still energetic enough they can undergo pair production supporting the shower with even more electrons and positrons. An electromagnetic shower can be induced by electrons of high enough energy, for example from CC interactions with ν_e or be the product of a hadronic shower.

A hadronic shower is, as the name suggests, a shower with hadrons. At high enough energies a hadronic shower will produce multiple pions and nucleons. Particles are mostly produced in these showers through the processes of hadron production, nuclear deexcitation and pion and muon decays. Elec-

[3]Translated: "braking radiation".

tromagnetic showers can also be induced by the decay of π^0 pions into electrons and photons. Hadronic showers are frequently happening in the atmosphere when cosmic rays interact with the air, but they can also be observed as a product of a DIS interaction described in Section 3.3.

The energy deposited in the two types of showers are different and important to the detection of neutrinos, but this will be explained in further detail in Section 3.4.

3.3 Neutrino-Nucleon Interactions

From the atmospheric showers, neutrinos will be produced, some of which will interact with the nucleons in the detector medium. The type of interaction, will vary depending on the energy of the interacting neutrino. These types of interactions are generally distinguished in three types. The *quasi-elastic* (QE) or just *elastic* for NC interactions, *resonance excitation* (RES) and *deep inelastic scattering* (DIS). Each of these dynamics dominate in different energy regions, with some transition regions between the three. Figure 3.2 shows the cross sections of each type of dynamic for a given energy from CC interactions. The cross section of an interaction can, in simplified terms, be related to the probability that the interaction will occur, so the figure shows the dominating regions of each dynamic.

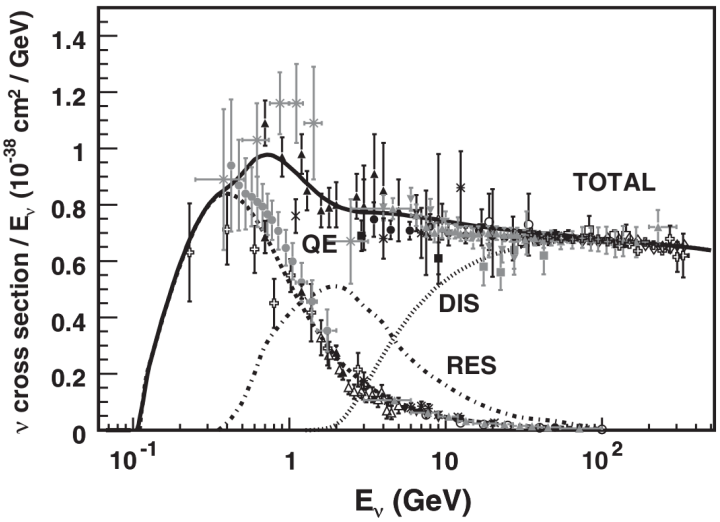

Figure 3.2: The neutrino cross section contributions divided by energy for CC interactions as a function of energy. From [19].

An elastic interaction is when the initial particles and final particles are

of the same type. These interactions will only happen with NC interactions, and one such interaction would look like $\nu_\ell N \to \nu_\ell N$. A quasi-elastic interaction is the equivalent but for CC interactions. In CC interactions, there will always be an exchange of charge so the initial particles will not remain, but the amount of particles will remain the same. One such interaction can be seen for the inverse-beta-decay in Eq. 2.5. The energy region for these type of interactions are $\lesssim 1\,\text{GeV}$.

For the resonance excitation or resonant single pion production, the neutrinos have enough energy to excite the nucleon which is involved in the interaction. The interaction will produce a baryon resonance (N^*) which will quickly decay. This decay will, most often, result in a nucleon and a single pion in the final state. An example of such interaction for a muon neutrino is

$$\nu_\mu + N \to \mu^- + N^*, \tag{3.1}$$

$$N^* \to \pi + N', \tag{3.2}$$

where N is a neutron and N' is a proton. The energy region of such interactions are $\sim 2\,\text{GeV}$.

With enough energy the neutrino can scatter off the individual quarks inside the nucleon resulting in a deep inelastic scatter interaction. The final state of the interaction will be a lepton or neutrino, depending on CC or NC, and a hadronic system. This hadronic system can be nucleons, pions, kaons as well as other mesons. These interactions will in general produce hadronic showers (see Section 3.2). The dominating region of these interactions are for energies $\gtrsim 5\,\text{GeV}$.

For particle observatories, such as the IceCube Observatory, the relevant energy regions are usually above 10 GeV, which means that the DIS reactions are dominant. For oscillation analysis, where low energy neutrinos are of interest, the neutrinos studied, rarely go below the dominating region of the DIS interactions.

3.4 Cherenkov Radiation

When the neutrinos finally interact with a nucleon in the detector medium, a particle shower will be induced from the DIS reaction. These secondary particles can be observed by their emission of Cherenkov radiation.

As a charged particle travels through a dielectric medium at a speed larger than the phase velocity of light in that medium, electromagnetic radiation

will be emitted. This is usually visible in nuclear reactors submerged in water where charged particles are emitted at large speeds, and the radiation can be seen as blue light coming from the water, but the radiation can also be used as an observational tool for these kinds of particles.

As the charged particle travels through the dielectric medium, it will polarize the atoms to be aligned in the direction of the traveling particle and it will excite the molecules to higher states, which will then subsequently return to their ground state, emitting photons. These photons will primarily be in the wavelengths of blue light. The wavefronts of the photons will be spherical and propagate at the phase velocity of the medium. If the speed of the particle is less than the phase velocity of the medium then the wavefronts can be seen to bunch up towards the direction of travel of the particle. If the particle is traveling at speeds larger than the phase velocity of the medium, the wavefronts will coincide and cause constructive interference resulting in what looks like a cone-like light emission trailing the traveling particle. An illustration of this can be seen in Fig. 3.3.

The angle of emission for this can be calculated using simple trigonometry, resulting in

$$\cos\theta = \frac{1}{n\beta}, \tag{3.3}$$

where n is the refractive index of the material and the β is the ratio between the particle speed and the speed of light in a vacuum.

Cherenkov light can be used successfully to observe charged particles and because of that, large detectors have been built to detect particles in this way. Examples are the Super-Kamiokande detector or the IceCube Observatory, which both use photo sensitive detectors called photomultiplier tubes (PMTs), to detect the light.

The amount of energy deposited can vary from the two types of showers. Electromagnetic showers will deposit most of their energy in the detector before they slow to velocities where no Cherenkov radiation is emitted, whereas hadronic showers, with their more heavier particles, will reach sub-Cherenkov velocities before depositing the same amount of energy as the electromagnetic shower. As such, inferring the initial energy of a interacting neutrino is not trivial. Even more so if the neutrino participated in a NC interaction, then it will carry much of the energy away, reducing the deposited energy even more.

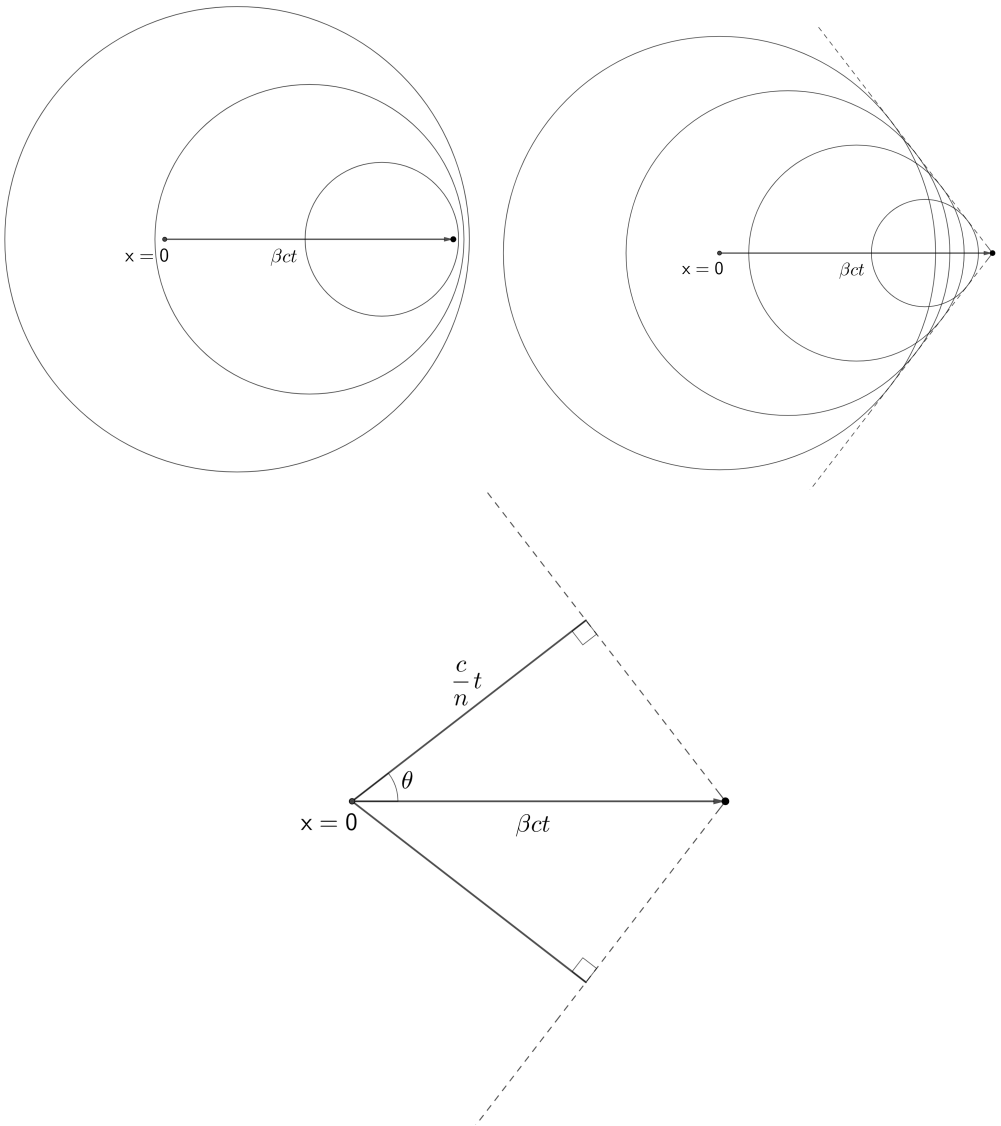

Figure 3.3: Diagrams showing Cherenkov radiation. The black arrow shows the distance traveled by the charged particle and the circles show some of the light being emitted isotropically. **Top-Left:** A charged particle traveling slower than the phase velocity of light in the medium. The light waves do not produce constructive interference, so the light is not clearly visible. **Top-Right:** A charged particle traveling faster than the phase velocity of light in the medium. The waves overlap to produce constructive interference seen as a wave propagating behind the particle. **Bottom** The trigonometry of the top-right plot is shown more clearly with drawn in triangles and the light waves omitted.

4 The IceCube Detector

The IceCube Neutrino Observatory is a cubic-kilometer particle detector buried deep into the ice at the South Pole close to Amundsen-Scott Pole Station. The IceCube detector consists of two parts, the IceTop array situated at the surface of the ice and the IceCube array extending to around 2500 meters below the surface, including the more dense region of the detector called DeepCore (for more about DeepCore, see Section 4.3). For an illustration of IceCube, see Fig. 4.1. The primary purpose of the IceCube, is

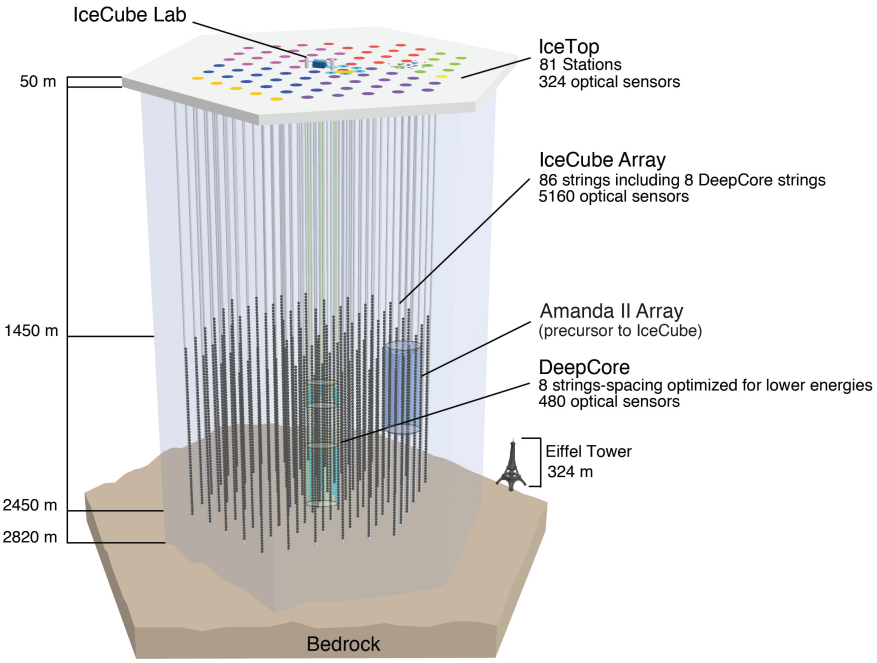

Figure 4.1: Illustration of the IceCube Neutrino Observatory

to observe high-energy neutrinos from astrophysical sources. The threshold for the main part of the array is about 100 GeV while the more dense region, DeepCore, lowers the energy threshold of IceCube to about 10 GeV, making it possible to study neutrino oscillations [20].

The in-ice IceCube array is made up of 86 strings, bored into deep into the ice. At around 1450 m to 2450 m below the surface, the strings each carry 60 Digital Optical Modules (DOMs) with 10″ PMTs (25.4 cm) and the needed electronics. For most of the strings the horizontal separation is 125 m and the vertical spacing between each DOM is 17 m.

To accommodate neutrinos' small cross sections, as well as the low flux

expected at Earth from astrophysical objects, the detector was built to be extremely large. The icecap at the South Pole is close to 3 km thick, which made it possible to build the large detector. At the depths that the DOMs are placed, there is no light pollution from the surface, and the ice has excellent optical properties making it ideal for observing the light generated in the ice from particles.

IceTop consists of 81 stations each located on top of one of the IceCube strings. Each station has two tanks, each with two downward facing DOMs. The surface array is usually used as a veto and calibration detector for IceCube as well as the detection of air-showers from cosmic rays.

The IceCube Laboratory is situated on the surface and handles all the information that is passed from the DOMs. The computers at IceCube Lab. combine this information from multiple DOMs to create the light patterns that can be used for analysis.

4.1 Digital Optical Modules

The DOMs are the fundamental detectors for capturing light in the ice. They consist of a glass housing encapsulating the photomultiplier tube (PMT) which is responsible for capturing and converting a photon into electrons. Inside the glass is also a main board, and separate circuit boards for conversion of electric signals into usable waveforms. A flasher board is also in the DOM and is used as a calibration device for a variety of purposes. In Fig. 4.2 a diagram and a picture of a DOM can be seen.

4.1.1 Photomultiplier Tube

A PMT is a vacuum tube that is sensitive to light in the ultra-violet to the near-infrared light. The light is converted into an electron, by a photocathode and is subsequently multiplied in the tube up to 10^8 times, from a sequence of dynodes. As a photon hits the photocathode area of the PMT an electron is emitted by the photoelectric effect. The electron is accelerated by an electric field in the PMT and is guided into the first of the multiple dynodes in the PMT. As the electron hits a dynode, more electrons are emitted from the material by the effect of secondary emission. These electrons are then accelerated into the next dynode. As the electrons hit the dynodes in the PMT the electrons are increased in an exponential manner. Finally the avalanche of electrons hit the anode producing a measurable signal. An illustration of this, can be seen in Fig. 4.3.

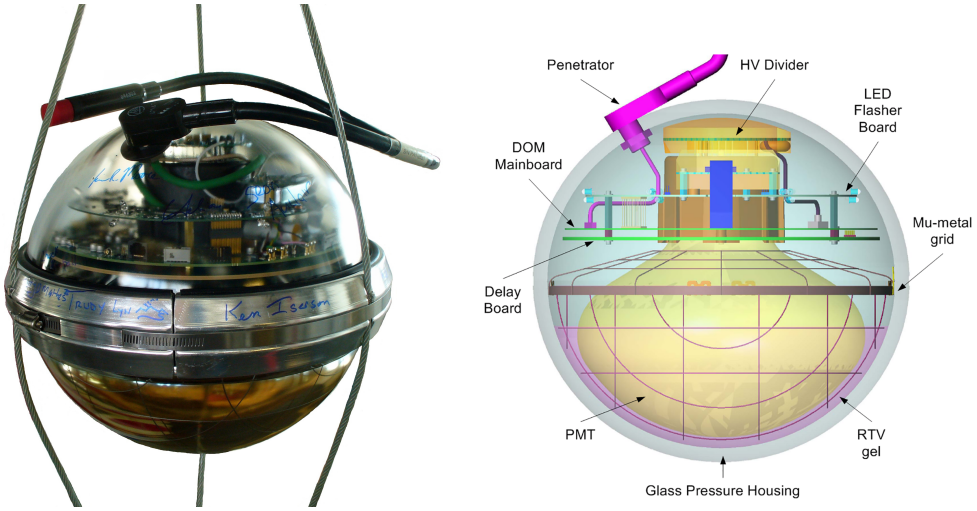

Figure 4.2: Digital Optical Modules are used in IceCube for detecting photons deep in the ice. From [21, 22].

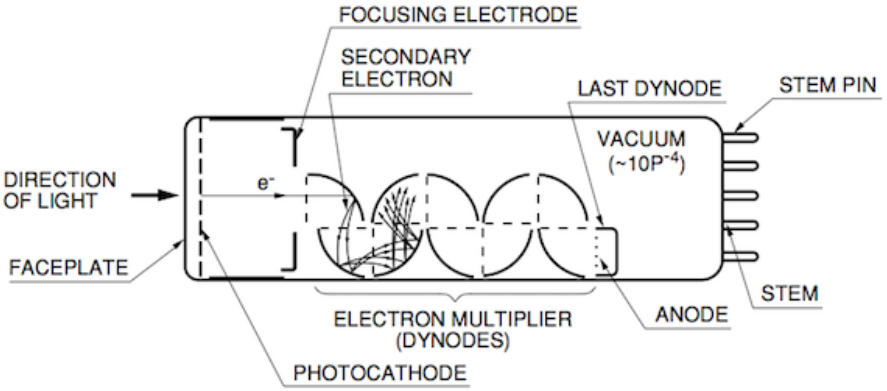

Figure 4.3: A schematic of a generic photomultiplier tube. The photomultiplier tube is used in the DOMs of IceCube to convert photons into signal. From [23].

The specific PMT used in the DOMs of the main part of the IceCube array, is the 10″ (25.4 cm) Hamamatsu R7081-02 PMT. The peak wavelength is at 400 nm, in the deep blue of the visible spectrum and a gain of 10^7, where gain is the measure of the multiplication of the initial electron [24].

4.1.2 Glass, gel and metal grid

The glass of the DOM is its protection from the environment outside. It has an outer diameter of 13″ (33.02 cm) and with a thickness of 0.5″ (1.27 cm). To reduce the noise from the glass, the amount of radioactive elements in the glass, such as potassium, were kept low. In the ice the DOMs have to

endure a pressure of around 250 bar, as well as the high pressure of around 690 bar, when the water in the borehole refreezes.

The PMT is secured in a silicone gel, which surrounds the photocathode area. The gel provides the mechanical support for the assembly of the PMT and circuit boards. It has good optical coupling and a thickness of 1 cm between the PMT and the glass housing. Good transmittance in the gel is important, so the gel is optically clear with transmission of 97% at 400 nm decreasing to 65% at 300 nm [20]. With a refractive index of 1.41, the amount of reflected light is only 0.1% from glass to PMT.

A wire mesh surrounds the PMT from the neck all around the PMT face. The mesh reduces the effects of the South Pole magnetic field by about 0.357 inside the DOM, but blocks about 4% of incident light. Without the mesh the collection efficiency of the PMT are worse by 5-10% as well as the single photoelectron resolution worsens. With the shield the reduction of efficiency is lower than 2%.

4.1.3 Local Coincidence and Cables

The DOMs have three wire pairs that penetrates the glass housing in a waterproof seal. One wire pair carries the power and bidirectional digital communication stream, which goes to the IceCube Laboratory on the surface. The other wire pairs lead to the immediate DOMs above and below. These cables are used for checking for local coincidence (LC) signals.

LC is used to see if more DOMs in its vicinity has also observed a charge pulse within some time frame. If there is LC, the pulses are recorded as Hard Local Coincidence (HLC) hits and all the charge and timing information of that recording is sent to IceCube Lab. If there is no LC, the hits are recorded as Soft Local Coincidence (SLC) and only a single timestamp and a brief charge summary is sent to the surface.

4.1.4 SPE Charge Distribution

The ideal measurement of a photon is the scenario of a photon hitting the PMT cathode initiating the electron avalanche which results in a known number of electrons hitting the anode. The measured charge response could then directly be related to a photon. Unfortunately, reality is never so simple, so a single photon can result in many different charge responses. The distribution of charge response from a single photon hitting the photocathode is called the single-photoelectron (SPE) charge distribution. The effects that result in the varying measured charge distributions are described in [25], some of them which can be seen here:

- **Statistical fluctuation due to cascade multiplication:** As a electron hits a dynode the amount of multiplication is randomly distributed, which in turn, results in a randomly distributed amount of electrons hitting the anode. This will cause the charge response to be smeared by some amount.

- **Photoelectron trajectory:** The electrons might miss a dynode as they are propagated through the PMT, which will show as less charge response. The largest effect is seen if the electron misses the first dynode after being emitted from the photocathode.

- **Late or delayed pulses:** An electron has a probability of backscattering off the dynode either elastically or inelastically. The electron will then be accelerated toward the dynode once again. If it scattered elastically, it will carry the full energy and the multiplication will be the same as had it not scattered, while the inelastic scatter will have less energy and therefore produce less electrons when it hits the dynode. The time difference of a backscattered electron has been measured to be up to 70 ns [26].

- **Afterpulses:** PMTs have a high vacuum, but the residual gas can be ionized by the electrons, if they have sufficient energy. The positively charged ionized gas will then be accelerated by the electric field towards the photocathode. When the positively charged particles hit the photocathode it can result in electrons being emitted, initiating another electron cascade. The timescale of afterpulses are measured to be from 0.3 to 11 μs after the initial pulse [26].

- **Pre-pulses:** A photon can pass through the photocathode without ejecting any electrons, and hit a dynode, whereby ejecting an electron. The electron will then only be amplified by the subsequent dynodes, resulting in a lower measured charge response than a regular pulse charge by a factor of around 10 to 20. They arrive approximately at around 30 ns before regular photoelectrons emitted from the photcathode.

- **Dark noise:** Photoelectron emission without an external source. It is described in more detail in section 4.1.5.

- **Electronic noise:** There is a small contribution to the charge noise from electronics, such as the analog-frontend and the analog-to-digital converters. It only leads to a small broadening in the low charge region.

The above effects are modelled using the sum of two exponential distributions and a gaussian distribution. This model is called the SPE charge template, and has the form:

$$f(q)_{SPE} = \frac{P_{e1}}{w_1} e^{-q/w_1} + \frac{P_{e2}}{w_2} e^{-q/w_2} + \frac{1 - P_{e1} - P_{e2}}{\sigma\sqrt{(\pi/2)}\mathrm{Erfc}[-\mu/(\sigma\sqrt{2})]} e^{-\frac{(q-\mu)^2}{2\sigma^2}}, \quad (4.1)$$

where q represents the measured charge, w_1 and w_2 is the exponential decay widths and μ, σ is the mean and the standard deviation of the Gaussian. The Erfc function is used to normalize the Gaussian. P_{e1}, P_{e2} and $1 - P_{e1} - P_{e2}$ describe the probabilities of a photoelectron contributing to each of the components in the SPE template. The specific values of these parameters were calibrated in-situ and can be seen in Table 1. in [25].

The DOMs have an onboard discriminator which only triggers if the photoelectrons that hit the anode produce enough charge, initiating the signal acquisition process. This discriminator is set to approximately 1.2 mV ($\sim$ 0.23 PE), to eliminate most of the electronic noise.

4.1.5 Dark Noise

Dark noise is noise that come from effects that lead to emission of an electron from the photocathode, without being hit by an external photon from outside the DOM. The dark noise can come from numerous sources, like thermionic emission, which is an emission of a electron by a heated cathode, Cherenkov light from radioactive decay and scintillation in the glass of the PMT and pressure sphere.

The dark noise can be characterized by uncorrelated Poisson noise pulses with rates from 230 Hz to 250 Hz and a correlated noise component with a rate of 280 Hz to 340 Hz [20, 27]. A dependence on the temperature was found for the noise rates, and the ranges of the pulse rates are determined in a temperature range of $-30\,°\mathrm{C}$ to around $-10\,°\mathrm{C}$, which corresponds to the change in temperature for the difference in depths that the DOMs are placed, measured on the DOM mainboard.

The dark noise which occur at small time-intervals are clustered in bursts, where hits therein are highly time correlated. Measurements of this noise shows it to be consistent with the spontaneous electron emission investigated in [28], in which they also show an increase in noise rate with lower temperatures. The exact reason for this noise is not known, but a likely candidate is scintillation in the glass, triggered by the decay of ^{40}K and other radioactive elements in the pressure sphere.

4.2 Ice Properties

The Antarctic Muon and Neutrino Detector Array (AMANDA) was the detector buried in the South Pole ice before IceCube and was its predecessor [29]. With AMANDA the ice properties, absorption and scattering, were measured at different wavelengths and depths down to about 2350 m. This model was called the AHA ice model. The ice properties were found to correlate well with climatological history. Part of the ice layer contains large amounts of dust, lowering the absorption and scattering lengths, at around depths between 2000 to 2100 m, and is generally denoted the "dust layer". It corresponds with a stadial about 65,000 years ago. The measured ice properties can be seen in Fig. 4.4.

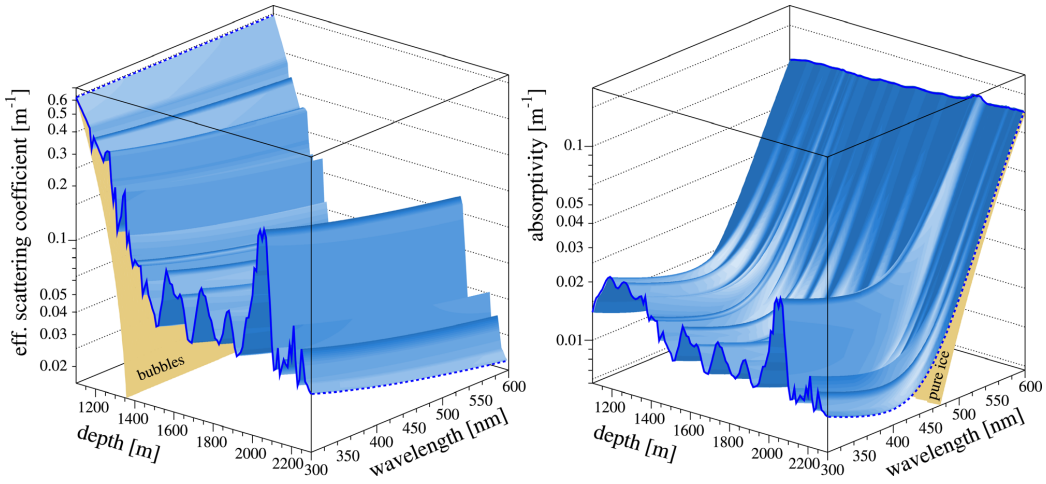

Figure 4.4: The ice properties measured by AMANDA. It shows the ice properties' dependence on depth and wavelengths. **Left:** Shows the effective scattering coeffecient. The dashed line at 2300 m shows the wavelength dependence as a power law due to dust. The dashed line at 1100 m shows that the scattering on bubbles is independent of wavelength. **Right:** The dashed line at 2300 m shows the wavelength contributions of two components, a power law due to dust and an exponential due to the ice. The slope of the solid line at 600 nm is caused by the temperature dependence of intrinsic ice absorption. From [30]

This has later been updated in-situ with the deployed IceCube detector. These measurements showed similar ice properties as AMANDA had previously measured but with small changes and much more precise result. This model is called the SPICE MIE model. The two models agree that at lower depth, both the absorption and scattering lengths are longer, and so the ice is clearer. In general, the SPICE MIE model shows increased absorption in the dust layer, and shows less scattering at larger depths, than the previous AHA model. For more specifics about the SPICE MIE ice model, see [31].

4.2.1 Hole ice

When the DOMs were lowered into the ice in the bore-holes, a camera system was deployed on string 80 in order to monitor the freeze-in process and the optical properties of the bore-hole. Two video cameras, each housed in their own pressure sphere were deployed between the bottom DOM and the string weight. They were each equipped with 4 LED lamps and three lasers. Using this system, it was observed that the drill holes were completely refrozen after 15 days. The ice was observed to freeze from the outer sides of the hole and inwards. This resulted in a clear outer layer and a central core of about 16 cm diameter with a much smaller scattering length than the bulk ice, as a result from the condensed impurities such as air bubbles and dust being pushed inwards. This is aptly named the "bubble column", and the ice is usually referred to as the hole ice.

4.3 DeepCore

DeepCore is a subarray of the IceCube observatory, which purpose was to improve sensitivity to neutrinos at lower energies than the bulk of the detector was intended to [3]. This improved sensitivity comes from the placement of the DOMs in the ice, better sensitivity of PMTs and the more dense geometry of the DOMs and strings. The improved sensitivity makes it possible to observe low energy atmospheric neutrinos at $E_\nu \gtrsim 10\,\text{GeV}$, which gives rise to the opportunity of oscillation analysis, ν_μ disappearance and ν_τ appearance.

DeepCore consists of 8 strings placed close to the middle of the bulk detector in the horizontal plane and has a DOM to DOM spacing between 7 to 10 m. DeepCore is separated in two parts at the depth of 2100 m. A small part is above the dust layer and has 80 DOMs with 10 m spacing between each DOM on a string. The rest of DeepCore is situated below the dust layer at depth between 2100 to 2450 m, and consists of 400 DOMs with 7 meters spacing between DOMs on the strings. The largest part of DeepCore is placed so deep to exploit the the optical properties of the ice at these lower depths. The ice is described in more detail in Section 4.2. A schematic of the geometry of DeepCore can be seen in Fig. 4.5.

The upper part of the DeepCore, as well as the original IceCube array, can be used as an active veto against atmospheric cosmic ray muons. At low energies the flux of atmospheric background muons is larger so having an effective veto is important.

The PMTs used in DeepCore differ from the PMTs used in the original IceCube Array. The PMTs in DeepCore are the R7081MOD, which are identical with the original PMTs except that they have an improvement of

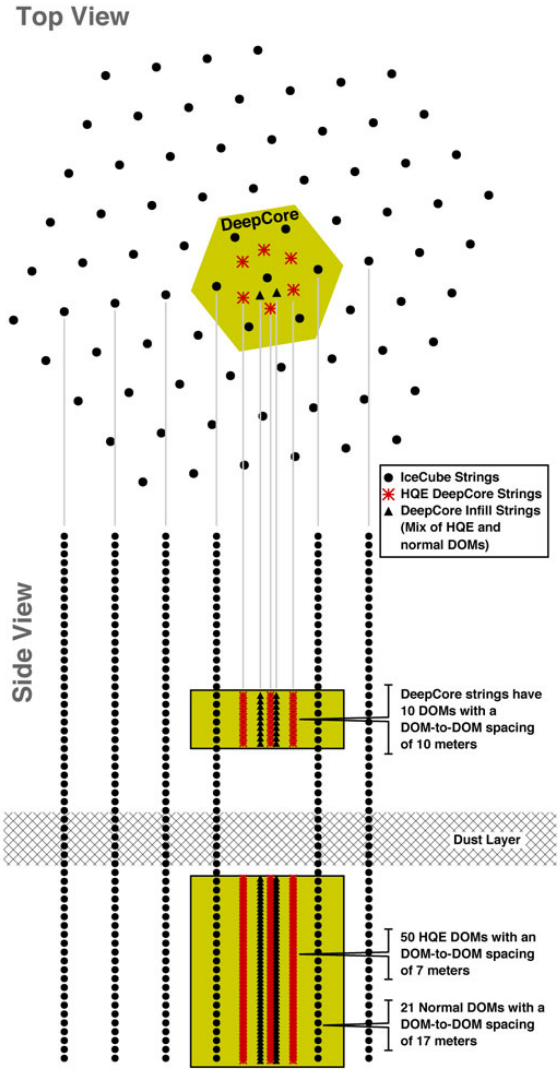

Figure 4.5: A schematic of the DeepCore layout. The upper part shows the position of the original IceCube and DeepCore strings seen from above. The bottom figure shows the depth of the DeepCore strings and DOMs as well as a few selected original IceCube strings.

40% for the quantum effeciency at photon wavelengths $\lambda = 390\,\mathrm{nm}$ reported by Hammatsu. DOMs were equipped with these higher quantum efficiency (HQE) PMTs, and subsequently tested by IceCube confirming the HQE of the PMTs. The noise rate of the HQE PMTs is also larger by around a factor of 1.33 at $-45\,^{\circ}\mathrm{C}$.

4.4 IceCube Upgrade

The IceCube Upgrade (ICU) is a planned upgrade to the current IceCube array, which aims to increase the sensitivity of the already deployed DeepCore, by deploying new optical modules with increased photon collection efficiency (see Section 4.4.1, 4.4.2), as well as giving IceCube an even denser instrumented region [32]. The ICU will make reconstructions (see Section 6) of even lower energy neutrinos more accurate than DeepCore has the potential to, and will enable more precise results of oscillation analysis. Each optical module will also include several calibration devices, including on-board pressure, temperature, magnetic field sensor, and accelerometers. Several stand alone light emitting devices will also be deployed for calibration of the glacial ice and *in-situ* detector responses. The calibration results can then be used in future analysis as well as being propagated through old archived data to obtain more accurate results.

The ICU will be deployed as 7 strings largely in between DeepCore strings, and the digital modules will be placed in depths between 2150 to 2425 m in the DeepCore region, where the ice is the clearest (see Section 4.2). The spacing between each digital modules will also be small with only 3 m, compared to the 7 m in DeepCore, and each string will have 100 optical modules.

The ICU is part of a larger improvement project to IceCube. This project is called IceCube-Gen2 and will enlarge the current IceCube array instrumenting a much larger area, as well as deploying a high-energy radio array and a surface CR detector array. The ICU is also one of the planned improvements. The ICU is significant to my thesis but the rest of the improvements are not, so I will not go into more detail about these. For more about Gen2 see [33].

4.4.1 D-Egg

One of the new digital modules that is going to be deployed in the ICU is the Dual optical sensors in an Ellipsoid Glass for Gen2 (D-Egg). The D-Egg has been optimized to increase detection efficiency for UV photons and angular acceptance at a minimum additional cost.

The D-Egg carries two 8″ (20.32 cm) Hamamatsu R5912-100 PMTs, with one looking up and one looking down (see left figure in Fig. 4.6). The D-Egg is taller than it is wide to have room for the additional PMT, making it 544 mm tall and 300 mm wide. The width of the D-Egg is therefore 30.2 mm smaller than the current DOMs. Even though the PMTs are smaller, the use of 2 opposite pointing PMTs increases the angular acceptance of the D-Egg compared with the regular DOMs, as well as giving more directional

information about the incoming photons.

The other improvement is the wavelength acceptance of photons is improved in the UV range, which is important for observing Cherenkov radiation. The thickness of the glass for the D-Egg varies, being thickest at the equator and thinning at the poles. In this way, the optical properties and the mechanical structure are both optimized.

Figure 4.6: Two of the optical modules that are planned to be used for the IceCube Upgrade. **Left:** The D-Egg consists of two 8″ (20.32 cm) PMTs, one pointing upwards and one pointing downwards. **Right:** The mDOM consists of 24 PMTs of 3″ (7.62 cm), pointing almost isotropically in all directions.

4.4.2 mDOM

The Multi-PMT optical module (mDOM) is instrumented with 24 Hamamatsu R12199-02 HA PMTs of 3″ (7.62 cm) close to isotropically oriented as seen in Fig 4.6. Even though the size of each PMT is substantially smaller than for the standard DOMs, the large amount of PMTs make up for this, and increase the sensitivity by several factors.

As with the D-Egg, the extra PMTs improve the angular acceptance for the module, and for the mDOM this means almost homogeneous coverage for all angles. The directional information gained from multiple PMTs can also improve reconstructions.

4.5 IceCube coordinate system

The coordinate system of IceCube is defined so that the y-axis is pointing Grid North (aligned with Prime Meridian and pointing towards Greenwich,

UK), the x-axis points Grid East, and the z-axis is pointing up, towards the sky. The origin of the coordinate system is set at the depth of 1948.07 m in the ice, close to the center of the detector. In this coordinate system, the IceCube strings are between -500 m to 500 m and the DeepCore strings are -500 m to -150 m. The dust layer resides at -150 m to 50 m.

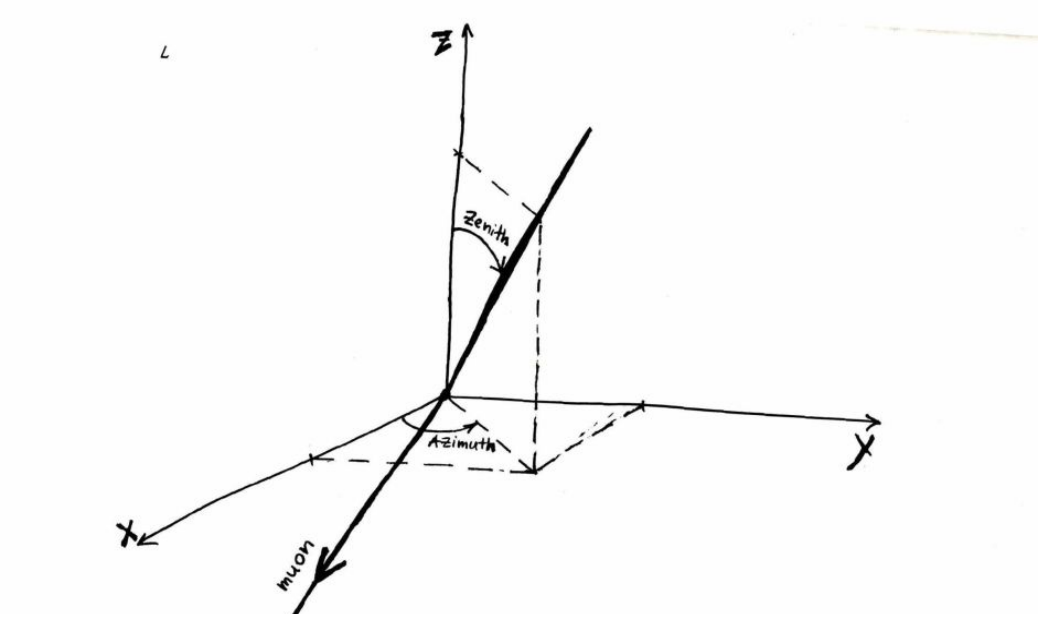

Figure 4.7: A diagram of the zenith and azimuth angles as used in the IceCube coordinates. A muon track is seen traveling through the coordinate system, to indicate how zenith and azimuth relates to muon direction. Drawn by Dusan Turcan.

Direction in IceCube, typically used when talking about the direction of a traveling particle, is usually defined by a zenith and azimuth angle. The zenith angle describes the angle between the z-axis and the (apparent) origin of the particle, while azimuth is the angle corresponding to the positive rotation around the z-axis, measured from the x-axis, to this same point. Zenith angle is also conventionally written as cos(zenith). In this convention, an upwards going particle would have cos(zenith) between 0 and -1, and a downwards going between 0, and 1. An example of zenith and azimuth on a traveling muon, is seen in Fig. 4.7.

4.6 Event Signatures

In general, IceCube event topologies consists of three types of events. There are the cascades and the track like events as seen in Fig. 4.8, and the rare

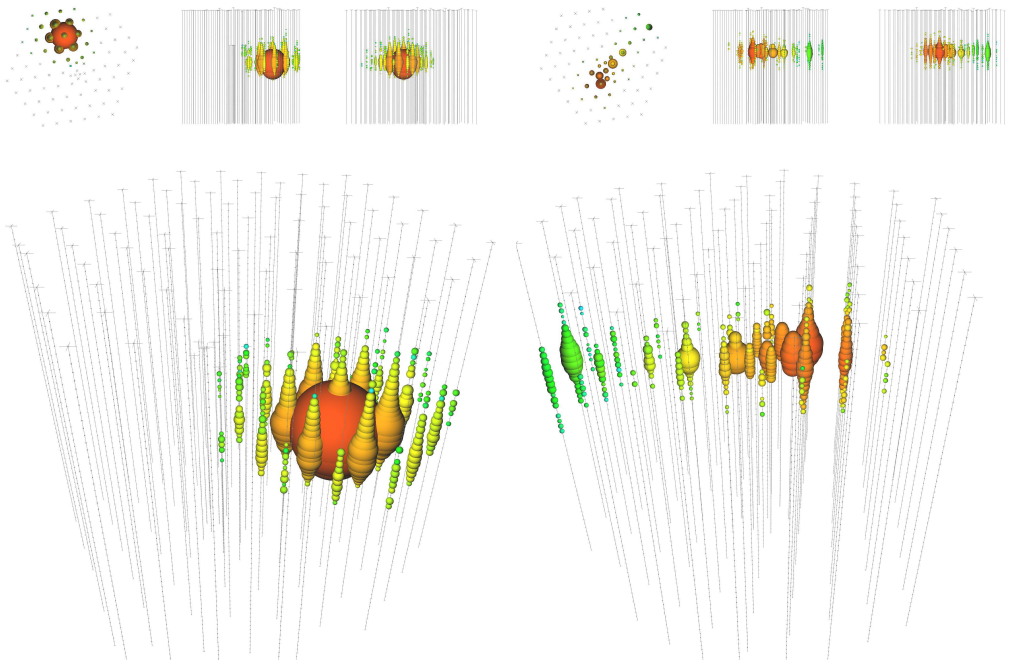

Figure 4.8: An example of the two types types of the event topologies in IceCube. Each sphere is a representation of a DOM in IceCube while the size of the sphere is proportional to the amount of observed light in a given DOM. The color is the relative time difference of each recorded photon on the DOMs. From [35]. **Left:** This specific cascade event deposited 1.05 PeV energy in the detector as light. **Right:** A track like event generated by a muon which deposited 74 TeV in the detector before escaping outside the range of the IceCube strings.

double-bang event [34]. Track like events, comes from the muon's cherenkov emissions as they travel through the ice. These, most predominately, come from the abundance of muons generated in the cosmic air showers, or from a CC ν_μ interaction in the ice. Cascades comes from particle showers in the detector, either from a CC ν_e interaction generating a electromagnetic and hadronic shower, or from any NC interaction generating a hadronic shower.

Events from CC ν_τ events can be track-like from the decay of the τ into a muon, or it can be cascade like from the decay into electrons and from the hadronic cascade. It is possible for a CC ν_τ interaction to produce a double-bang, which is two cascades resulting from the creation and decay of the τ lepton connected by a track from the traveling τ lepton.

5 Simulation

The focus of this thesis was to help in the development of DirectReco, a new reconstruction algorithm to be used in the ICU. To be able to develop and test the algorithm, Monte Carlo (MC) simulation was used. For the work of this thesis, only the D-Eggs were used, since they were the simpler optical module in the ICU, further explanation is given in Section 7.1. As such, when explaining optical module specific information, my focus will be on D-Eggs.

In IceCube there exist a lot of software that allow for most kinds of analysis that one would be interested in. In general, the simulation chain is `Initial particle generation -> Particle propagation -> Photon propagation -> Background / Noise generation -> Detector simulation.`

For all these steps, there are multiple different modules which are specific for ones area of interest, or specific needs. For example for the first step of generation of particles, there are modules for simulating a cosmic showers [36], simulating only muons, or only neutrinos [37].

In general, the simulation software that I have used was divided into 4 steps, and so I have also divided this chapter into 4 parts, each consisting of an explanation of the specific step in the simulation. A simplified chain of steps done in simulation is shown in Fig. 5.1. From each step, a list containing the relevant data will be passed on to the next step in simulation. In this thesis I will use the term *event* to describe a single particle simulation in the detector.

5.1 Step 1 : Generation

There exists a lot of software which has been modified to work specifically for IceCube, but for this thesis none of the generation software were used. Similar for all the generation modules is that they output an `I3MCTree`. This is essentially an object containing all the information about the particles in the simulation, and their relation to each other. At the top of the tree there is the primary particle and secondaries branch out from the primary. Information about the particles include their position, velocity, direction, type and any other relevant information. This tree is then subsequently passed on to the propagators which take care of the rest of the propagation.

For the testing of DirectReco, it was important to start with a simple setup. By starting with a simple setup, any problems that might occur, would be easier to understand, than had a more complex setup been used. As such, the particle to be reconstructed, was chosen to be an electron. Electrons produce cascades from the electromagnetic shower, which will deposit much

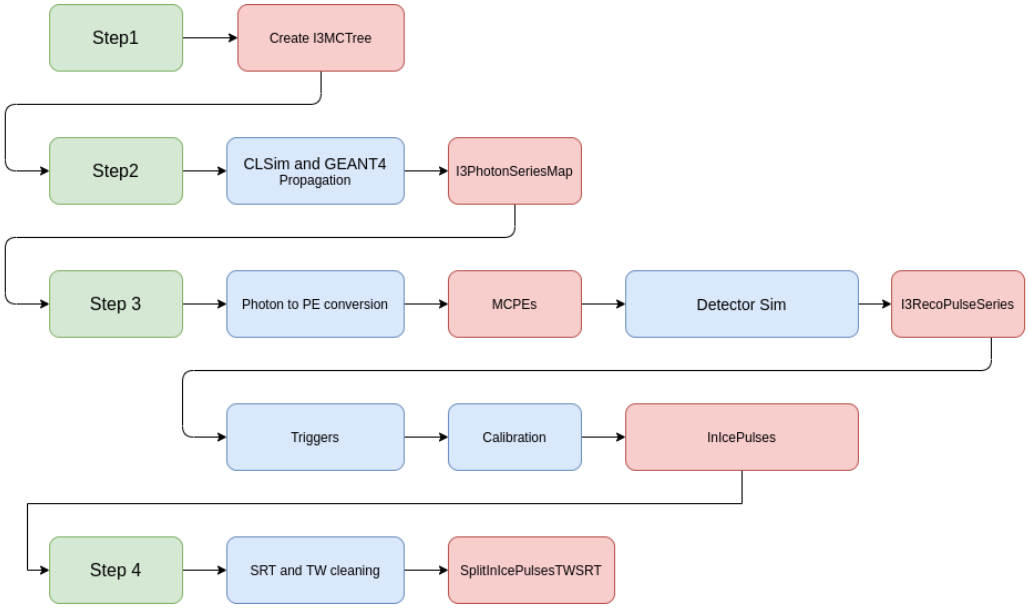

Figure 5.1: A diagram of the simulation chain used in this thesis. Green colour ▭ describes any start of a step, blue ▭ describes some module which is being used, and red ▭ means the creation of that specific object. A more comprehensive diagram can be seen in the appendix in Fig. F.1.

of the initial electron's energy in the form of Cherenkov light, which should make reconstruction easier. Since electrons were used there was no need for neutrino or muon simulation but it was merely enough writing the I3MCTree directly and passing it on to the propagator.

5.2 Step 2 : Propagation

In step 2, particle and photon propagation is simulated. This is done using GEANT4 and CLSim.

For the propagation of the particles GEANT4 is used [38]. Specifically for the work on this thesis, that was the propagation of the electron through the ice of the detector and any interactions caused by it.

For the photon propagation, the software developed by the IceCube collaboration, CLSim was used [39]. CLSim is a module which uses ray-traycing of the photons using the OpenCL framework to simulate the photons directly through the ice of IceCube. Since photons in CLSim can be independently simulated, each photon is given to a graphical processing unit (GPU) thread to propagate. When a photon has finished propagating, by either being absorbed in the ice or by hitting a DOM, the thread grabs a new photon to propagate from the photon pool of non-propagated photons. All photons

which hit DOMs are saved into a `I3PhotonSeriesMap`, containing the information about the time of hit, direction, position and wavelength as well as the specific DOM which was hit.

As a computational speed-up, photon weighting can be used for CLSim, which gives each photon a weight, based on its wavelength and the wavelength acceptance of the DOM. Photons are then only propagated according to their weight, such that photons with wavelengths that would never be accepted in a DOM, are simply not propagated, saving computational time. This procedure unfortunately became more complicated when simulation of the ICU were produced. In the ICU there are multiple modules with different wavelength acceptance curves, so instead of a simple curve being used, a combined envelope is used to give weight to the photons.

5.3 Step 3 : DOM and Detector Simulation

In Step 3 the photons from the `I3PhotonSeriesMap` are converting into photoelectrons (PE), and afterwards the detector simulation is run which includes noise, SPE charge, and other relevant effects.

5.3.1 Photon to PE conversion

In this step, each photon will be given a probability to be converted into a PE. These probabilities are based on the hit DOM's angular acceptance, wavelength acceptance and the photon weight. The wavelength acceptances implemented in the simulation currently are seen in the left figure of Fig. 5.2 with the angular acceptances on the right. The probability of a PE conversion is then calculated by getting the wavelength acceptance for the given wavelength of the photon and multiplying it with the angular acceptance for the given angle multiplied with the photon weight.

$$P(\gamma \rightarrow \text{PE}) = P_\lambda(\lambda(\gamma)) \cdot P_\theta(\theta(\gamma)) \cdot w(\gamma), \tag{5.1}$$

where $P(\gamma \rightarrow \text{PE})$ is the conversion probability, $P_\lambda(\lambda(\gamma))$ the wavelength acceptance, $P_\theta(\theta(\gamma))$ the angular acceptance, $w(\gamma)$ the weight of the photon, and γ is a specific photon.

This angle is defined as the angle between the normal of the PMT and the photon direction, and is used to find the angular acceptance at that given angle. The PMTs are pointing directly downwards and the angular acceptance is modelled to be rotationally symmetric around its normal, so this angle will be independent on the azimuth angle. When the probability of conversion has been found, it is used to decide whether the the photon discarded or saved as a PE.

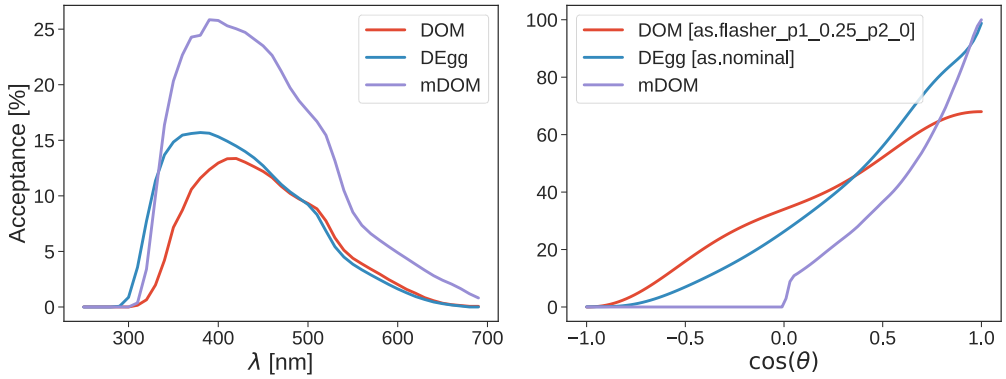

Figure 5.2: The acceptance of the three optical modules of the ICU, regular DOMs, DEggs and mDOMs. **Left:** The wavelength acceptance for each module. The mDOM acceptance is much larger, probably because it has not been module scaled. More on module scaling in Section 7.2. The DEggs also show more sensitivity in the UV as expected. **Right:** The angular dependence on acceptance. The different ice model parameterizations are seen in the legend besides the specific module that uses it. The mDOMs do not use hole ice parameterization.

Getting the wavelength acceptance for the D-Egg and mDOM is equivalent to the regular DOMs but getting the angular acceptance is less trivial. For the mDOMs, each PMT is simulated as a flat disk and intersections with these defines which PMT is hit.

The D-Egg implementation separately calculates a probability for each PMT, given the angle between the incoming photon and the PMT normal. Similarly to the regular DOMs, this angle will be independent on the azimuth since the PMTs are pointing either directly upwards or directly downwards. The angle of one PMT will be equal to the difference between π and the angle of the other PMT. For example, if the angle between the downwards looking PMT and the incoming photon is $\pi/4$ then the upwards looking PMT will have an angle to the incoming photon of $3/4\pi$. The angular acceptance of each PMT can then be extracted, using these angles, from the angular acceptance curve of the D-Egg PMTs, seen in Fig. 5.2. The total probability of conversion, $P(\gamma \rightarrow \text{PE})$, from Eq. 5.1, is calculated for each. The fate of the photon is then determined by drawing a random number between 0 and 1. If the number is larger than the combined probability of conversion for both PMTs the photon is discarded. If not, then if the number is smaller than the probability of conversion for the downwards looking PMT, the photon hits this PMT, if not then the photon hits the upwards looking PMT. When a photon has been accepted by the PMT in simulation, the photon becomes a PE.

The angular acceptances of all PMTs in simulation also depend on the specific hole-ice parameterization that is used. The hole-ice parameterization depend on which module that is used, since the ICU probably be different than that of the regular DOMs, though the exact difference is not known yet[4]. The angular acceptance of the DEggs that is used in simulation is, as of now, just the regular DOM angular acceptance but with a different hole-ice parameterization. All of the angular acceptances can be seen in Fig. 5.2, using their specific hole-ice parameterization.

The converted photons are then sent to the `Detector Sim` as `MCPEs`. These MCPEs are what has been used for most of the work on this thesis, because they contain no detector simulation nor any added noise, which was beneficial for the testing of DirectReco. For some of the next steps, I will not go into much detail, since they were not used for a large part of the thesis. At this point, the MCPEs are accepted by the PMT, and can be referred to as a *hit* in the PMT. Normally, they would not be referred to as *pulses* since they have no charge at this point, but in this thesis I will break convention and refer to them as pulses in the analysis in Section 7 and Section 8. To distinguish between these hits and the pulses from later simulation steps, it will be explicitly stated whether the analysis was with or without detector and noise simulation.

5.3.2 Detector Sim

The first step of the detector simulation is to add noise. This is done using the Vuvuzela model [27]. It simulates the noise components as three independent processes, to capture the dark noise components explained in Section 4.1.5. The noise is added as PEs into the list of PEs from actual photons.

The next step is the PMT simulator. It simulates the PMT and outputs the charge at the anode for each PE, converting it into a pulse. All PEs share the same probability of being a pre-pulse or a late pulse, where the probability of being a normal pulse is then $P(\text{normal}) = 1 - P(\text{late pulse}) - P(\text{pre-pulse})$. Each PE is determined to be either of the three types from a random number draw. A normal pulse, will get a charge assigned to it drawn from the SPE template, and the time will have a small time jitter added to it. A pre-pulse will always have a charge of 1/20 and the time will have jitter added as well as a pre-pulse shift. For a late pulse the charge will be drawn from the SPE distribution, and the time will have some late-pulse time delay added to it.

[4]The hole-ice used in simulation for regular DOMs is `as.flasher_p1_0.25_p2_0`, while D-Eggs use `as.nominal`. The mDOMs do not use hole-ice at all.

For any non pre-pulse, there is a probability of initiating an afterpulse. The afterpulse time will be some delay after the pulse that it was initiated by and the charge will be drawn from the SPE template. Saturation is applied to the pulses at this step, and the pulses are merged if they are close than 200 picoseconds of each other.

For the DEggs the probabilities of having an after-pulse, late pulse, or pre-pulse is set to zero and no saturation is applied.

For normal DOMs the pulses will then be passed on to DOMLauncher which takes care of the simulation of the mainboard of the DOM which entails launches and digitization. The main features of the DOMLauncher is the discriminator, LC logic and digitization. For the ICU, DOMLauncher is not used, because the electronics are yet to be finalized for the ICU optical modules. Instead a simplified module is used which applies a simplified discriminator and merges pulses that are close than 200 nanoseconds of each other. If any pulse is within these 10 ns they will be merged into a single pulse with the charge being the sum of charges and the time being the latest of the two times. After the merging of pulses any pulses with a charge less than the discriminator of 0.25 will be discarded.

From the detector simulation the pulses are stored in `I3RecoPulseSeries`, which are then sent through the `Triggers` module.

5.3.3 Triggers

Triggering is used on real data to distinguish a neutrino event from noise. Triggering is also run on simulation to emulate what is done on real data. These include Simple Multiplicity Trigger (SMT), string trigger (cluster trigger), volume trigger (cylinder trigger) and Slow Particle trigger (SLOP). For the cascade simulation that the electron produces the SMT trigger is most relevant. It simply checks whether there has been N number of hits in a given time windows of all DOMs.

5.3.4 Calibration

In the calibration step, a module calibrates the launches from DOMLauncher into waveforms using calibration constants. Afterwards these waveforms are run through the wavedeform module which tries to deconvolve these into photons again using linear algebra. These pulses are sent to step4 as `InIcePulses`.

Since DOMLauncher does not exist for the ICU simulation, this step is not used for the ICU simulation.

5.4 Step 4 : Preprocessing

In this step cleaning of the pulses is done using two algorithms, the Seeded Radius-Timing (SRT) and Time Window (TW) cleaning. The SRT cleaning step iterates through the HLC pulses and for any SLC pulse that is within 150 m of the given DOM with the HLC pulse it is added to a cleaned pulse list. This process repeats with the cleaned pulse list until no new pulses can be added. The TW cleaning simply removes any pulses outside the a given time range of the trigger time.

Finally the pulses from this are stored as `SplitInIcePulsesTWSRT`, which are the pulses used by DirectReco when noise and detector simulation was not removed.

6 Reconstruction

The reconstruction of particles is an extremely important aspect of particle physics experiments. Reconstruction is the aspect of taking whatever electronic signal your detector outputs and try to figure out, or *reconstruct*, whatever source caused the signal. Specifically, for the IceCube detector, that would usually be reconstructions of neutrinos. Parameters of interest for IceCube are the energy (**E**), time (**t**), zenith angle ($\boldsymbol{\theta}$), azimuth angle ($\boldsymbol{\phi}$), and position (**x, y, z**). If one wishes to reconstruct track-like events another parameter to reconstruct would be the track length (**L**). In this work, only electrons are simulated, which produce cascades, and so, no track length is reconstructed.

When an event has been observed, a reconstruction algorithm is given the pulses of observed light in the PMTs for this event. For DirectReco and table based reconstruction (Section 6.1 and 6.3), they will work by subsequently testing a hypothesis particle with different sets of parameters and compare the light yield of the hypothesis to the observed light. The comparison is done by constructing a likelihood function, and the algorithm tries in this way to maximise the likelihood and find the most probable particle for the observed light yield. The exact way in which the algorithm tries to explore the likelihood space, is different for different algorithms, as well as the method for getting the light yield for a given particle hypothesis. The ideal case of a reconstruction algorithm is one that can get accurate results quickly. One such algorithm does not exist, so algorithms might be more focused on the accuracy rather than the speed, which is the case for DirectReco.

Table-based reconstruction is one of the main reconstruction methods and is described in the next subsection. The framework that DirectReco uses for minimization and likelihood reconstruction is explained Section 6.2, and DirectReco is explained in Section 6.3.

6.1 Table-based reconstruction

In IceCube light will scatter and be absorbed in the ice and with ice properties differing at all depths this makes evaluating light yield in a PMT non trivial. Some reconstruction methods therefore use splined table look ups [40] for their photon yields when evaluating a set of parameters for a hypothesis. These tables are generated by simulating the photons for a cascade or muon track in as many configurations of the parameter space as possible. Each photon is then propagated through the medium and at each propagation step the photon yield of its 3D voxel is evaluated and stored. This is repeated multiple times to get a cumulative density function (CDF) of the

possible light yields at a given position in space and time and a given set of parameters for the light source. The time and photon intensity is stored in a 6 dimensional binary *table*. The tables are splined, so that it is possible to obtain the light yield from any particle parameters and not just the simulated discrete ones. The reconstruction method which was used for the previous low-energy IceCube analysis [41, 42, 43] was the PegLeg algorithm [44], which uses splined table lookups, for generating the light yield of the hypothesis.

When the tables have been generated, finding the light yield of a given hypothesis, only takes as long as looking up an entry in a table, but the downside of table-based reconstruction comes from the generation time. Generating the full tables with splining can take multiple months of human checking and tuning. This in itself would be no problem if it only had to be generated once, but as the calibration of the ice gets better and with the ICU soon being deployed, tables will have to generated again. This generation also has to be repeated for every systematic uncertainty variation in the ice. In part because of the generation time as well as difficulties in systematic uncertainty tests, many new reconstruction algorithms are being developed. One of which is DirectReco.

6.2 Millipede

Millipede is a framework for reconstructing particles, and provides the ability to construct the likelihoods and perform the minimization. Millipede has to be provided with a module for construction of light yields, which could be the splined photonic tables, described in the previous section. Millipede constructs a time binning for the supplied observed light and the hypothesis, such that they can be used for constructing a likelihood. This is by default a dynamic binning that puts a specific number of photons into each bin.

6.2.1 Likelihood

The likelihood calculation in Millipede uses the number of observed pulses k_j in a given bin j, and the number of pulses from the hypothesis Λ_j. The detected number of photons are expected to follow a **Poisson** distribution with a mean of Λ. The likelihood of observing Λ_j given the observed k_j pulses in a bin, $\mathcal{L}_j$, is given by

$$\mathcal{L}_j = \frac{\Lambda_j^k}{k!} e^{-\Lambda_j}. \tag{6.1}$$

The total likelihood is the multiplication of the likelihoods of all bins in all PMTs

$$\mathcal{L} = \prod_{j=1}^{M} \mathcal{L}_j, \tag{6.2}$$

$$= \prod_{j=1}^{M} \frac{\Lambda_j^k}{k!} e^{-\Lambda_j}, \tag{6.3}$$

where M is the total number of bins. As is custom with likelihood calculations, it is beneficial to take the natural log of the likelihood, to reduce numerical errors. Logarithms perserve any maxima or minima in the original likelihood, so using them for the application of finding a maximum or minimum is valid. Taking the natural log results in

$$\ln(\mathcal{L}) = \sum_{j=1}^{M} \left(k \ln(\Lambda_j) - \ln(k_j!) - \Lambda_j\right). \tag{6.4}$$

The factorial can then be approximated as the Gamma function Γ, and to be explicit that Λ depends on the parameters of the hypothesis particle ($\boldsymbol{X}$) we let $\Lambda_j \to \Lambda_j(\boldsymbol{X})$, to finally optain the default likelihood used in Millipede

$$\ln(\mathcal{L}) = \sum_{j=1}^{M} \left(k \ln(\Lambda_j(\boldsymbol{X})) - \ln(\Gamma(k_j)) - \Lambda_j(\boldsymbol{X})\right). \tag{6.5}$$

Because of the non-analytical $\Lambda_j(\boldsymbol{X})$, Eq. 6.5 has to be solved with numerical minimization.

6.2.2 MINUIT minimization

For minimization, Millipede uses the minimization framework of MINUIT [45]. MINUIT needs to be supplied with a `FCN` method for computing the likelihood, which in the case of millipede will by default be the Poisson in Eq. 6.5. MINUIT will try and minimize the likelihood, so the negative log-likelihood is used.

MINUIT can use one of three minimization subroutines, SEEK, MIGRAD, and SIMPLEX. SEEK is a simple Monte Carlo sampling method which does not try to converge, but can give a good starting point for the other two. MIGRAD is a minimization routine that uses gradients to find the minimum and converge.

The SIMPLEX routine tries to find the minimum by constructing a simplex in the parameter space, and using reflections to find the minimum, based

on the Nelder-Mead method [46]. Notably, it is a minimization technique which uses no derivative, as opposed to the MIGRAD subroutine.

A simplex is the simplest possible polytope in a given space, where a polytope is a geometric object with flat side. For 2 dimensions a polytope is also known as a polygon. The simplest type of a polytope (simplex) in 1D is a line segment, and in 2D it is a triangle as opposed to a square, since the triangle has less vertices. In 3D the simplex is a tetrahedron, and this can be generalized to any number of dimensions. A simplex will always have $n+1$ vertices, where n is the number of dimensions.

For the minimization, the simplex is constructed by a starting point, supplied by the user, as the first point, and the rest of the points are generated by finding a local minima along each coordinate axis from the starting point. For each local minima a new point for the simplex is generated. Using this method $n+1$ points will be generated, which make up the simplex.

An iteration of the SIMPLEX routine, consists of first finding the worst point of the $n+1$ points (the point with the largest FCN value, in case of minimization). A new point that needs to be evaluated, $\boldsymbol{x}_r$, is found by reflecting the worst point, $\boldsymbol{x}_w$, over the center of all the rest n points, $\boldsymbol{x}_c$

$$\boldsymbol{x}_r = \boldsymbol{x}_c + \alpha(\boldsymbol{x}_c - \boldsymbol{x}_w), \tag{6.6}$$

where α is some reflection coefficient large than 0. From here, there are a number of different possibilities

1. If this new point is better than the second to worst point, $\boldsymbol{x}_{sw}$, but still worse than the best, $\boldsymbol{x}_b$

   $$FCN(\boldsymbol{x}_{sw}) > FCN(\boldsymbol{x}_r) > FCN(\boldsymbol{x}_b),$$

   the worst point is replaced by the reflected new point.

2. If, however, the reflected point is better than the best point,

   $$FCN(\boldsymbol{x}_b) > FCN(\boldsymbol{x}_r),$$

   then another point is evaluated which resides further in away in the direction of the reflected point

   $$\boldsymbol{x}_e = \boldsymbol{x}_c + \gamma(\boldsymbol{x}_r - \boldsymbol{x}_c), \tag{6.7}$$

   where γ is some expansion coefficient larger than 1. From here, there are two extra options:

(a) If this expansion point is better than the reflected point,

$$FCN(\boldsymbol{x}_r) > FCN(\boldsymbol{x}_e),$$

replace the worst point with the expansion point.

(b) if not, replace the worst with the reflected point.

3. If the reflected point is worse or equal to the second to worst point, x_{sw},

$$FCN(\boldsymbol{x}_r) \geq FCN(\boldsymbol{x}_{sw}),$$

then compute a new contracted point

$$\boldsymbol{x}_c = \boldsymbol{x}_c + \rho(\boldsymbol{x}_w - \boldsymbol{x}_c), \tag{6.8}$$

where ρ is the contraction coefficient, between 0 and 0.5. If the contraction point is better than the worst point, replace it by this contraction point.

4. The simplex is reduced in all directions by a factor of 0.5 keeping only the best point $\boldsymbol{x}_b$.

5. It can also choose to use the best point as a starting value and evaluate a new simplex.

This process is then iterated until convergence is found. Convergence is considered when

$$EDM = FCN(\boldsymbol{x}_w) - FCN(\boldsymbol{x}_b) < 0.1, \tag{6.9}$$

which at this point the routine stops and the estimated-distance-to-minimum (EDM) value is output as well as the FCN value of the best point and the corresponding parameters.

6.3 DirectReco

DirectReco is a Millipede based reconstruction algorithm, but replaces the usual photon tables with a direct simulation of the photons from the particle hypothesis using CLSim. Every hypothesis is simulated multiple times, to smooth out the stochasticity in the photon propagation. The amount of times a given event is re-simulated is called the **oversampling**. Fig. 6.1 shows an illustration of a hypothesis being evaluated in DirectReco. A large oversampling will make the likelihood landscape smoother and help the minimizer reconstruct to better values, but for every oversampling, the reconstruction

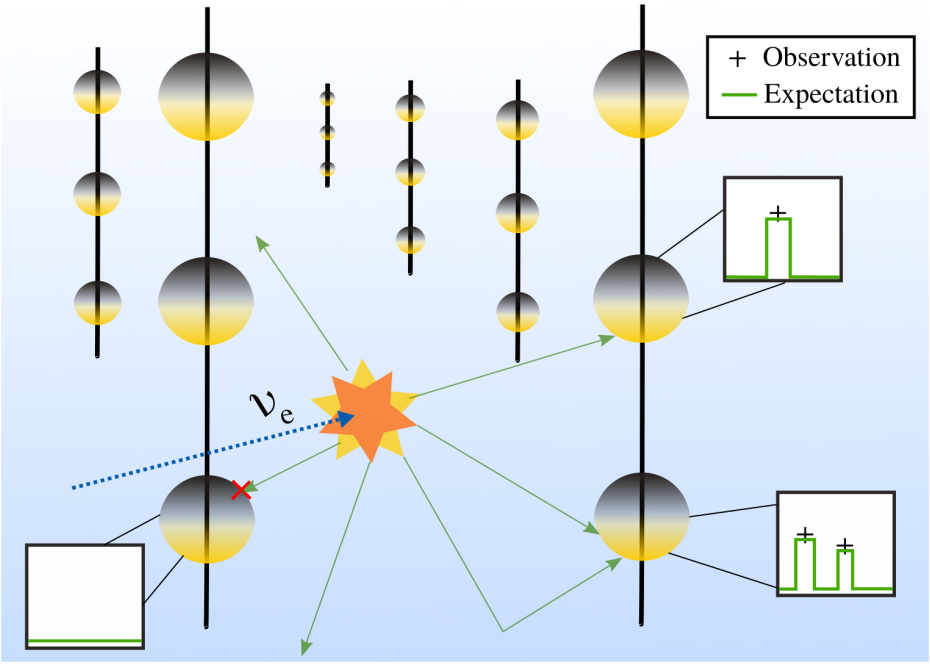

Figure 6.1: An illustration of the true hypothesis being evaluated in DirectReco. The green arrows indicate the photons, scattering and being absorbed and the boxes show the light yield from the observation and the expectation from the hypothesis. In this illustration, only regular DOMs are shown. In reality more light will usually be observed and more noise will be present, but the illustration is simplified for clarity. From [47].

time gets longer. This makes the reconstruction time substantially longer than for tables, but DirectReco offers lot of advantages in other areas.

Importantly, DirectReco is also modular, in that if calibration of the ice gets better and the parametrization of the ice is changed, unlike the tables which needs to be regenerated, DirectReco takes the new ice model as input and runs immediately.

For the likelihood model, DirectReco does not use the default Poisson likelihood, but a modified version of the likelihood model called the DIMA-LLH [48] is used instead. The DIMA-LLH uses weighted data and weighted simulation terms, but the modified version in DirectReco only uses the weighted term for simulation (oversampling)

$$\ln(\mathcal{L}_{DIMA}) = \sum_{j=1}^{M} n_{os}\Lambda_j \ln\left(\frac{\mu_j}{\Lambda_j}\right) + k_j \ln\left(\frac{\mu_j}{k_j}\right), \tag{6.10}$$

where, n_{os} is the oversampling, Λ_j is the expected light in a given bin j, k_j

is the observed light, and

$$\mu_j = \frac{n_{os}\Lambda_j + k_j}{n_{os} + 1}. \tag{6.11}$$

The performance difference of the Poisson and DIMA likelihoods are not completely understood, but initial testing has shown that the DIMA likelihood shows slightly better results.

For the minimization, DirectReco uses the SIMPLEX algorithm from MINUIT.

From a previous study done by Thomas Halberg [47] looking into DirectReco at low energies, it was found that using Millipede's default dynamic binning gave rise to problems, so DirectReco now uses uniform binning, with a bin width of 8 ns. Bin sizes less than 8 ns also showed to be problematic.

6.4 Seeding algorithms

For most minimization based reconstruction algorithms, they usually need an initial guess of the parameters called a **seed**. To be able to guess without being too far off, algorithms which can produce a rough but quick reconstruction is usually used. A few which was used for the analysis of DirectReco is presented here.

6.4.1 Center Of Gravity

Center of Gravity (CoG) is a very simple algorithm for getting an initial guess for x, y, z. It finds the average position of pulses

$$\vec{r}_{CoG} = \frac{\sum_i^N \vec{r}_i}{N}, \tag{6.12}$$

where N is the number of hits, and $\vec{r}_i$ is the position of a hit.

6.4.2 LineFit and SPE fit

LineFit is a reconstruction algorithm which ignores the ice properties and the geometry of the Cherenkov cone, and assumes the particle travels in a straight line emitting photons perpendicular to its travel direction. Given the OM locations, r_i and the pulse hit times t_i, a function with the two free parameters, the vertex point $\vec{r}$, and the direction $\vec{v}$, should be minimized

$$r_i = \vec{r} + \vec{v}t_i. \tag{6.13}$$

This equation can be solved analytically by

$$\vec{r} = \langle r_i \rangle - \vec{v} \langle t_i \rangle , \tag{6.14}$$

$$\vec{v} = \frac{\langle r_i t_i \rangle - \langle r_i \rangle \langle t_i \rangle}{\langle t_i^2 \rangle - \langle t_i \rangle^2}. \tag{6.15}$$

The direction is then simply $\vec{e} = \vec{v}/|\vec{v}|$.

The single-photon-electron (SPE) fit uses the LineFit result as input and uses likelihood maximization to try and improve the result of LineFit [49].

7 Smaller Projects

As part of my work at NBI and IceCube, a few other smaller projects were worked on besides the main project with DirectReco. I will go through two of them in this section. In Section 7.1, I will describe the different custom detectors I made in simulation that was used in the analysis of all smaller projects as well as the DirectReco analysis. In Section 7.2, I will describe the implementation of a realistic acceptance curve for the D-Eggs in simulation.

7.1 Custom Detector Setups

For most problems, starting as simple as possible and working your way to larger complexity can be beneficial in the long run. In the same way, being able to test simulation as well as reconstruction algorithms on a more simplified detector than the whole of IceCube, could also be beneficial. Using a smaller custom made detector in simulation made it possible to look at the charge vs. time distributions of their pulses (waveforms) in all PMTs, which would be impossible for the real detector having more than 1000 PMTs, making it impossible to visualize in a single PDF file. While this simplification was beneficial to some of the analysis, it also turned out to be a problem for some of the DirectReco analysis, as will be explained in further detail in Section 8.1.2. Another simplification was to only focus on the D-Eggs in the ICU, instead of using all ICU modules like the mDOMs. The mDOM has 24 PMTs which would drastically increase the number of PMTs in the simulation and the mDOM simulation is different to D-Eggs, so by focusing on a single module the process would be more streamlined. One could then, after making D-Eggs work, move on to the mDOMs. Since D-Egg reconstructing is still showing problems, I never moved on to mDOMs.

To produce any simulation, the scripts needs to be provided with a **G**eometry-**C**alibration-**D**etector (GCD) file, which contains all things relevant to the detector. That is the placement of each DOM in space as well as on which strings, and which PMTs belong to which DOMs. It contains specific parameters for the individual modules, in order to produce correct SPE distributions and noise in the each PMT. To be able to make a custom detector, this GCD file needs to be modified, with the specific geometry that is wanted. To create an only D-Egg simulation, a single D-Egg from a realistic ICU GCD file was used to generate the whole custom detector[5].

[5]The GCD file that was used was `GeoCalibDetectorStatus_ICUpgrade.v55.mixed_noGap.V4`, and the specific D-Egg was OM 24 on string 89.

The `circle_9` geometry, was the first iteration of the custom detector that was used for a long time in the DirectReco analysis, as well as for the D-Egg acceptance implementation, which will be explained in the next section. It uses the same ice as the IceCube detector but the string placement and number of optical modules, are different. It consists of 5 strings in a circle with a radius of 20 m. The number 9 from the naming, comes from the fact that each string had 9 modules on them, with the 5th module placed at z=0, with 4 above and 4 below. The module spacing was 3 m, so to emulate the spacing of the to-be ICU module spacing. All in all, that makes up 5 (strings) $\cdot$ 9 (OMs on string) $\cdot$ 2 (PMTs on OM) = 90 PMTs, making it possible to visualize the waveforms of all. Using the IceCube coordinates of the ice, the detector had its center at (x,y,z)=(0,0,0), which puts it at a depth of 1948.07 m in the ice. In all parts of the analysis, this GCD file was used when simulating an directly upwards going (zenith=π) electron placed at the center of the detector. The electron is chosen because it produces a simple cascade and it should deposit most of its energy in the medium in the form of Cherenkov radiation. Putting it in the center of a circle of strings made it possible to study the waveforms from each PMT to see if any discrepancies were found. One would expect, on average, an equal light deposit in each PMT in a circle layer, which could be directly checked whether that was the case. Any discrepancy between upwards facing and downwards facing PMTs could also be studied. This setup can be seen in the top-left of Fig. 7.1, with an example of an electron event on the top-right.

The next iteration, which was only shortly used, was the `circle_40` detector. It was introduced after it was discovered that the `circle_9` detector was too small to include the maximum amount of light emitted by the electron. This is described in further detail in Section 8.1.2. The only thing that changed in this iteration as compared to the previous one, was the addition of 31 more modules on each string, keeping the vertical spacing of 3 m, making it a taller detector. For a single string, there were now 20 modules above and 20 modules below z=0. This was a total of $5 \cdot 40 \cdot 2 = 400$ PMTs, making it vastly more difficult to visualize all PMT outputs, but still possible. This setup can be seen in the middle row of Fig. 7.1.

The final custom detector that was used was the initial ICU GCD file, but with all modules replaced with D-Eggs[6], the `Upgrade_DEgg` detector.

[6]Any DOMs in the IceTop array were removed. They were problematic and would not contribute to any readout since all electrons would be situated in DeepCore and the ICU anyway.

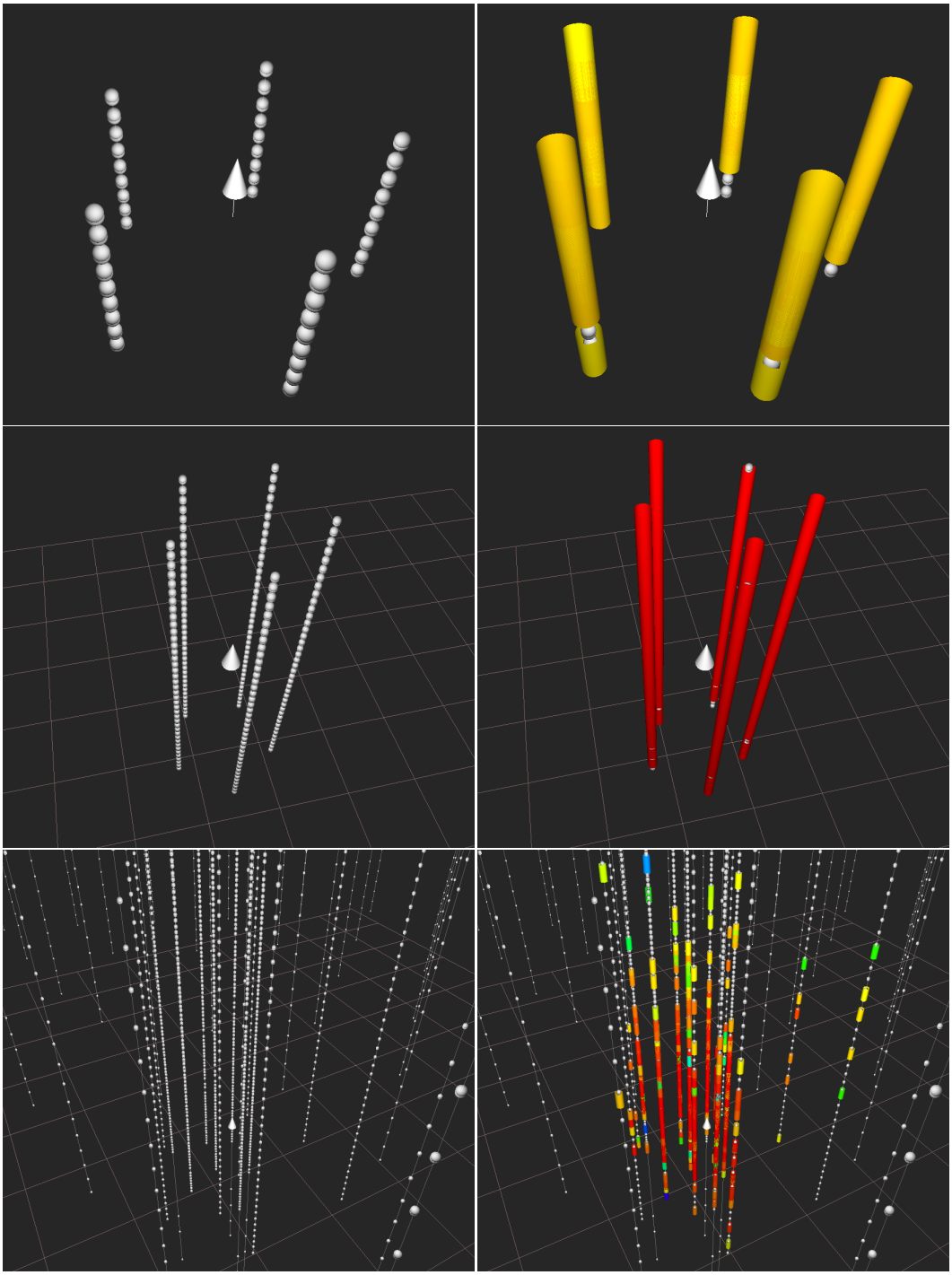

Figure 7.1: The three different types of custom detectors used in this thesis, each shown with a directly upwards going 50 GeV electron event on the right. The spheres are each PMTs, so two PMTs bunched together is a D-Egg. The arrow shows the direction and initial position of the electron, and direction of travel of the electron. When a PMT records a photon, it is shown as a colored cylinder in front of the PMT. When multiple PMTs on a string record photons, the whole string looks like a single colored cylinder. The color shows the relative hit times on the PMTs, where red is early and blue is late. When only a single color is shown, then the time difference is almost indistinguishable. **Top:** The `circle_9` detector setup. **Middle:** The `circle_40` setup. **Bottom:** The `Upgrade_DEgg` setup is shown.

The regular DOMs were also showing problems in DirectReco, so I choose to replace these, while another master student at NBI, Kasper Pedersen, was working on making the regular DOMs work for DirectReco. By replacing regular DOMs with D-Eggs, more information is gained from the two PMTs, while replacing the mDOMs with D-Eggs will give us less information. For the whole analysis, simulated electrons were only generated in DeepCore and the ICU, so replacing everything with D-Eggs is not a completely insane approximation to the actual ICU. Though, I will not claim that any conclusions on the resolution of the ICU can be drawn from the simulations done in this thesis, since this is not the actual ICU setup, but rather the focus should be on the comparison of the simulation to DirectReco, which both used this GCD file in the final steps of this thesis.

This detector geometry has 86 regular strings each with 60 modules which now have 2 PMTs each $86 \cdot 60 \cdot 2 = 10320$, including the 7 ICU strings, with a varying amount of modules on each, between 95 to 103. In total, this GCD file contains 11706 PMTs. While the upside of this GCD file is that it more closely represents the real ICU, the huge amount of PMTs makes it completely impossible to plot the waveforms of all PMTs.

7.2 Implementation of the D-Egg acceptance curve in simulation

When I started my project, the D-Egg wavelength acceptance was simulated using the regular DOM acceptance. Since that was not realistic, one of the small projects was to implement a more realistic acceptance curve. In the thesis by Ayumi Kiriki, [50] measurements from Hammatsu of the acceptance of all 643 planned D-Egg PMTs for IceCube were presented. The average of all the PMTs was extracted to be used for the implementation of the D-Egg acceptance curve in the simulation. Furthermore, his thesis also included the transmittance of the gel and glass, which was likewise extracted.

The acceptance and the transmittances were combined by multiplication to get the combined acceptance, and it was inserted into the D-Egg simulation part of the simulation chain.

One thing that was out of place in the new implementation, was that it seemed to be too good compared to the regular DOMs. The reason for this was found to be that the acceptance curves of the D-Egg that was pulled from the thesis of Ayumi Kiriki, was directly measured on the PMT, but what is needed in simulation is the acceptance on the whole module. Some photons hitting the module might not enter the PMT since the module radius is larger than the PMT radius, therefore the acceptance needed to be appropriately

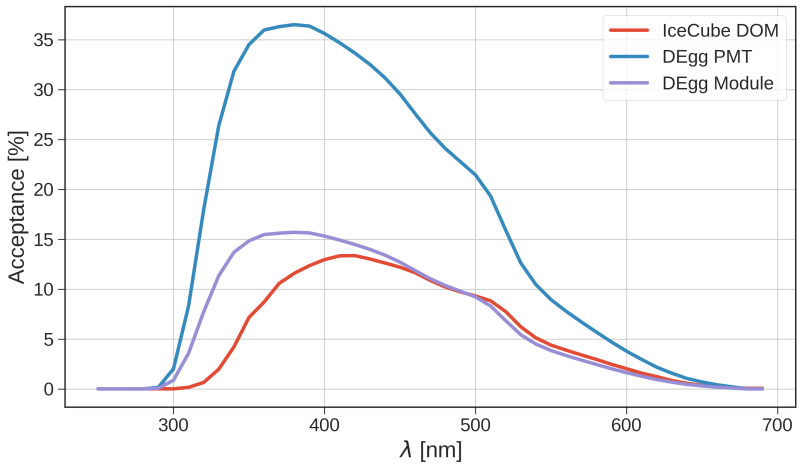

Figure 7.2: The regular IceCube DOM acceptance compared to the acceptance of the D-Egg PMT and the D-Egg acceptance scaled to the module size, by Eq. 7.1.

scaled. The scaled acceptance was calculated as such

$$P_{\lambda,\mathrm{Module}}(\lambda) = P_{\lambda,\mathrm{PMT}}(\lambda)\frac{r^2_{\mathrm{PMT}}}{r^2_{\mathrm{Module}}}, \tag{7.1}$$

where $P_\lambda(\lambda)$ is the wavelength acceptance and r is the radius. From Ayumi Kiriki's thesis, there were also a schematic of the module and the PMT in Fig. 4.1, from which I pulled the radii of both to do the calculation. Specifically, $r_{PMT} = 99.0126\,\mathrm{mm}$ and $r_{Module} = 151\,\mathrm{mm}$. The PMT acceptance and the module acceptance can be seen in Fig. 7.2, showing more realistic acceptance curve after the scaling.

To make sure nothing was wrongly implemented, extra checks were conducted. These checks were done in the `circle_9` setup described in section 7.1, with a directly upwards going electron in the middle of the circle. Specifically, the charge and time distributions of the pulses in all PMTs were compared, at different steps in the simulation chain. Such distributions of the `I3RecoPulses`, which are created by `DetectorSim`, can be seen in the top row of Fig. 7.3 of a single PMT. One would expect an increase in the amount of pulses observed since the acceptance is larger for the new implementation, so the plots have normalized counts such that the shape can be more closely compared. It was clear that the two charge distribution did not match, which was initially unexpected. In general, the time distributions also showed a difference at small times. The reason for this discrepancy was believed to be caused by the pulse merging in the `DetectorSim` module in the simulation. Since more light pulses were expected in the new implemen-

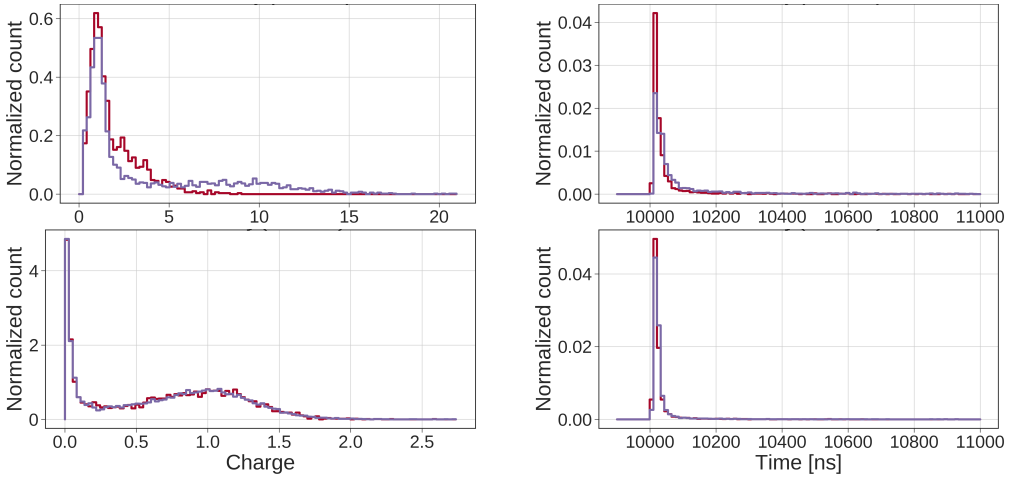

Figure 7.3: The normalized charge and time distributions of pulses from different parts along the simulation chain. A combination of the pulses from 900 events taken from a single downwards looking PMT in the `circle_9` setup described in section 7.1. The red is for the old implementation where the D-Egg used the regular DOM acceptance and the purple is my new implementation. **Top:** The pulses `I3RecoPulses` created by `DetectorSim` in step3 of the simulation. **Bottom:** The pulses `MCPulses` which are created in one of the modules in `DetectorSim` before the pulse merging.

tation, the pulses would also be closer in time to each other, and as such, more pulse merging would happen with the new implementation. To further investigate whether pulse merging was the culprit, the `MCPulses` were plotted. These pulses are created in the `PMTSimulator` which exists inside `DetectorSim`, and produces the `MCPulses` just before pulse merging happens in `DetectorSim`. If the pulses at this step, before merging, agreed with the previous implementation, then the discrepancy at the later step could be attributed to the pulse merging, which would show that nothing was wrong in the new implementation, and the discrepancy was simply attributed to the fact that the new implementation produces more pulses. The distributions of the `MCPulses` are seen in the bottom row of Fig. 7.4 of the same PMT as the row above, and shows a much better agreement, suggesting that the discrepancy is merely caused by the increase in pulses in the new implementation and not a fundamental problem in the implementation.

What can be seen as well is that some pulses in the top plot has much more charge than any of the pulses in the bottom plot. When pulses are merged, their charges are simply added together, which makes it possible to get much larger charge if more pulses are merged.

To investigate the pulse merging further, the Δt distributions are plotted and can be seen in Fig. 7.4, where the `MCPulses` are shown on the left and

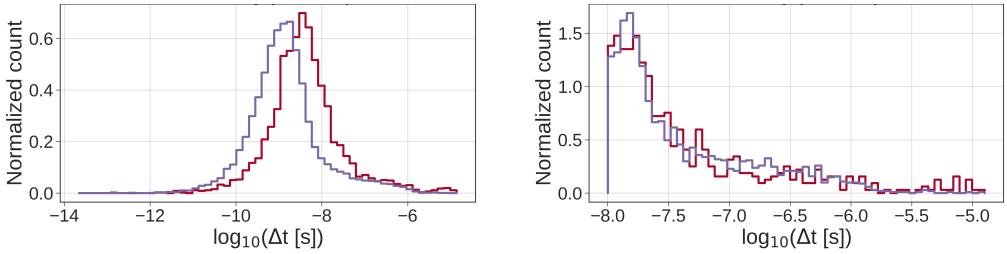

Figure 7.4: The log10 of the time between two consecutive hits Δt, taken for a single PMT in 900 events. The red is for the old implementation where the D-Egg used the regular DOM acceptance and the purple is my new implementation. **Left:** The `MCPulses` created in the `DetectorSim` module before the pulse merging. **Right:** The `I3RecoPulses` created as the final pulses of `DetectorSim`.

the `I3RecoPulses` on the right. Here, Δt describes the time between two consecutive hits on the same PMT. From the left plot, it can be seen that the new implementation has more consecutive hits closer spaced together than for the old implementation. This is expected since it accepts more photons than the old implementation did. On the right plot we can see that there are no pulses closer than 10 ns of each other, which is expected from pulse merging. From these investigations, it was accepted that the discrepancy in the `I3RecoPulses` was expected and caused by the pulse merging, so the new implementation did not show anything unexpected in its shape.

During the implementation of the new D-Egg curve, strange scaling factors were discovered which did not seem to be well understood. Since they were not well understood, I have included the exact way they are used in Step 2 and Step 3 in Section A in the appendix so that they can be further investigated.

8 DirectReco Analysis

The main part of the thesis was the investigation into DirectReco reconstruction at low energies for the ICU, specifically the D-Eggs. Only electrons were simulated and reconstructed to have a simple cascade event to reconstruct while working on improving DirectReco. Many things were investigated, many problems were encountered, mistakes were made, and therefore I have subdivided this section into three subsections. Section 8.1 will contain changes in the analysis setup from problems that were discovered during the investigations into DirectReco. Section 8.2, will contain changes to DirectReco and discoveries found directly related to DirectReco as part of the investigations. Finally, Section 8.3 will contain results from a high statistics run using DirectReco, to show its current performance, and its current problems.

8.1 Setup Changes

In science, it is usually a good idea to start with a simplified version of the subject in study, and then expand in complexity when the simplified version is well understood. In this subsection, a problem will be presented where there was not simplified enough, and another where the problem ended up being simplified too much.

8.1.1 Noise and detector simulation removal

During the investigations of DirectReco, there were many problems that were extremely hard to identify. They could be caused by a lot of issues, and finding the exact problem meant reading through thousands of lines of code to find the mistake. For one inexperienced to the IceCube software, this took a long time, and mostly nothing was found using this method. One specific problem, was that there seemed to be an offset in the generated light that DirectReco was finding compared to the light from simulation. One of the causes of this was found to be caused by the ice model, described in section 8.2.2, but another seemed to be caused by a lack of charge in DirectReco/Millipede.

In Millipede, there is a variable called `light_scale`, which caries the charge from the SPE distribution as well as other factors which should be applied to the pulses from DirectReco. It was found, by increasing this factor to something ludicrous, that it never seemed to be applied to any pulses. Not having charge applied will cause an offset since only simulation pulses will have the correct charge, while pulses from DirectReco will have

charge equal 1. It was not clear whether more problems were caused by a discrepency between the detector simulation of the simulated data and DirectReco, so it was decided to simplify the problem, by removing all noise and detector simulation from the simulated data, as well as from DirectReco. Any simulation starting from `DetectorSim` seen in Fig. 5.1 was removed, keeping the `MCPE`s and converting these into pulses by giving them an artificial charge of 1. The pulses generated from simulation and DirectReco, given the right hypothesis, should then be exactly equal, if the light hypothesis generation of DirectReco was working as it should. This was initially not the case, as will be described in Section 8.2.

Noise and detector simulation was never added back in since there are still problems with DirectReco in this simplified form, so `light_scale` was never investigated in detail. Once detector simulation is added back in, `light_scale` should be further investigated.

8.1.2 Detector Size and Cherenkov Emission

For a large part of the investigations into DirectReco, the `circle_9` setup was used. At a point in the analysis it seemed there were an asymmetry in the amount of PMTs that were hit pointing upwards compared to pointing downwards. Investigations into this asymmetry lead to the discovery that the custom detector setup was simply too small. My faulty initial thoughts were that electrons produced almost spherically symmetric cascades, from the EM shower, but that is not the case. An electron will produce a Cherenkov ring, though a little more fuzzy than that of the muon, and therefore does have a directional asymmetry from the vertex. This directional asymmetry was also found to be the reason for the PMT asymmetry. From these investigations, it was coincidentally also found that the initial custom detector, `circle_9` was too small to receive most of the light. The Cherenkov wavefront determines where most of the light is deposited, so by plotting the expected Cherenkov wavefronts together with the detector, it is possible to see where we expect the largest light yield. In the top plot of Fig. 8.1, there is an illustration of two strings in the `circle_9` detector with the measure of total charge received in the PMTs in a simulation, a 50 GeV electron assumed to be traveling in a straight line in 10 ns, and the Cherenkov wavefronts calculated from trigonometry in Section 3.4. The bottom part of the Cherenkov wavefronts is extended to see where the first light from the emission will hit. The ice was assumed to have a refractive index of $n = 1.31$.

Using this, very rough, estimate it is can be seen that a lot of the Cherenkov light will escape the detector. A new detector, `circle_40` was made and these same calculations were done, and it is seen in the bottom of

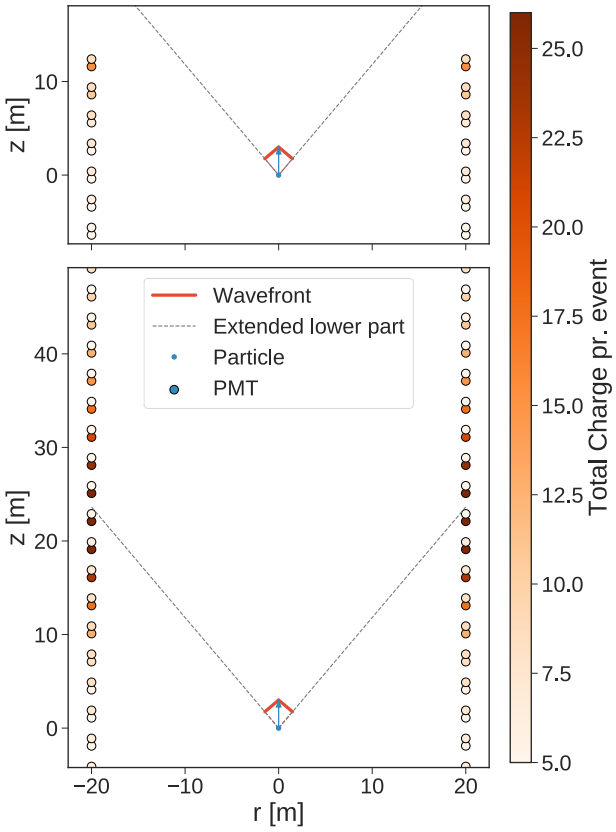

Figure 8.1: A diagram of two types of detectors setups used in the thesis. The predicted Cherenkov cone is drawn with a 50 GeV electron traveling for 10 ns. The D-Eggs are shown as two circles on top of each other, one representing the upwards looking and one the downwards looking. **Top:** Shows the `circle_9` detector. The detector was too small to get hit with the ideal amount of light. **Bottom:** Shows a smaller part of the `circle_40` detector setup. With this setup the optimal light emission from the Cherenkov cone, hits inside the detector volume.

Fig. 8.1. The most amount of charge is seen around where we expect the Cherenkov wavefront. As such, the `circle_40` detector was used for a bit, until I felt confident to move to the `Upgrade_DEgg` for final reconstructions.

8.2 Investigations and Changes

Investigations into DirectReco led to changes made directly to DirectReco, as opposed to only the setup as described in Section 8.1. A few of these changes are directly related to the D-Eggs and some are general DirectReco problems. In this section I will present the problems that were found with DirectReco, some that were never solved, some that were solved with changes, and some

testing that did not solve anything.

8.2.1 PMT Light Yield Acceptance

The simplest method to check if there was any agreement between simulation and the output of DirectReco, was to compare the waveforms of charge and time in each PMT. DirectReco takes no iterative steps in this test and is given the true hypothesis of the simulated particle, and calculates the expected light yield in each PMT. Agreement at this step is important, since it relies completely on DirectReco's ability to find the light yields and there is no dependence on the minimizer, likelihood, or any other effects that are seen in minimization problems.

First investigation into this was done in the `circle_9` detector, still with noise and detector simulation. In these, a general disagreement was found in the shape of distributions as well as an offset in the amount of charge at all times. This initial distribution can be seen on the left of Fig. 8.2. The discrepancy in the shape can be seen more clearly seen in the ratio plot, as the ratio is not constant over time.

The reason for the shape difference was found in the way DirectReco accepted the light into the PMTs. Similar to simulation, DirectReco gets a probability for a photon to be accepted by the PMT by multiplying the photon weight, wavelength acceptance and angular acceptance together. Dissimilar to simulation, DirectReco aims to produce a probability-density-function (PDF) of the expected light yield by simulating the event multiple times (oversampling), and does so by simply adding this probability divided by the oversampling into the PMT. For D-Eggs, the choice of PMT to be hit by a photon in DirectReco was taken to be the one which had the smallest angle between the PMT normal and the incident photon. Choosing only one PMT to be hit, produced a wrong PDF. The fix was to simply calculate the probabilities for accepting the photon in either PMT and adding this probability into each PMT, without discarding any. This change produced waveforms that had a much better agreement, but there were still a discrepancy. The comparison after the acceptance change can be seen on the top-right of Fig. 8.2.

8.2.2 Ice models in DirectReco

Anyone who has programmed, knows the dread of locating a bug hidden deep within the thousands lines of code. This only worsens if the code you are reading was not written by yourself. The factor of around 1.9 in difference between the light yield of the simulation and DirectReco was one of these

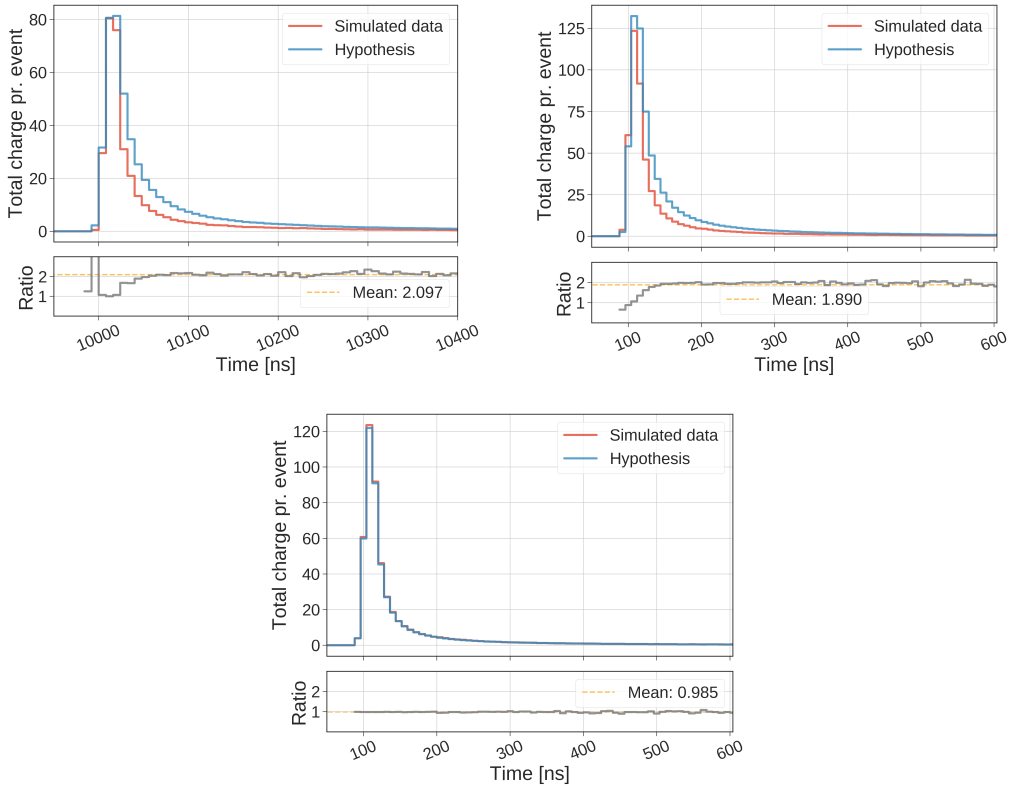

Figure 8.2: The sum of all pulse waveforms from the 90 PMTs in the `circle_9` custom detector. The plots are averaged over 800 events and DirectReco was run with an oversampling 100. The ratio is hypothesis over data. **Top Left:** Initial waveform plot from before any changes. **Top Right:** Waveform plot after the change to the way in which a photon is applied to D-Eggs described in section 8.2.1, as well as removal of detector simulation. **Bottom:** After removal of noise and detector simulation, the change to the the single photon yielding light in both PMTs, and both using the same ice model.

bugs. Because it looked close to a factor of 2, and it was only seen with ICU reconstruction, it was hypothesised that it was somehow specific to the D-Egg. Extensive testing was done to see if there were a difference in the simulation and DirectReco when handling D-Eggs. Nothing was found, even after removal of noise and detector simulation.

It was finally found to be caused by a difference in the ice model used in simulation and DirectReco. When simulation was run for the ICU an ice model with homogeneous ice was used by default, instead of the realistic ice model used in DirectReco. The homogeneous ice was used in ICU simulation since the table reconstructions that were generated in the non-ICU, could be re-used by using a trick which required the ice to be homogeneous. Changing

the ice model in simulation to a realistic ice model, fixed the large discrepancy in the light yield, as seen in the bottom of Fig. 8.2.

In simulation the D-Eggs use a hole ice parameterization called `as.nominal`. The effect of this is is small, but the parametrization was also implemented into DirectReco. It showed to have very little effect, only changing the mean of the ratio from 0.985 $\rightarrow$ 0.990. This change in the mean ratio was so small that it might be from the stochastic nature of the generated data, nevertheless, this change was kept for the final run, since it should be more correct.

8.2.3 Likelihood Stability

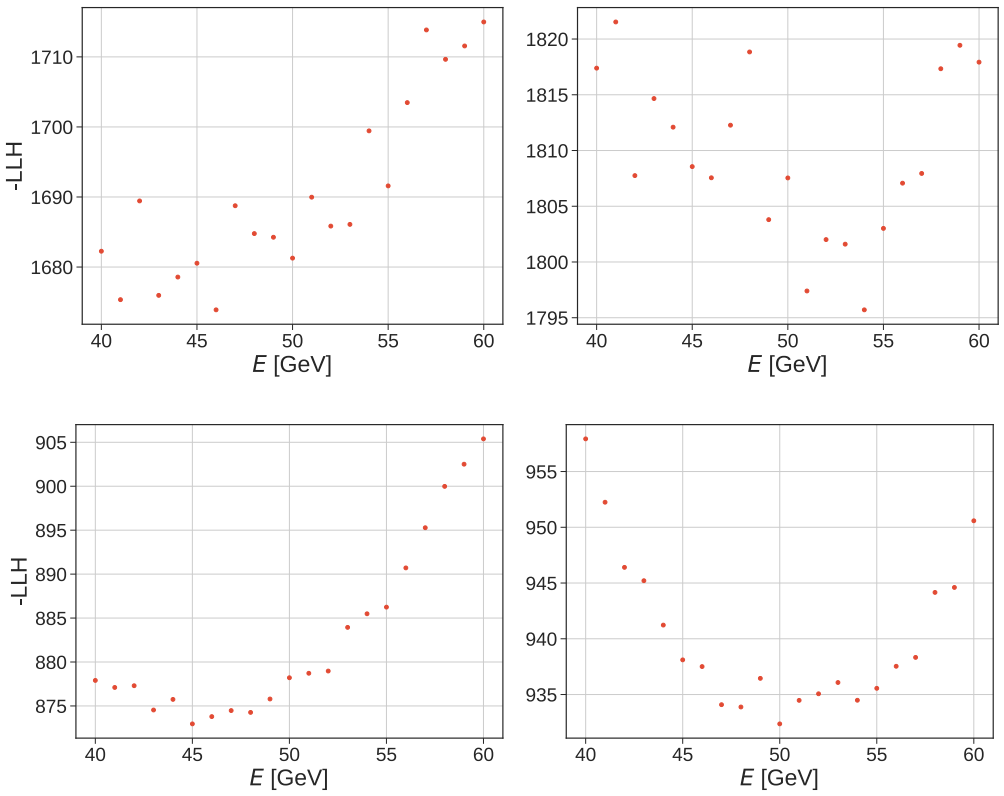

Figure 8.3: Likelihood scans of 2 events, using two different types of binning. The true energy is at 50 GeV. An oversampling of 500 was used. **Top:** Shows the likelihood scan of 2 events using the regular uniform binning with a bin width of 8 ns totalling 87 bins. **Bottom:** Same two events, but using logarithmic binning with only 13 bins.

Using the implemented changes to DirectReco described in Section 8.2.1 and 8.2.2, and moving to the `Upgrade_DEgg` detector setup, the reconstruc-

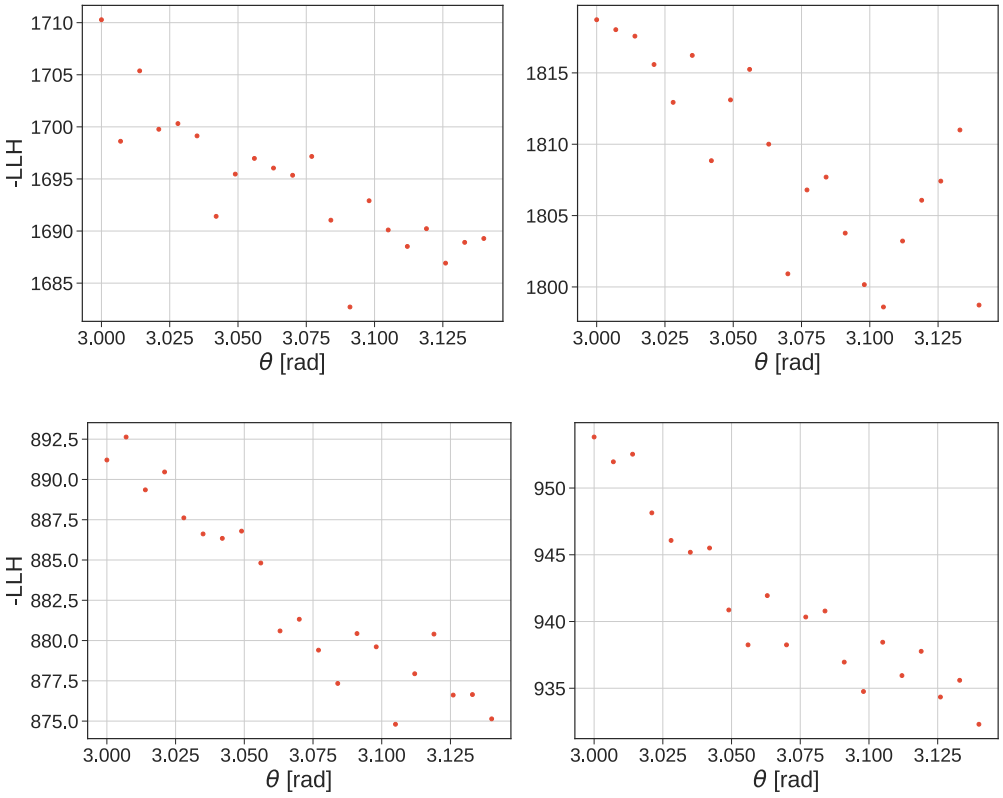

Figure 8.4: Likelihood scans of 2 events, using two different types of binning. The true zenith, (θ), is at π. An oversampling of 500 was used. **Top:** Shows the likelihood scan of 2 events using the regular uniform binning with a bin width of 8 ns totalling 87 bins. **Bottom:** Same two events, but using logarithmic binning with only 13 bins.

tion tests of the 50 GeV electron using 100 oversampling showed accurate results for most parameters, although, the energy reconstruction showed to have the most problems. Sampling the energy seed uniformly in the range of 0 GeV to 100 GeV, the energy reconstruction got a mean of 53.88 GeV and a standard deviation of 22.42 GeV. Comparing this to the mean of the seed, which was 52.77 GeV for the mean and 27.61 GeV for the standard deviation, the reconstruction of the energy showed very little improvement in terms of precision and showing worse results than the random seed in terms of accuracy. To investigate this, likelihood scans were produced on single events, to see if the stability of the likelihood space did not allow for better reconstructions. The likelihood scans were produced by in DirectReco by fixing the true values for each parameter except the parameter to be scanned, which was given value to be scanned. Restricting DirectReco to only calculate the light yield and not do any minimization, the likelihood could be computed

for each scan point. Two such likelihood scans can be seen for energy (E), in the top of Fig. 8.3, and for the zenith angle (θ) in the top of Fig. 8.4. The bottom plots in both figures are from a log binning which will be explained further down in this subsection.

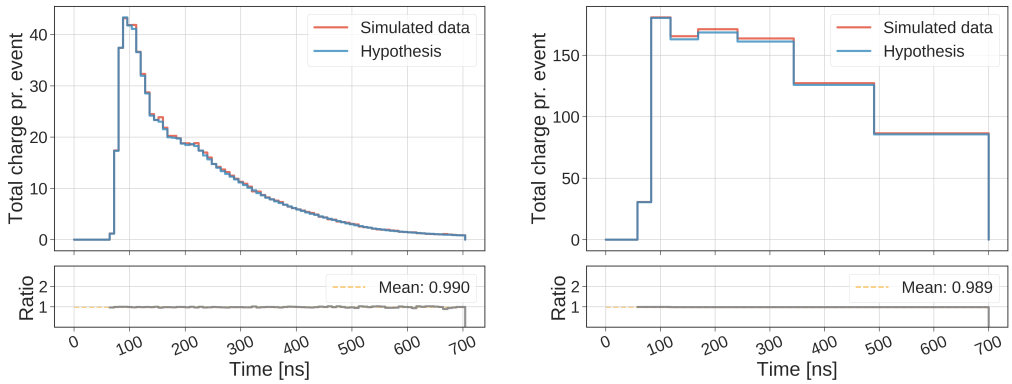

Figure 8.5: The total charge from all PMTs per event averaged over 400 events. The hypothesis is made using an oversampling of 100. **Left:** Shows the uniform binning with bin widths of 8 ns. totalling 87 bins. **Right:** Shows the log binning with only 13 bins in total.

An ideal stable likelihood space of this kind, would show a smooth curve with a single minimum at the true value of the scanned parameter. This was not the case, with the initial energy scan having large amounts of local minima and no clear global minimum at the truth value, even with the oversampling of 500 that was used for the scan. Increasing the oversampling showed clear improvements in the likelihood stability, but larger oversampling comes at a cost of computational time. The reconstruction of this upgoing 50 Gev electron that was simulated in these tests, took $\sim$ 17 min to reconstruct with 100 oversampling. Increasing this above an oversampling of 10 000 would require larger amounts of time, increasing the reconstruction time by a factor of 100, coming in at 28.5 hours per electron event. The binning method of millipede was investigated to see if the likelihood space could be affected by changing the way in which pulses were binned. Since energy should be closely related to the deposited charge in the PMTs, only looking at a single bin spanning all time, containing the total charge in each PMT, showed an incredible stable likelihood space in energy, which can be seen in Fig. B.1 in the appendix. With no time information, it would be impossible to reconstruct vertex time, and direction would suffer as well, but the test showed that the likelihood space for energy could become more stable using a different binning. Since there is more stochasticity in the bins with

low statistics, it was decided to try a logarithmic binning, with small bins at small times and larger bins at later times. To capture really early pulses two 10 ns bins were inserted in the beginning before the logarithmic binning started. An example of the total light yield from simulation and DirectReco given the correct parameters can be seen using the initial uniform binning and the logarithmic binning in Fig. 8.5. The likelihood space for the energy after the change can be seen in the bottom of Fig. 8.3, and for the zenith angle in the bottom of Fig. 8.4.

Using the logarithmic binning, the energy likelihood space was more stable, with less local minima, and a much clearer global minimum. Even the zenith angle likelihood space improved from the change. With the likelihood space, showing a much more stable nature, the change to logarithmic binning was kept for the final reconstruction in Section 8.3.2.

8.2.4 Bimodality of the iteration distribution

During reconstruction with DirectReco, it was found that the distribution of the number of iterations that the minmizer used before terminating was bimodal. The reconstructed values from those with higher iterations, were better performing than for those that used less. This could also be seen in the extracted negative log-likelihood values, showing smaller values for the events with higher iterations. Another measure which showed a clear bimodality was nmini, which is the measure of the amount of times the likelihood was evaluated during a reconstruction. The amount of times the likelihood was evaluated each iteration, might differ depending on the action of the minimizer, but in general this number would be around two. Therefore nmini and iterations are very related, which is also why they both show a clear bimodality. It was found that the split between the two peaks was around nmini $= 50$, so this value is used when separating the two populations. An example of this can be seen in Fig. 8.6, showing the two populations divided into two at nmini $= 50$.

To figure out what caused the bimodality, extensive testing was done, but the cause was never found. Nevertheless, from the testing, some things can be ruled out. To check if it is related to some specific simulated events, the reconstruction was run multiple times on the exact same simulated data, but the bimodality was still there. The outcome of this test is what is seen in Fig. 8.6. The figure that shows two populations in nmini and it is seen in the likelihood distribution as well.

Reconstructions in the `circle_9`, `circle_40` and `Upgrade_DEgg`, all showed bimodality. Simulating random positions, directions and energy for the electron, still resulted in the bimodal distribution as well. This test and the

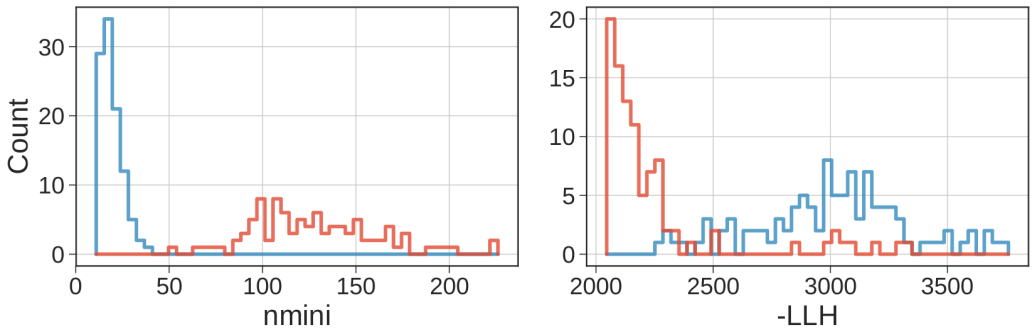

Figure 8.6: The distributions for nmini and the negative log-likelihood for the reconstruction of 200 of the exact same simulated events. The distributions have been split into two, with blue for nmini ≤ 50 and red is for nmini > 50.

test of reconstructing the same event suggests that it is independent of the simulated electron parameters.

Millipede can be provided with a minimizer tolerance, which supposedly, is multiplied onto the convergence check in Eq. 6.9, so that one can require an even smaller EDM than is required by default. Changing the tolerance showed no difference, neither with a higher value nor a lower value. The bimodal distribution was still apparent.

The minimizer might meet its convergence, if it finds a local minima and gets stuck. This can happen if the likelihood space is unstable or multimodal. From likelihood scans in the single parameters, no multimodal likelihoods were found, and from Fig. 8.3 and Fig. 8.4, the likelihood space does not look to be too unstable to traverse. While the left figure of Fig. 8.3, does seem to have its minimum at the wrong value of 45 GeV, with a standard deviation of around 22 GeV from the reconstructions, one such minimum with 5 GeV off from the truth is not the cause of the bad energy reconstructions but rather the minimizer doing the wrong thing. The multidimensional likelihood space could look different than what is, and be more unstable, than the idealized 1-dimensional scans that has been shown, but more evidence that the minimizer is the culprit, is explained in the next section, Section 8.2.5. Ultimately, the exact reason was never found, but should be investigated further, as there is a divide, with the higher nmini showing better performance.

8.2.5 Likelihood scans on reconstruction parameters

From the bimodality of the nmini distribution described in last section, it was interesting to try and investigate the likelihood space that the minimizer was trying to find the minimum of. The prior scans were made with the non-scanning parameters fixed at the truth, while scanning the likelihood

space over the scan parameter. These scans will produce the optimal likelihood space, but that is not what the minimizer will see. It is trying to minimize in a 7 dimensional space, where it is not seeded with the truth parameters, so the space would look different. For this reason, new likelihood scans were produced over events where the reconstruction had already been run. These scans were then run with the non-scanning parameters fixed at the final reconstructed values. In this way, it should be possible to see approximately how the likelihood space in one parameter looked before the minimize terminated. For comparison, these same events, were also scanned with non-scanning parameters fixed at the truth. Both types of scans on energy, of two separate events, can be seen in Fig. 8.7, where the two top figures are with the non-energy parameters fixed at the truth, and the two bottom figures are the same events, but with the non-energy parameters fixed at the final reconstructed values. Both events are simulated with the same setup.

The event on the right seem to largely agree in the shape of the energy likelihood in both scans. The seed was started at 70 GeV while the truth is at 50 GeV, and the final reconstructed value seem to have found a value close to that. It also seems to have found a local mimimum which is present in both the top and bottom figures. The left figures, seeded almost perfectly at 50 GeV, but the reconstruction moved away from that, to a worse value. From the truth scan one would expect the reconstruction to terminate without moving much, but instead it moved to a place which does not have a lower value that it was seeded with. More worryingly, the scan in the lower plot, shows a decline towards lower energies. While the minimum is not at the correct value, the more worrying part of the plot is that the minimizer decided to terminate, instead of following the decline, even though no clear local minimum is seen. This behaviour suggests that the minimizer is not doing what it is supposed to, and therefore the minimizer should be investigated further, to understand this behaviour.

In Fig. 8.8 the same two events have been scanned over z, with one scan having the non-scanned parameters fixed at truth and another with the reconstructed parameters. In the plots we can see that the left event does a better reconstruction as opposed to the right event where the reconstruction stays at the seed. This is opposite of what was seen in the energy. It does not look like there is any local minimum in z in the right plot, where it gets stuck, so once again, this shows that the minimizer is not doing what is expected. On the left figure where it works, it does find a value close to the minimum seen in the bottom figure. More likelihood scans on the reconstructed parameters can be seen in Appendix B.

A few settings given to the minimizer were tested to see if better re-

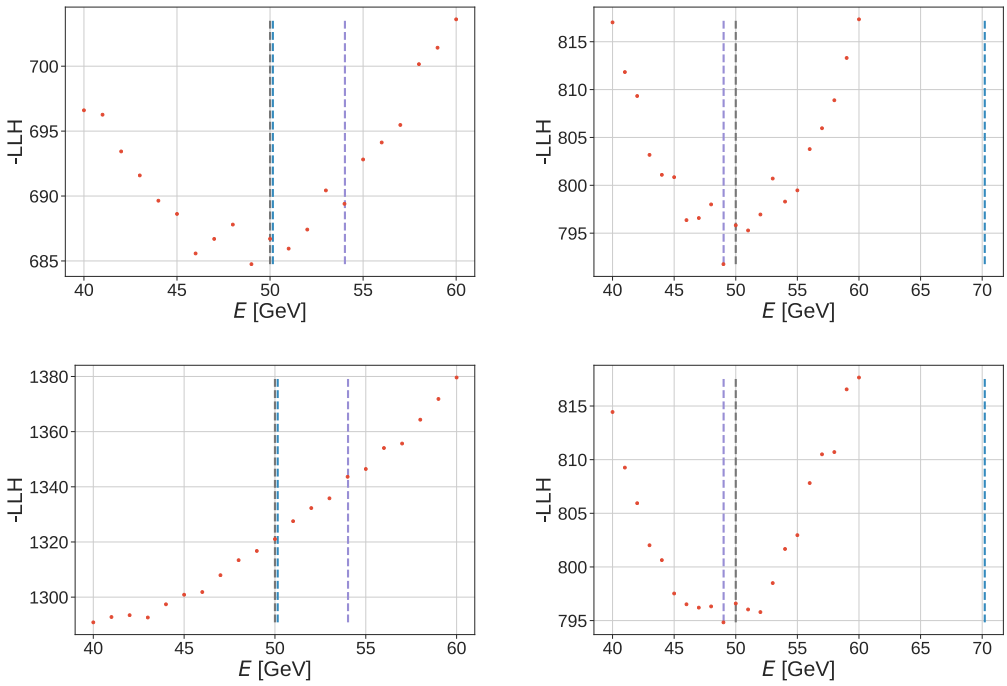

Figure 8.7: Energy likelihood scans on 50 GeV electron events that have been reconstructed using DirectReco with an oversampling of 1000. The scan points are the red, the initial energy seed is the blue dashed line, the purple dashed line is the reconstructed energy and the gray dashed line is the truth value. **Top:** Shows the scan of two events on the left and right, where the other parameters were set to their truth values while scanning in energy. **Bottom:** Shows the same two events but where the parameters were set to their final reconstructed values while scanning in energy.

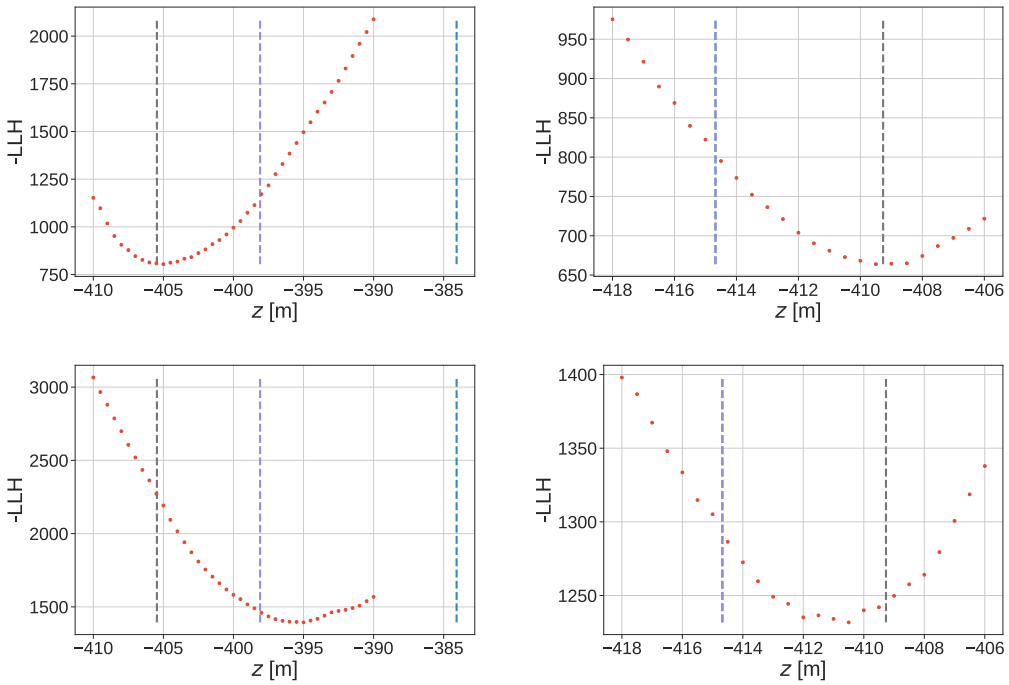

Figure 8.8: Z likelihood scans on two events that have been reconstructed using DirectReco with an oversampling of 1000. The scan points are the red, the initial z seed is the blue dashed line and the purple dashed line is the reconstructed z, with the gray dashed line being the truth. **Top:** Shows the scan of two events on the left and right, where the other parameters were fixed at their truth values while scanning in z. **Bottom:** Shows the same two events but where the other parameters fixed at their final reconstructed values while scanning in z.

construction were found given some changes. These included changing the tolerance, which did not help. Another was setting the `minuitStrategy` which is described to optimize for accuracy as opposed to speed when set to a value of 2. This was tested, and no difference was found in the results. Another option was the `ignoreEDM`, which can by its name suggest that it forces the minimizer to keep minimizing even when estimated-distance-to-minimum (EDM) is small, which might have been helpful. This is not the case and it is described to set the EDM as converged if the maximum EDM is reached, as opposed to either fail or keep iterating. From this description no difference is expected when changing it, but it was tested anyway, and showed no difference. Further investigations into the minimizer should be conducted in the future.

8.3 High Statistics Run

As a final test of the performance of DirectReco, it was set to reconstruct events for a whole week, to have reconstructed 915 events, with a single event taking between 30 to 60 minutes to reconstruct for the specific setup and an oversampling of 1000.

8.3.1 The events and the setup

The custom detector that was used, was the `Upgrade_DEgg` to simulate as close to the actual ICU as possible, while still only using D-Eggs. For the simulated events, an electron was used where the parameters were randomly drawn from a uniform distribution for each event. The energy was drawn between 10 GeV to 50 GeV, the zenith angle was uniformly drawn from $\cos(\theta)$ between -1 and 0, since only upwards going events are of interest to low energy oscillation studies. The azimuth angle, ϕ, was drawn randomly between 0 and 2π, and z between -430 and -230 so to only reside in the ICU and DeepCore depths. The x and y the positions were drawn uniformly from a circle around string 88 at a max radius of 33 meters, so to only be placed inside DeepCore and the ICU. The vertex time was set to be 0 for all simulations. The exact distribution of all 915 events can be seen in the appendix in Fig. D.1, and the x and y placement can be seen in relation to the ICU and DeepCore strings in Fig. 8.9.

For DirectReco an oversampling of 1000 was used, as well as all changes described in Section 8.2. Since there were still problems with energy, and late time seeding has generally shown to produce flat likelihood spaces, it was decided to exclude time from the fit and fixing it to the truth value.

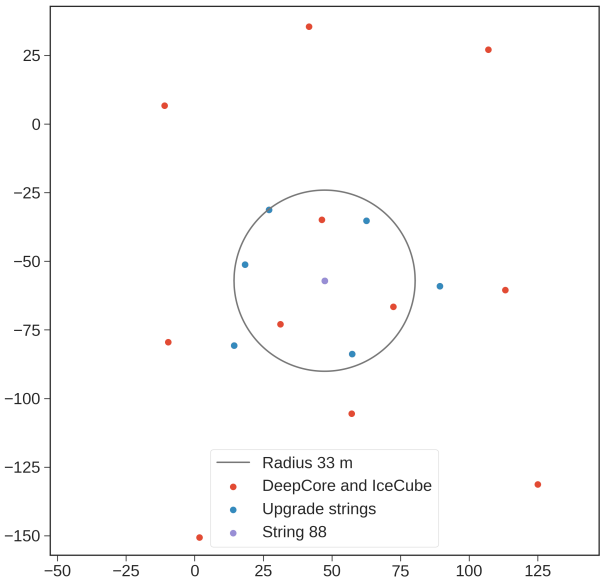

Figure 8.9: The placement in x and y as compared to the ICU and DeepCore strings.

As such, the space to be fitted was only 6 dimensional as opposed to the 7 normally seen in a cascade reconstruction.

To make a more realistic seeding choice for this reconstruction, functions that are used for quickly finding a seed, were used. For the x, y, and z positions COG was used and for direction SPE Fit was used. Both are described in Section 6.4. No obvious function existed to seed the energy of an electron, so the energy was seeded using a function specifically made for this setup. This function took the observed charge in the detector and output an energy. To construct such a function, the expected amount of charge to be observed at the energies 10 GeV, 30 GeV, 50 GeV, 70 GeV and 90 GeV were found by simulating 2000 events of an electron at the given energy, and all the other parameters drawn from the same random distributions as described above. For every single energy, the median was extracted from the total charge distribution of the 2000 events. The relation between energy and total observed charge was assumed to be linear and the medians were fit to a linear function, $y = ax + b$ where y is the total charge and x the energy. The simulated points and the linear fit can be seen in Fig. 8.10. The slope coefficient was found to be 22.28 and the intersection at 20.95. To seed the energy, the function is simply inverted and the total charge of a given event

is put in, and the energy from the output is the seed.

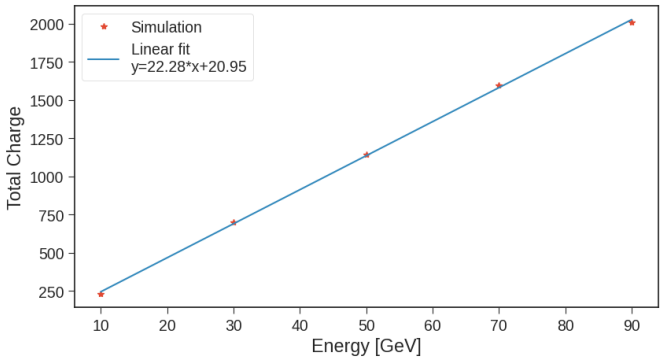

Figure 8.10: The linear function that was used for seeding the energy in the final reconstruction.

By the use of realistic seeding, it is expected that the number of iterations required by the minimizer to reach convergence is smaller than given a random seed, since the realistic seeding should be closer to the true value. But, in the case that the seeding is far away from the truth, it should still be possible to recover a good reconstruction value using more iterations.

8.3.2 The results

The final reconstruction results can be seen in Fig. 8.11. The medians of all distributions as well as the negative and positive width $\sigma_{\pm}$, each describing the distance from the median in which 34.14% of the data resides, can all be seen in Table 8.1.

The results still show bimodal distribution in nmini, so the two populations have been separated at nmini=50, to see if they differ in performance. In Fig. E.1 and Fig. E.2 in the appendix the distribution of seeding and the distribution of true parameters split at nmini=50 can be seen.

The likelihood of the two distributions show an overlap but the population with small nmini shows better performance with a median of 704.8 as opposed to the median of 1407.5 from the nmini ≤ 50 population, with the medians being within 1.16 σ significance of each other. A large difference between the two populations is also seen for the reconstructed parameters, with a better performance by the large nmini reconstructions. The medians of all, but the zenith angle, is more closely centered at 0 and the widths are smaller for all parameters with nmini > 50 as compared to the nmini ≤ 50 reconstructions. The median of the zenith angle in the nmini > 50 population is further from 0 than for nmini ≤ 50, but the lower width is smaller by a factor of

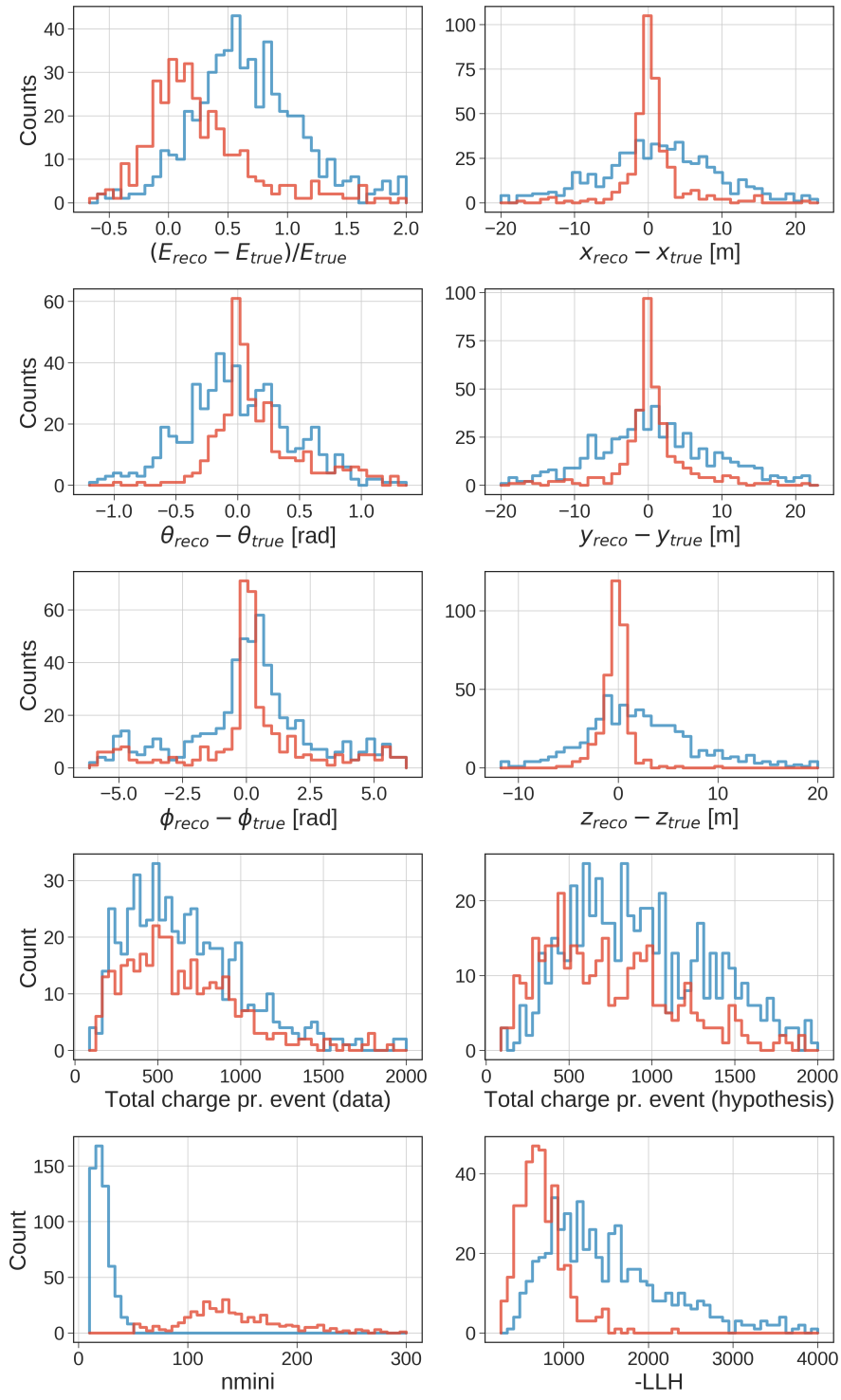

Figure 8.11: The reconstructed parameters of 915 simulated electron events in the `Upgrade_DEgg` custom detector using DirectReco. The simulated parameters of the electron and the seeding are described in Section 8.3.1. All reconstructed parameters have been split whether it used nmini less than or larger than 50. Red is for nmini > 50 and blue for nmini ≤ 50.

Metrics from Fig. 8.11	nmini $\leq$ 50 [$n = 563$]			nmini $>$ 50 [$n = 352$]		
	Median	σ_-	σ_+	**Median**	σ_-	σ_+
$(E_{reco} - E_{true})/E_{true}$	0.643	0.383	0.507	0.160	0.274	0.485
$\theta_{reco} - \theta_{true}$	-0.020	0.411	0.450	0.064	0.169	0.440
$\phi_{reco} - \phi_{true}$	0.258	2.352	1.828	0.119	1.682	1.697
$x_{reco} - x_{true}$	1.401	8.517	7.836	0.198	1.484	2.079
$y_{reco} - y_{true}$	0.861	8.016	9.083	0.199	2.283	3.175
$z_{reco} - z_{true}$	1.736	4.281	5.326	0.104	1.088	0.677
Total Charge per event (data)	612	283	406	575	261	387
Total Charge per event (hypo)	916	388	609	696	355	529
-LLH	1407.5	546.9	1038.3	704.8	213.0	267.6

Table 8.1: The median values, and the widths, $\sigma_\pm$, describing the distance from the median wherein 34.14 % of the data lies within, for all parameters in Fig. 8.11. The distributions are not symmetric around the median, so widths include both toward negative values, σ_-, and towards larger values, σ_+. The distributions are split at nmini equal 50 and therefore the median and widths are also separate for the two distributions.

6.4, while still having 0 within its 1σ bound. The reconstructed azimuth angle is a strange parameter, because a difference between the truth and the reconstruction can be 2π and still be a good reconstruction because of the cyclic nature of the azimuth angle, where an angle of 0 is equal to 2π. The distribution of the azimuth angle can therefore have small collections of reconstructions at the end points, -6.28 to 6.28, which is also seen in the distributions in the Fig 8.11.

The energy distribution of the nmini $\leq$ 50 population has a significant offset from 0, with a median of 0.643 and a lower width of 0.383, differing from 0 with 1.68 σ_-. This suggests that the minimizer overestimates the energy when reconstructing. The median of the energy in the nmini $>$ 50 population does not show such a significant offset.

The total charge per event of the MC data does not differ by more than 0.08 σ between the nmini populations. This suggests that the nmini of a reconstruction, does not depend on the charge of the data. This was also seen with the test done in Section 8.2.4, where the same event was reconstructed multiple times, and still saw bimodality in nmini. The median of the total charge per event for the hypothesis, has a 0.33 σ difference. Comparing the data charge and the hypothesis charge, for nmini $\leq$ 50, their medians differ by 0.54 σ, while for the nmini $>$ 50 population differ by 0.23. The median of the hypothesis charge is especially larger for the nmini $\leq$ 50 compared to nmini $>$ 50, which corresponds well with the overestimation of the energy seen in the nmini $\leq$ 50 population.

For the nmini > 50 population a skew in the energy and zenith angle towards larger values is seen. The difference in the lower width and the larger width are larger by a factor of 1.77 for energy and 2.60 for the zenith angle. This skew, with medians close to 0, means that when the reconstruction overestimates, they spread out towards larger values more than they spread towards lower values when underestimating. These skews can come from a skew in the initial seeding or from a flatter likelihood space above the truth value. A flatter likelihood space in energy at larger energies has been seen before. This is not clear from the scans on zenith seen in Fig. C.3 in the appendix whether that is the case for zenith. Further scans should be done, to reach a firmer conclusion whether the flat likelihood is the reason for the skews.

Focusing only on the nmini > 50 population, these results show that it is possible in this setup to reconstruct more than 68.2% events within a zenith angle of 0.5 rad from the truth, the x, and y positions within 3.4 m of the truth and the z position within 1 m of the truth using DirectReco. The relative energy difference can be reconstructed within 0.645. The azimuth parameter, is affected by its outer peaks so a better performance than what immediately is seen from the median and widths in Table 8.1, is expected, but purely from this table the azimuth can be reconstructed for more than 68.2% events, within 1.82 rad.

These results show interesting tendencies, with skew in the distributions as well as a difference in the performance two nmini populations. But the results might depend largely on the seed, so plots were produced with the correlation between the reconstructed value and the seed value as shown in Fig. 8.12.

In these correlation plots, if a reconstruction did not move away from seed it would lie on the 1:1 line, and if it reconstructed exactly to the truth, it would lie on the y=0 line. Evident from all of the parameters, is that a lot of the reconstructions with nmini ≤ 50 stay on, or close to, the 1:1 line, suggesting that they are either not moving at all, or only a tiny bit. For the nmini > 50 reconstructions, they show a better exploration of the space as well as a better final reconstruction value. In the two parameters that seem to have most difficulty to move away from the seed, energy and azimuth, a tendency to move above the seed is seen for the nmini ≤ 50 population, independently of whether the truth value is larger or smaller than the seed. This can suggest that the minimizer prefers to move to higher values, that it meets a local minimum at higher values, or that the initial steps are towards higher values. The latter explanation should not generally be the case from the description of the SIMPLEX method, which just reflects the worst SIM-

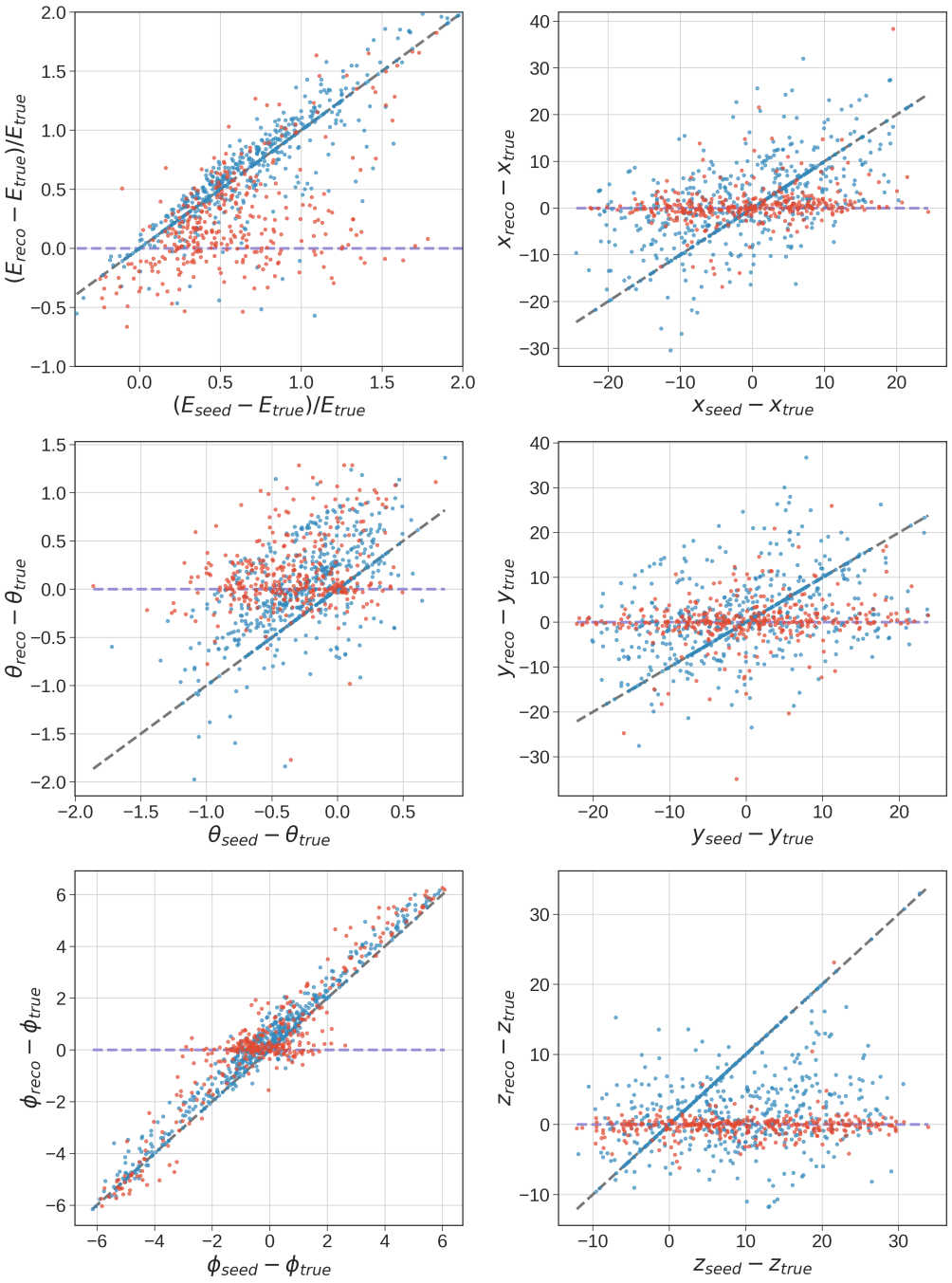

Figure 8.12: A scatterplot showing the seeded value and the reconstructed value. The red points are for nmini > 50 and the blue are for nmini ≤ 50. The best reconstructed values would be if they reconstructed to the true value, so that is seen as the purple line at y=0. If the reconstructed values stayed at the seed and did not move, they would lie on the 1:1 line in the plots, shown as the gray line.

PLEX point past the other points, which should have no preferred direction for a random initialization. The two other reasons depend on the likelihood space, which did not look strange for higher energy values. The exact reason for this tendency is not known, and should be investigated further, when investigating the minimizer.

To better measure the performance of DirectReco, a measure of the difference between the reconstructed value to the truth compared to the difference between the seed value and the truth should be compared. If the reconstruction does not do better than the seed, then the reconstruction would be obsolete. Therefore, to get a better sense of the reconstruction performance, the absolute ratio of the distance between reconstruction and the truth over the difference between the seed and the truth, $y = |(reco - true)/(seed - true)|$, is plotted in Fig. 8.13, and specific metrics for this ratio, are seen in Table 8.2.

Metrics of $\frac{reco-true}{seed-true}$ from Fig. 8.13

Parameters	**nmini $\leq$ 50 [$n = 563$]**					**nmini $>$ 50 [$n = 352$]**				
	Median	σ_-	σ_+	$n_{<1}/n_{total}$	$n_{=1}$	**Median**	σ_-	σ_+	$n_{<1}/n_{total}$	$n_{=1}$
E	1.000	0.164	0.237	0.368	29	0.582	0.480	0.679	0.739	0
θ	1.000	0.712	1.962	0.467	76	0.451	0.361	2.322	0.673	0
ϕ	1.000	0.458	0.686	0.398	76	0.778	0.653	0.578	0.622	0
x	1.000	0.745	0.847	0.556	7	0.187	0.149	0.847	0.832	0
y	1.000	0.791	1.168	0.536	20	0.257	0.225	1.316	0.770	0
z	0.529	0.418	0.471	0.629	135	0.054	0.042	0.218	0.940	0

Table 8.2: Metrics for the measure of performance seen on the y-axis of Fig. 8.13. The distribution is split into two at nmini = 50. The metrics include the median and the negative and positive widths, $\sigma_\pm$, which describe the distance from each side of the median that encompasses 34.14% of the data. $n_{<1}/n_{total}$ is the ratio between the points below 1 and the total points, and $n_{=1}$ is the amount of points with a distance ratio exactly equal to 1 The points exactly on the line are not counted when counting the below 1 points, $n_{<1}$.

In the figure, any points below $y = 1$ are reconstructions that get a better value than the initial seed of those events, while anything above is worse. If points lie directly on the $y = 1$ line, that shows that the reconstruction did not move away from the seed.

The distribution of both nmini populations in z show a tendency to reconstruct, lower z values better than larger values. At the high end of the z range, the dust layer is closer, which also contains a far less dense instrumentation. The fact that some events does worse at higher values, is expected, if

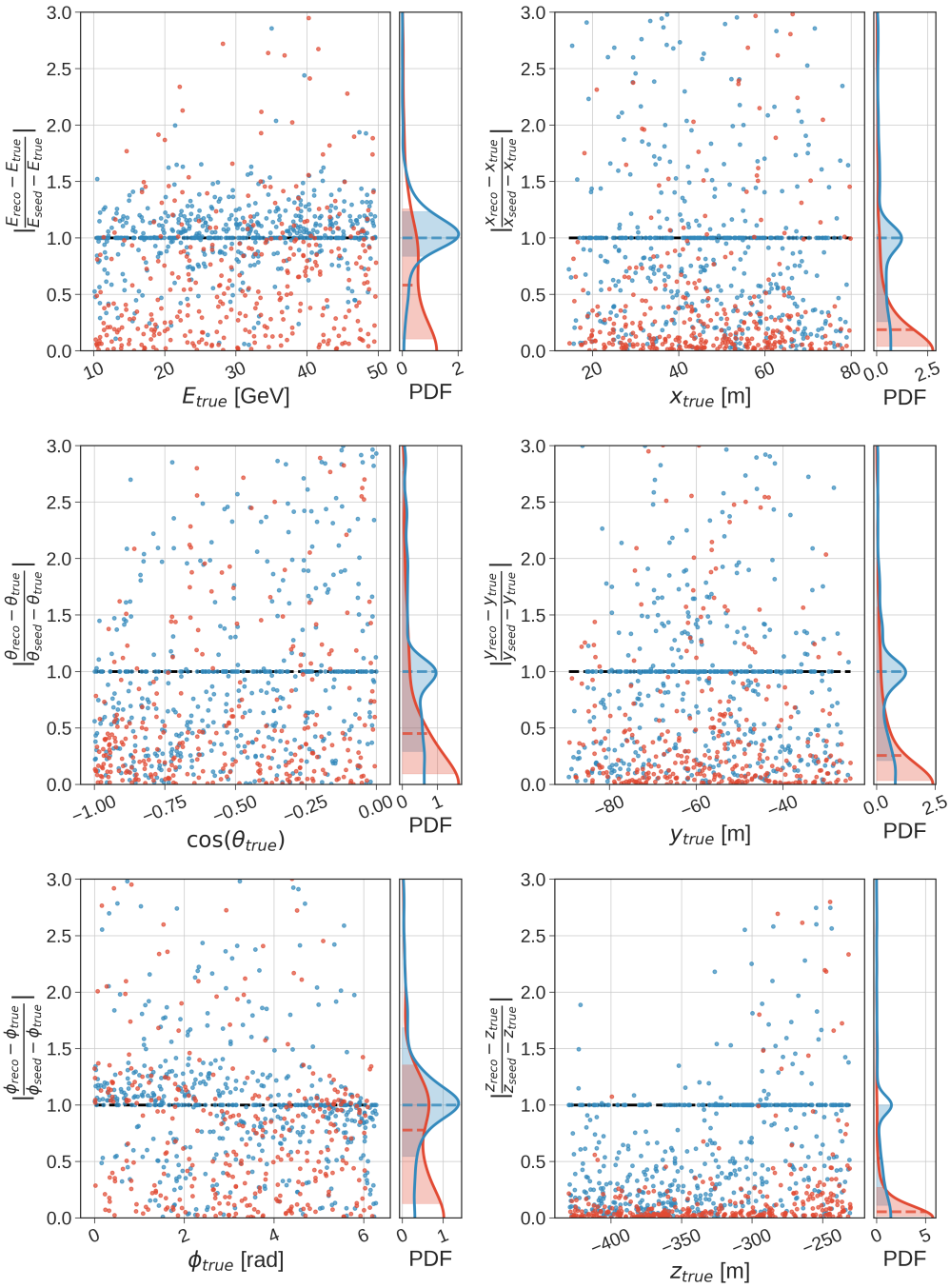

Figure 8.13: The performance of DirectReco as compared to the seed for each event, shown as scatterplots, with a kernel-density-function (KDE) probability-density-function (PDF) shown to the right. The measure of performance is the ratio of the seed and reconstruction distances to the truth. The events are split into two, with blue being for nmini ≤ 50, and red for nmini > 50. The dashed lines of color in the PDF plots indicate the median of the events and the colored area indicates wherein 68.27% of the data lie within. A black dashed line at $y = 1$ indicates the split where reconstructions are doing better than the seed.

the event goes into the dust layer, and less light is deposited in the D-Eggs. The same thing is not seen at the low z values, since the direction of the electron is never downwards, and therefore would never travel outside the bottom of the detector.

Focusing on the nmini ≤ 50 population, a large part prefers to only move very little distance away from the seed or not at all, which was also seen in the correlation plots. All parameters have definite peaks at $y = 1$, and all parameters, but energy, has larger values for the probability-density-function (PDF) below y=1 than above. The reason for these larger PDF values below $y = 1$, most likely comes from the boundary at $y = 0$. With a boundary, given a median of 1, 50% has to be between 0 and 1, as opposed to the 50% points which have values larger than $y = 1$, that can extend infinitely. The medians in Table 8.2 of all parameters, but z, are all suspiciously equal exactly 1. This is caused by the fact that a lot of the reconstructions stayed at the seed, and therefore there are a lot of events with a distance ratio exactly equal to 1. When the $n_{<1}/n_{tot}$ ratio is calculated the points on the $y = 1$ line are not counted for $n_{<1}$ and therefore, this ratio does not have to be 0.5 even when the median is 1. The ratio of points below 1 of the total points, show that energy and directions have less than 50%, and the positional parameters have more than 50%. If no points were exactly at $y = 1$, a 50% $n_{<1}/n_{total}$ ratio would suggest the minimizer moved randomly from the seed. The parameters x, and y are both close to 50% with only a few points on the $y = 1$ line, suggesting close to random movement. The z parameter has more points below than above and 135 of reconstructions directly on the $y = 1$, which suggests the z reconstruction does better than random. While zenith is close to 50%, energy and azimuth are both below, with energy having the smallest amount of points below. This might suggest what was seen in the correlation plots, that moving to the wrong direction in energy or azimuth, can result in the minimizer prematurely terminating. This could be the reason for the two populations, but that needs to be investigated further, to reach a full conclusion.

Turning the attention to the much better performing population of nmini > 50. The median of all the parameters are below 1, with no points on the $y = 1$ line, which means that the largest part of the population is better than the seed, for all parameters. The ratios of points below $y = 1$ to the total also show good results, with the best parameter, z, reconstructing 94% of them better than the seed. Z also has a median 0.05, very close to 0. The x position shows a better performance than y, with a better median and percentage of points below 1. This is unexpected, since the detector should be close to symmetric in the x and y plane. This difference might be from random chance but that is unlikely with 352 events and a difference in the

number of points below $y = 1$ of 22. Looking at the position in x and y in the detector in which the electrons were simulated in Fig. 8.9, a few extra strings is seen in the x direction as opposed to y. The x strings are outside the generation circle, but they can still collect light and contribute, and can be the reason for the better x reconstructions. The direction reconstructions have the lowest percentage of reconstructions below $y = 1$ of 0.622 for the azimuth angle and 0.673 for the zenith angle. The median of the zenith angle is at 0.451 and for azimuth at 0.778. The azimuth median is worse than zenith but the difference is most likely caused by the bimodal nature of the distance ratio as seen in Fig. 8.13, where azimuth has a peak at $y = 1$ and one close to $y = 0$. The peak at 1 is unexpected and seem to suggest that even for this nmini > 50 population, the azimuth angle is still hard to reconstruct. A similar double peak, is seen for the energy as well, which has a median at 0.582 and a ratio of points below $y = 1$ of 0.739. The double peaked distribution of energy and azimuth suggest that they are the parameters which are the hardest parameters to reconstruct, and are prone to staying close to the seed.

Since no analysis level reconstruction methods currently work for the ICU, it is not possible to compare this performance with any other reconstruction method.

8.4 Future Work

The separate populations seen in nmini have shown to divide the reconstructions into a good performing population and a bad performing populations which tends to stay close to the seed. It is possible to redo the reconstructions of the bad performing population, but with $\sim 2/3$ of the reconstruction being the bad performing kind, and time already being a pressing factor, this solution is not a long term solution. Investigations into the bimodality should be one of the next steps.

An issue was found in the minimizer movement in the likelihood space, not doing what is expected. On a steep decline, the minimizer still found convergence and terminated, as was seen in Fig. 8.7. The SIMPLEX minimizer which is used in DirectReco, should therefore be further investigated to find the issue that is causing the unexpected minimizer behaviour.

D-Eggs have been used for all the analysis of this thesis, but the DirectReco light yield in each PMT should also be tested for mDOMs, to see if the expected light yield from DirectReco agrees with the simulation.

The reintroduction of noise and detector simulation should also be studied, by comparing the light yield in the detector to the light yield of DirectReco, without any minimization.

When the former problems have been resolved, and if no further problems arise, advancing to the reconstruction of neutrinos is the next step, as reconstruction of neutrinos is the goal of DirectReco. Since track-reconstruction has yet to be tested, the first step should be cascade neutrino reconstruction.

9 Conclusion

In this thesis DirectReco has been investigated, with a focus on the IceCube Upgrade and specifically the D-Eggs. The light yield generation of DirectReco has been modified to properly work for multi-PMT modules and has shown to have equal light yield in D-Eggs when comparing MC simulation with the DirectReco light yield, when excluding noise and detector simulation.

The likelihood space of a hypothesis has shown to be highly dependent on the binning, showing that a single bin in each PMT can result in a more stable energy likelihood scan as compared to the normal 87 uniform bins. To have time information in the bins, a logarithmic binning has been introduced in Millipede, with smaller bins at small time and larger bins at late times. This also showed an improvement in the stability of energy likelihood and showed no degradation in the stability seen in the zenith angle likelihood scan compared to the 87 bins implementation.

The minimizer of DirectReco was investigated and was shown to inhibit an unexpected behaviour where convergence was met even when on a steep decline.

A reconstruction of 915 events, with no detector or noise simulation, no time reconstruction and with events simulated in a custom Upgrade detector where all optical modules were replaced by D-Eggs, was presented and showed a bimodality in the nmini distribution. Separating the two populations at nmini = 50, showed a clear difference in the two populations, with the small nmini reconstructions doing worse with medians offset from the truth and much more spread out, as opposed to the better performing population with large nmini. It was shown that the same simulated event could be reconstructed with large nmini or small without introducing any change, suggesting that nmini is independent on the simulated event.

Focusing just on the nmini > 50 population, DirectReco could reconstruct more than 62% events better than the seed for all parameters, with z reconstructing 94% events better than seed. From the upper 1σ bound on all parameters, more than 68.2 events reconstructed within 3.3 m from the true vertex position, 0.5 rad from the true zenith angle and 1.8 rad from the true azimuth angle. The energy ratio, $(E_{reco} - E_{true})/E_{true}$ were reconstructed within 0.65 for more than 68.2% events. With azimuth being cyclic, the 1σ widths are probably overestimated, so the azimuth angle is expected to be better than the estimated 1.8 rad value.

The behaviour of the minimizer and the bimodality of the nmini distributions, should in the future be investigated further, as fixing the issues will improve the performance of DirectReco.

10 References

[1] Edoardo Vitagliano, Irene Tamborra, and Georg Raffelt. Grand unified neutrino spectrum at earth: Sources and spectral components. *Reviews of Modern Physics*, 92(4):045006, 2020.

[2] C. L. Cowan, F. Reines, F. B. Harrison, H. W. Kruse, and A. D. McGuire. Detection of the free neutrino: a confirmation. *Science*, 124(3212):103–104, 1956.

[3] R. Abbasi, Y. Abdou, T. Abu-Zayyad, M. Ackermann, J. Adams, J.A. Aguilar, M. Ahlers, M.M. Allen, D. Altmann, K. Andeen, and et al. The design and performance of icecube deepcore. *Astroparticle Physics*, 35(10):615–624, May 2012.

[4] Pauli's original letter. URL: https://cds.cern.ch/record/83282/, Last visited: March 19, 2021.

[5] Pauli's letter - english translation. URL: https://www.radioactivity.eu.com/site/pages/Pauli_Letter.htm, Last visited: March 19, 2021.

[6] P Lipari. Introduction to neutrino physics. page 814, 2003. URL: https://cds.cern.ch/record/677618, doi: 10.5170/CERN-2003-003.115.

[7] Georges Aad, Tatevik Abajyan, B Abbott, J Abdallah, S Abdel Khalek, Ahmed Ali Abdelalim, R Aben, B Abi, M Abolins, OS AbouZeid, et al. Observation of a new particle in the search for the standard model higgs boson with the atlas detector at the lhc. *Physics Letters B*, 716(1):1–29, 2012.

[8] The standard model. URL: https://commons.wikimedia.org/wiki/File:Standard_Model_of_Elementary_Particles.svg, Last visited: April 2, 2021.

[9] Brian Robert Martin. *Nuclear and particle physics*. Wiley Online Library, 2006.

[10] Right and left helicity. URL: https://commons.wikimedia.org/wiki/File:Right_left_helicity.svg, Last visited: April 2, 2021.

[11] Chien-Shiung Wu, Ernest Ambler, Raymond W Hayward, Dale D Hoppes, and Ralph Percy Hudson. Experimental test of parity conservation in beta decay. *Physical review*, 105(4):1413, 1957.

[12] Raymond Davis, Don S. Harmer, and Kenneth C. Hoffman. Search for neutrinos from the sun. *Phys. Rev. Lett.*, 20:1205–1209, May 1968.

[13] Q. R. Ahmad, R. C. Allen, T. C. Andersen, J. D. Anglin, G. Bühler, J. C. Barton, E. W. Beier, M. Bercovitch, J. Bigu, S. Biller, and et al. Measurement of the rate of $\nu_e + d \rightarrow p + p + e$ -interactions produced by b8solar neutrinos at the sudbury neutrino observatory. *Physical Review Letters*, 87(7), Jul 2001.

[14] B. Pontecorvo. Inverse beta processes and nonconservation of lepton charge. *Zh. Eksp. Teor. Fiz.*, 34:247, 1957.

[15] Ziro Maki, Masami Nakagawa, and Shoichi Sakata. Remarks on the Unified Model of Elementary Particles. *Progress of Theoretical Physics*, 28(5):870–880, 11 1962.

[16] M. Aker, K. Altenmüller, M. Arenz, M. Babutzka, J. Barrett, S. Bauer, M. Beck, A. Beglarian, J. Behrens, T. Bergmann, and et al. Improved upper limit on the neutrino mass from a direct kinematic method by katrin. *Physical Review Letters*, 123(22), Nov 2019.

[17] Huaiyu Duan, George M. Fuller, and Yong-Zhong Qian. Collective neutrino oscillations. *Annual Review of Nuclear and Particle Science*, 60(1):569–594, 2010.

[18] U.F. Katz and Ch. Spiering. High-energy neutrino astrophysics: Status and perspectives. *Progress in Particle and Nuclear Physics*, 67(3):651–704, Jul 2012.

[19] J. A. Formaggio and G. P. Zeller. From ev to eev: Neutrino cross sections across energy scales. *Rev. Mod. Phys.*, 84:1307–1341, Sep 2012.

[20] Mark G Aartsen, M Ackermann, J Adams, JA Aguilar, M Ahlers, M Ahrens, D Altmann, K Andeen, T Anderson, I Ansseau, et al. The icecube neutrino observatory: instrumentation and online systems. *Journal of Instrumentation*, 12(03):P03012, 2017.

[21] Picture of a dom. URL: https://commons.wikimedia.org/wiki/File:ICECUBE_dom_taklampa.jpg, Last visited: April 20, 2021.

[22] Diagram of a dom. URL: https://icecube.wisc.edu/gallery/diagrams/#modulagallery-7055-1605, Last visited: April 20, 2021.

[23] Diagram of a pmt. URL: http://analyticalprofessional.blogspot.com/2013/05/photomultiplier-tube.html, Last visited: May 15, 2021.

[24] Photomultiplier tube, r7081. URL: https://www.hamamatsu.com/eu/en/product/type/R7081/index.html, Last visited: April 20, 2021.

[25] MG Aartsen, M Ackermann, J Adams, JA Aguilar, M Ahlers, M Ahrens, C Alispach, K Andeen, T Anderson, I Ansseau, et al. In-situ calibration of the single-photoelectron charge response of the icecube photomultiplier tubes. *Journal of Instrumentation*, 15(06):P06032, 2020.

[26] Rasha Abbasi, Yasser Abdou, T Abu-Zayyad, J Adams, JA Aguilar, M Ahlers, K Andeen, J Auffenberg, X Bai, M Baker, et al. Calibration and characterization of the icecube photomultiplier tube. *Nuclear Instruments and Methods in Physics Research Section A: Accelerators, Spectrometers, Detectors and Associated Equipment*, 618(1-3):139–152, 2010.

[27] Michael James Larson. *Simulation and identification of non-Poissonian noise triggers in the IceCube neutrino detector*. PhD thesis, University of Alabama Libraries, 2013.

[28] HO Meyer. Spontaneous electron emission from a cold surface. *EPL (Europhysics Letters)*, 89(5):58001, 2010.

[29] ANDREA and SILVESTRI. The amanda neutrino telescope. *International Journal of Modern Physics A*, 20(14):3096–3098, 2005.

[30] Markus Ackermann, J Ahrens, X Bai, M Bartelt, SW Barwick, RC Bay, T Becka, JK Becker, K-H Becker, P Berghaus, et al. Optical properties of deep glacial ice at the south pole. *Journal of Geophysical Research: Atmospheres*, 111(D13), 2006.

[31] MG Aartsen, R Abbasi, Yasser Abdou, M Ackermann, J Adams, JA Aguilar, M Ahlers, D Altmann, J Auffenberg, X Bai, et al. Measurement of south pole ice transparency with the icecube led calibration system. *Nuclear Instruments and Methods in Physics Research Section A: Accelerators, Spectrometers, Detectors and Associated Equipment*, 711:73–89, 2013.

[32] Aya Ishihara. The icecube upgrade–design and science goals. *arXiv preprint arXiv:1908.09441*, 2019.

[33] MG Aartsen, R Abbasi, M Ackermann, J Adams, JA Aguilar, M Ahlers, M Ahrens, C Alispach, P Allison, NM Amin, et al. Icecube-gen2: The window to the extreme universe. *arXiv preprint arXiv:2008.04323*, 2020.

[34] Juliana Stachurska. First double cascade tau neutrino candidates in icecube and a new measurement of the flavor composition, 2019.

[35] IceCube Collaboration et al. Evidence for high-energy extraterrestrial neutrinos at the icecube detector. *Science*, 342(6161), 2013.

[36] Dieter Heck, J Knapp, JN Capdevielle, G Schatz, T Thouw, et al. Corsika: A monte carlo code to simulate extensive air showers. *Report fzka*, 6019(11), 1998.

[37] C. Andreopoulos, A. Bell, D. Bhattacharya, F. Cavanna, J. Dobson, S. Dytman, H. Gallagher, P. Guzowski, R. Hatcher, P. Kehayias, A. Meregaglia, D. Naples, G. Pearce, A. Rubbia, M. Whalley, and T. Yang. The genie neutrino monte carlo generator. *Nuclear Instruments and Methods in Physics Research Section A: Accelerators, Spectrometers, Detectors and Associated Equipment*, 614(1):87–104, 2010.

[38] Sea Agostinelli, John Allison, K al Amako, John Apostolakis, H Araujo, P Arce, M Asai, D Axen, S Banerjee, G 2 Barrand, et al. Geant4—a simulation toolkit. *Nuclear instruments and methods in physics research section A: Accelerators, Spectrometers, Detectors and Associated Equipment*, 506(3):250–303, 2003.

[39] Clsim: a photon propagation module. GitHub URL: https://github.com/claudiok/clsim, Last visited: April 26, 2021.

[40] J. Lundberg, P. Miočinović, K. Woschnagg, T. Burgess, J. Adams, S. Hundertmark, P. Desiati, and P. Niessen. Light tracking through ice and water—scattering and absorption in heterogeneous media with photonics. *Nuclear Instruments and Methods in Physics Research Section A: Accelerators, Spectrometers, Detectors and Associated Equipment*, 581(3):619–631, Nov 2007.

[41] M. G. Aartsen, M. Ackermann, J. Adams, J. A. Aguilar, M. Ahlers, M. Ahrens, I. Al Samarai, D. Altmann, K. Andeen, T. Anderson, and et al. Measurement of atmospheric neutrino oscillations at 6–56 gev with icecube deepcore. *Physical Review Letters*, 120(7), Feb 2018.

[42] MG Aartsen, M Ackermann, J Adams, JA Aguilar, M Ahlers, M Ahrens, D Altmann, K Andeen, T Anderson, I Ansseau, et al. Measurement of atmospheric tau neutrino appearance with icecube deepcore. *Physical Review D*, 99(3):032007, 2019.

[43] MG Aartsen, M Ackermann, J Adams, JA Aguilar, M Ahlers, M Ahrens, C Alispach, K Andeen, T Anderson, I Ansseau, et al. Development of an analysis to probe the neutrino mass ordering with atmospheric neutrinos using three years of icecube deepcore data. *The European Physical Journal C*, 80(1):1–16, 2020.

[44] Martin Leuermann. *Testing the neutrino mass ordering with IceCube DeepCore*. PhD thesis, Universitätsbibliothek der RWTH Aachen, 2018.

[45] F. James and M. Roos. Minuit - a system for function minimization and analysis of the parameter errors and correlations. *Computer Physics Communications*, 10(6):343–367, 1975.

[46] J. A. Nelder and R. Mead. A Simplex Method for Function Minimization. *The Computer Journal*, 7(4):308–313, 01 1965.

[47] Thomas S. Halberg. Low energy neutrino reconstruction in icecube and the icu. Master's thesis, University of Copenhagen, 2019.

[48] Dmitry Chirkin. Likelihood description for comparing data with simulation of limited statistics, 2013.

[49] J Ahrens, X Bai, R Bay, SW Barwick, T Becka, JK Becker, K-H Becker, E Bernardini, D Bertrand, A Biron, et al. Muon track reconstruction and data selection techniques in amanda. *Nuclear Instruments and Methods in Physics Research Section A: Accelerators, Spectrometers, Detectors and Associated Equipment*, 524(1-3):169–194, 2004.

[50] Ayumi Kiriki. Detection efficiency of next generation icecube optical module, d-egg, and its sensitivity to optical properties of the antarctic ice with the geant4 based precise photon simulation. Master's thesis, Chiba University, 2020.

Appendices

A Strange Scaling Factors in Simulation

During the implementation of the correct D-Egg acceptance curve, scaling factors of the wavelength acceptances of all modules were found in both Step 2 and Step 3, but the specific scaling factor differed between the two. I did not understand the reason for these when I found them, and it seemed it was unclear what they were there for. Therefore, I will in this small section, present them as they are used, so that they can be investigated further by someone else.

In Step 2, the acceptance curves are used to compute a combined envolope to be used for photon weighting as explained in Section 5.2 and in Step 3, they are used to compute the probability of a photon being converted into a PE as explained in Section 5.3.

For step 2, the scaling of the acceptance α_2, for a given type of optical module m is

$$\alpha_2(m) = 1.15 \cdot \frac{\text{EffeciencyScale}_2(m)}{\text{rqe}(m)}, \tag{A.1}$$

$$\text{rqe}_2(m) = \frac{\text{SensorArea}(m)}{\text{SensorArea(DOM)}}, \tag{A.2}$$

where the values of each variable are seen in Table A.1. The mDOM is furthermore scaled by the square of the mDOM radius over the DOM radius. These scalings and acceptances are then combined into a single envolope.

	DOM	**D-Egg**	**mDOM**
`EfficiencyScale`$_2$	2.2	2.2	2.2
`SensorArea`	29.2 cm	43.3 cm	65.4 cm
`rqe`$_2$	1.00	1.48	2.24
α_2	2.53	1.71	1.31

Table A.1: The specific scaling factors used in step 2 for the different modules.

For step3, the scaling of the acceptances α_3, for a given module m, is

given by

$$\alpha_3(m) = \mathrm{rqe}_3, \tag{A.3}$$

$$\mathrm{rqe}_3(m) = \mathrm{EffeciencyScale}_3(m) \cdot \frac{\mathrm{SensorArea(DOM)}}{\mathrm{SensorArea}(m)}, \tag{A.4}$$

where the rqe's definition is different here than in step 2. The specific values of this is seen in Table A.2.

	DOM	**D-Egg**	**mDOM**
$\texttt{EfficiencyScale}_3$	1.0	1.5	2.2
`SensorArea`	29.2 cm	43.3 cm	65.4 cm
$\texttt{rqe}_3$	1.00	1.01	0.98
α_3	1.00	1.01	0.98

Table A.2: The specific scaling factors used in step 3 for the different modules.

The reason for the 1.15 factor in step 2 is unknown to me. In step 3, the explanation of `EffeciencyScale` is that it is the effective area of the module divided by the DOM area. This ultimately means that when multiplying the `EffeciencyScale` with the sensor area ratio, it almost equals 1, as seen in the rqe_3. In step 2, it seems this `EffeciencyScale` has been set to 2.2, like the mDOM in step 3. The efficiency scaling in step 3, might come from the time when the wavelength acceptance of all the ICU optical modules used the DOM acceptance, so they were then scaled to better represent how the real acceptance curve of such a module would look. If that is the case, then they should be removed, now that the D-Egg has an more realistic curve as well as for mDOM which also has its own now.

The exact reason for all this scaling is unknown to me, and it did seem unclear, when they were presented, whether they should stay or were old artifacts. These factors were also recently presented by Brian Clark, and it seems that they will soon be investigated in more detail.

B Likelihood scans on truth

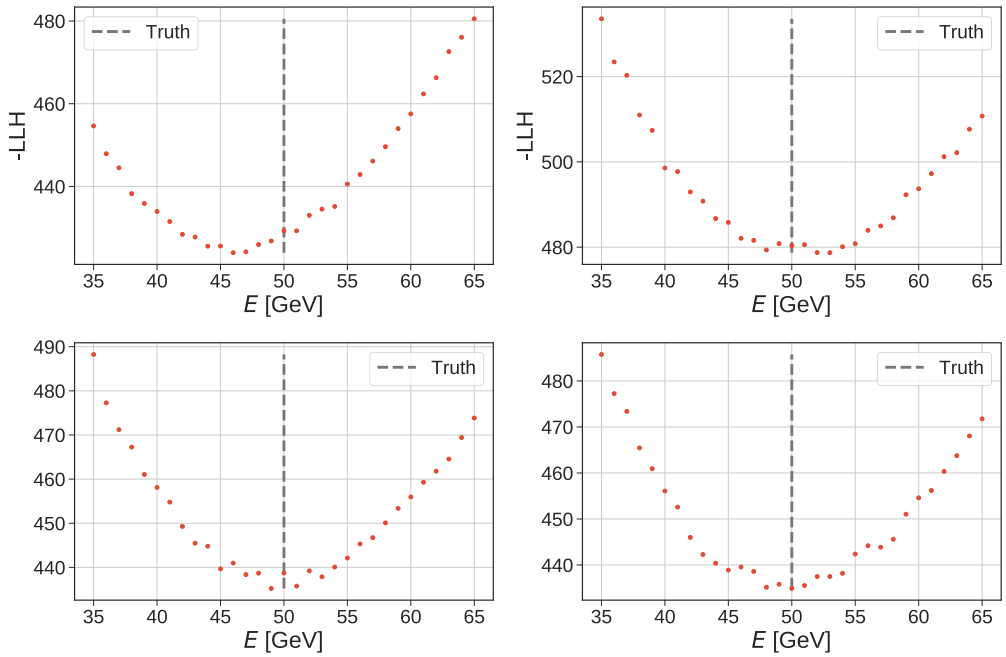

Figure B.1: Energy likelihood scans over electron events with the non-scanned parameters fixed at their truth values. The binning used for this scan was a single bin in all PMTs. The electron was a 50 GeV upwards going electron in the center of the ICU.

C Likelihood scans on reconstruction parameters

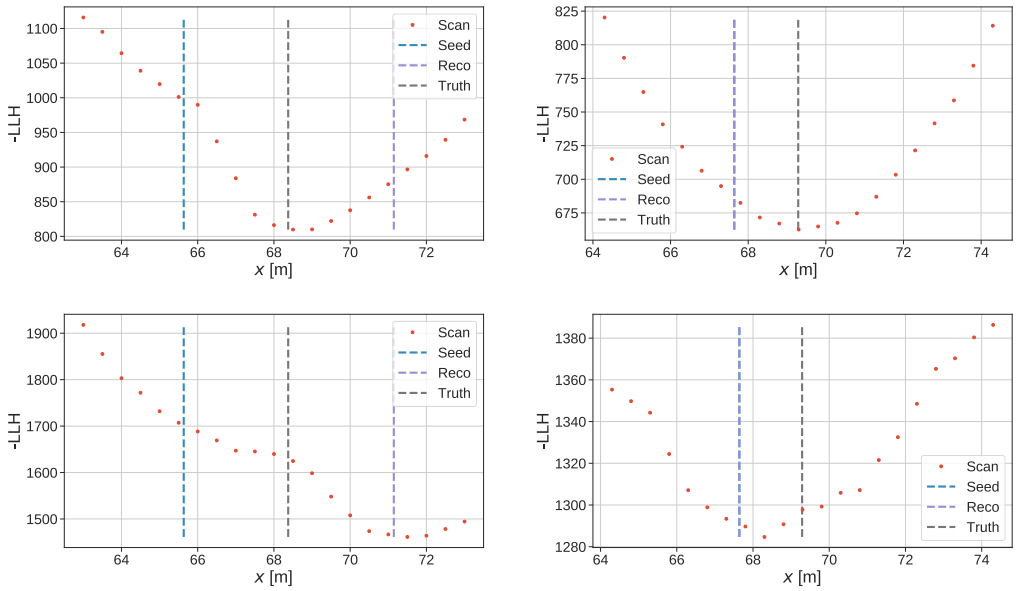

Figure C.1: Likelihood scans on two events that have been reconstructed using DirectReco with an oversampling of 1000. The scan points are the red, the initial seed is the blue dashed line and the purple dashed line is the reconstructed x, with the gray dashed line being the truth. **Top:** Shows the scan of two events on the left and right, where the other parameters were fixed at their truth values while scanning. **Bottom:** Shows the same two events but where the other parameters fixed at their final reconstructed values while scanning.

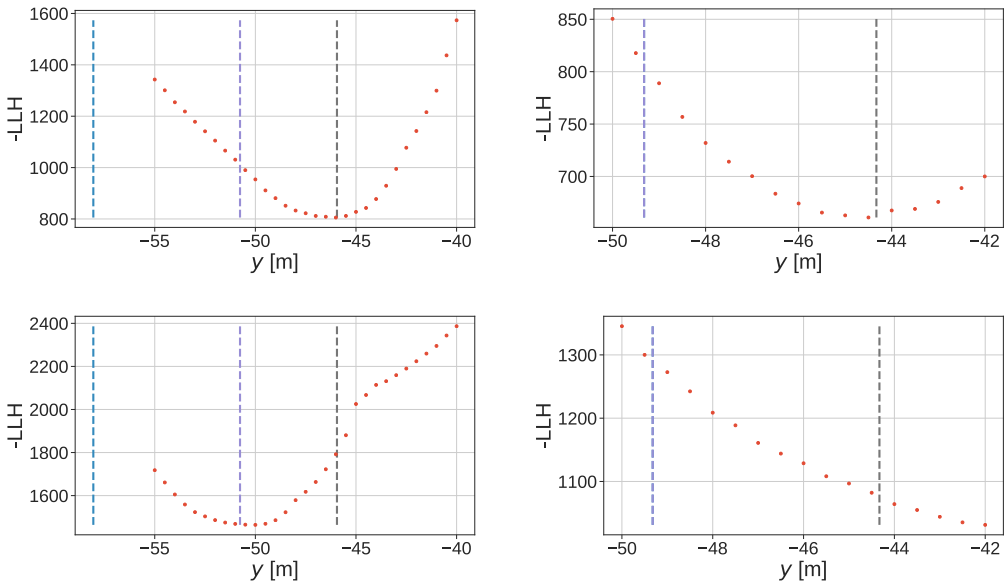

Figure C.2: Likelihood scans on two events that have been reconstructed using DirectReco with an oversampling of 1000. The scan points are the red, the initial seed is the blue dashed line and the purple dashed line is the reconstructed y, with the gray dashed line being the truth. **Top:** Shows the scan of two events on the left and right, where the other parameters were fixed at their truth values while scanning. **Bottom:** Shows the same two events but where the other parameters fixed at their final reconstructed values while scanning.

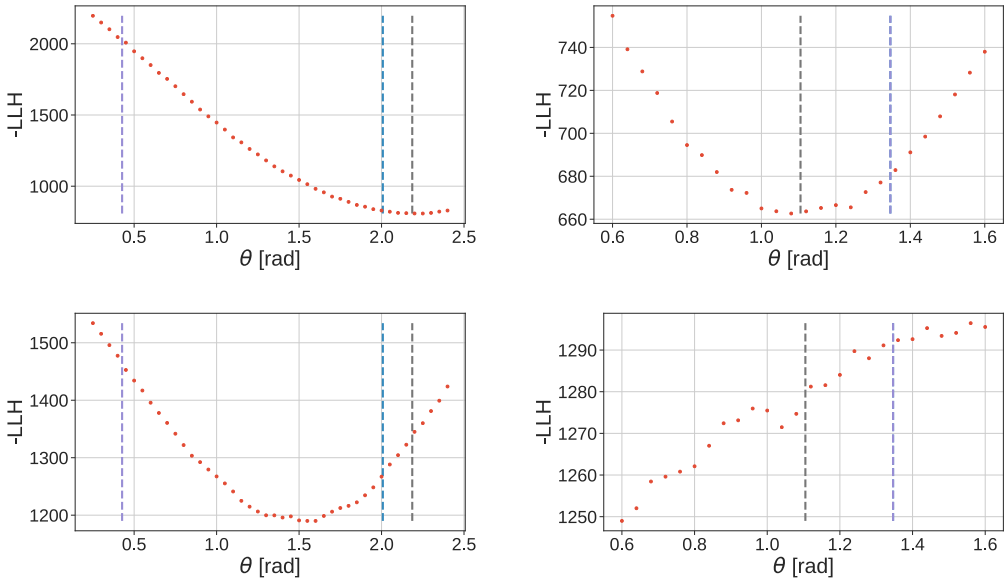

Figure C.3: Likelihood scans on two events that have been reconstructed using DirectReco with an oversampling of 1000. The scan points are the red, the initial seed is the blue dashed line and the purple dashed line is the reconstructed zenith, with the gray dashed line being the truth. **Top:** Shows the scan of two events on the left and right, where the other parameters were fixed at their truth values while scanning. **Bottom:** Shows the same two events but where the other parameters fixed at their final reconstructed values while scanning.

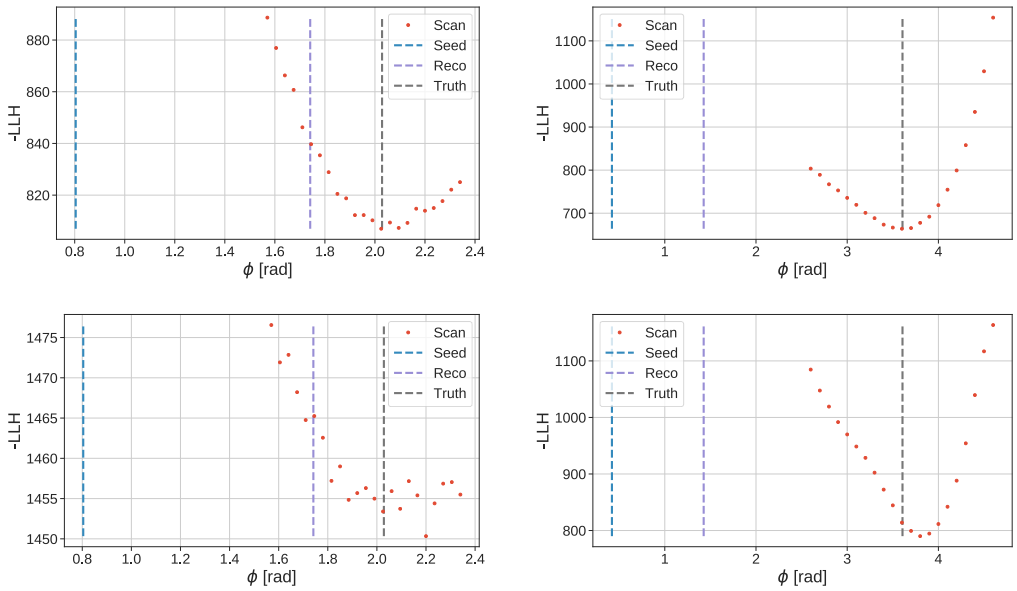

Figure C.4: Likelihood scans on two events that have been reconstructed using DirectReco with an oversampling of 1000. The scan points are the red ■, the initial seed is the blue ■ dashed line and the purple ■ dashed line is the reconstructed azimuth angle, with the gray ■ dashed line being the truth. **Top:** Shows the scan of two events on the left and right, where the other parameters were fixed at their truth values while scanning. **Bottom:** Shows the same two events but where the other parameters fixed at their final reconstructed values while scanning.

D Electron generation distributions

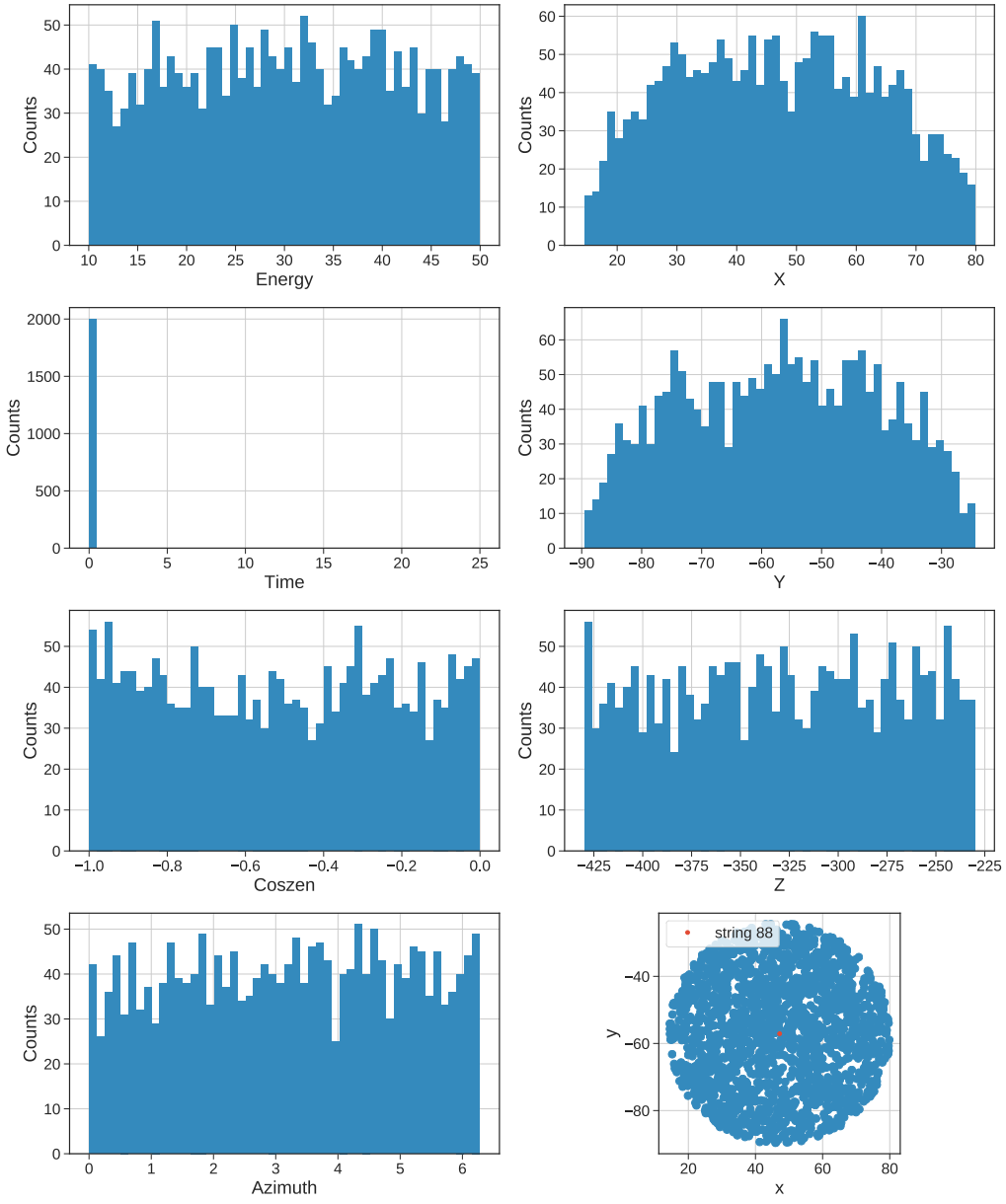

Figure D.1: The distributions of the generated events for the high statistic run. This is 2000 events of which 915 were reconstructed.

E Nmini dependence on truth and seed

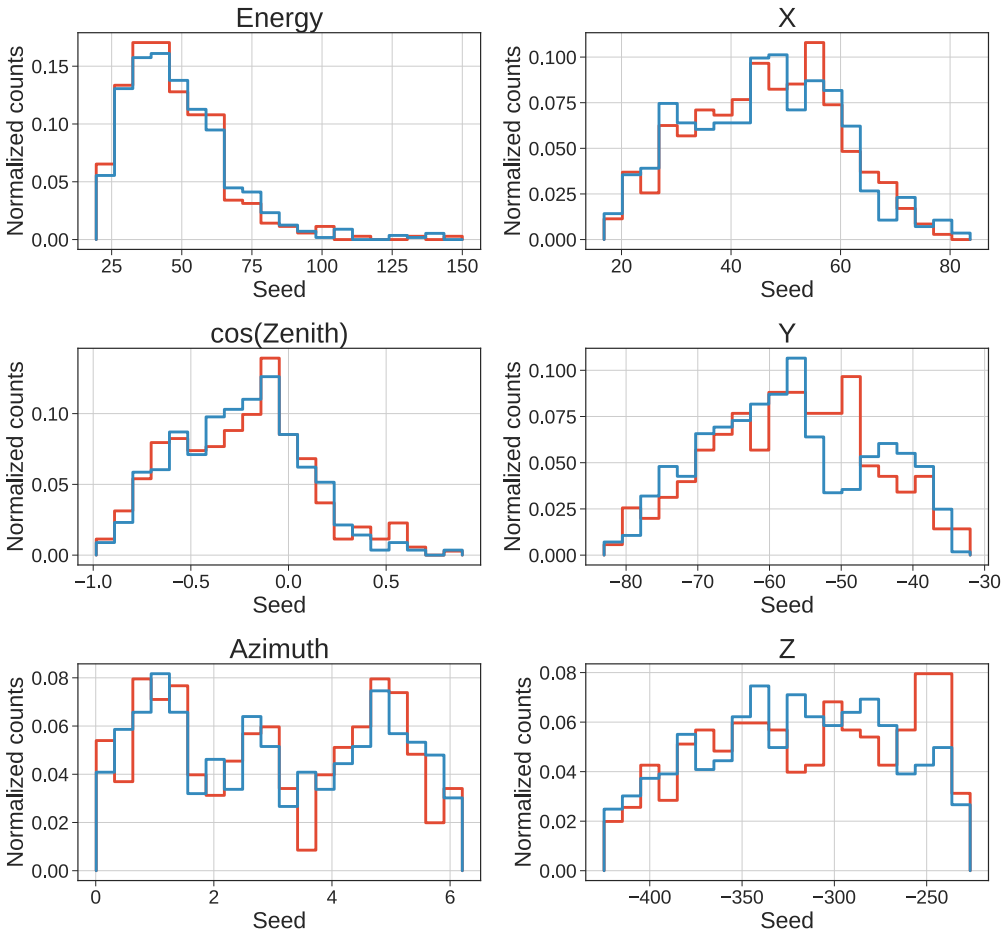

Figure E.1: The distribution of the 915 generated parameters used for the high statistics reconstruction. They are split between nmini ≤ 50 in blue and nmini > 50 in red

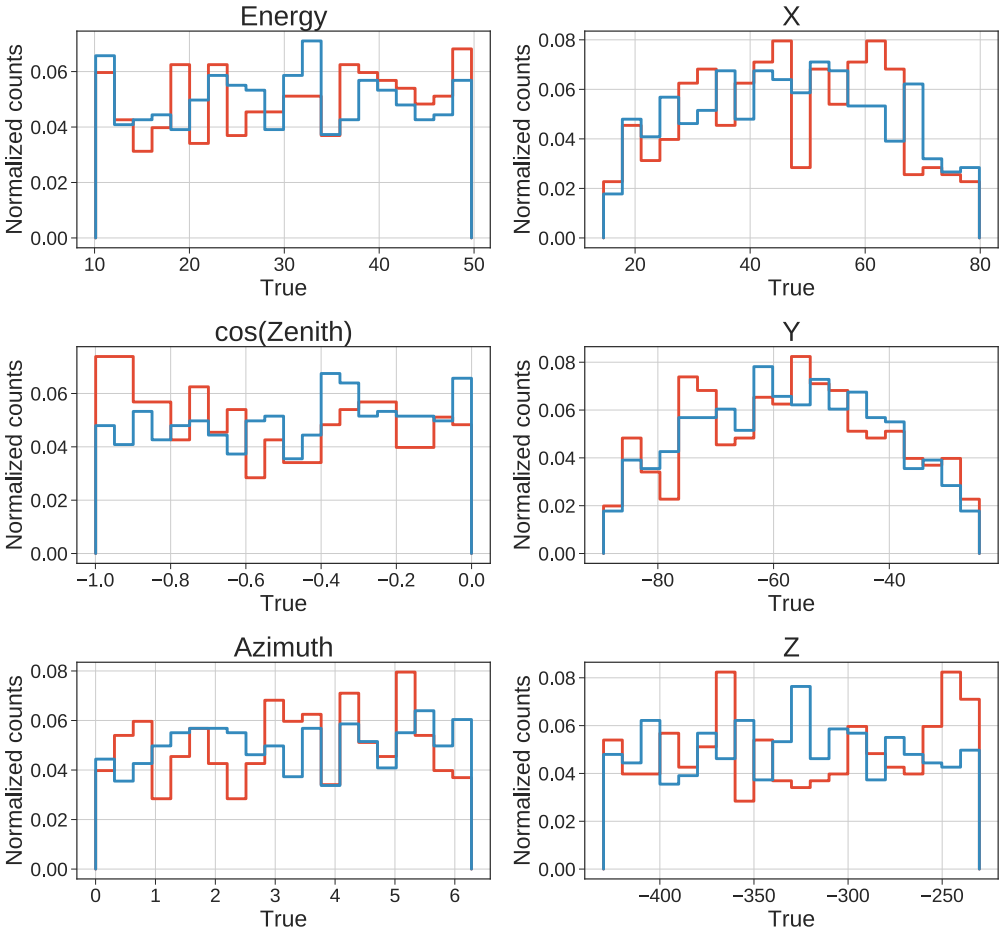

Figure E.2: The distribution of seeding of the 915 generated parameters used for the high statistics reconstruction. They are split between nmini ≤ 50 in blue and nmini > 50 in red

F Simulation diagram

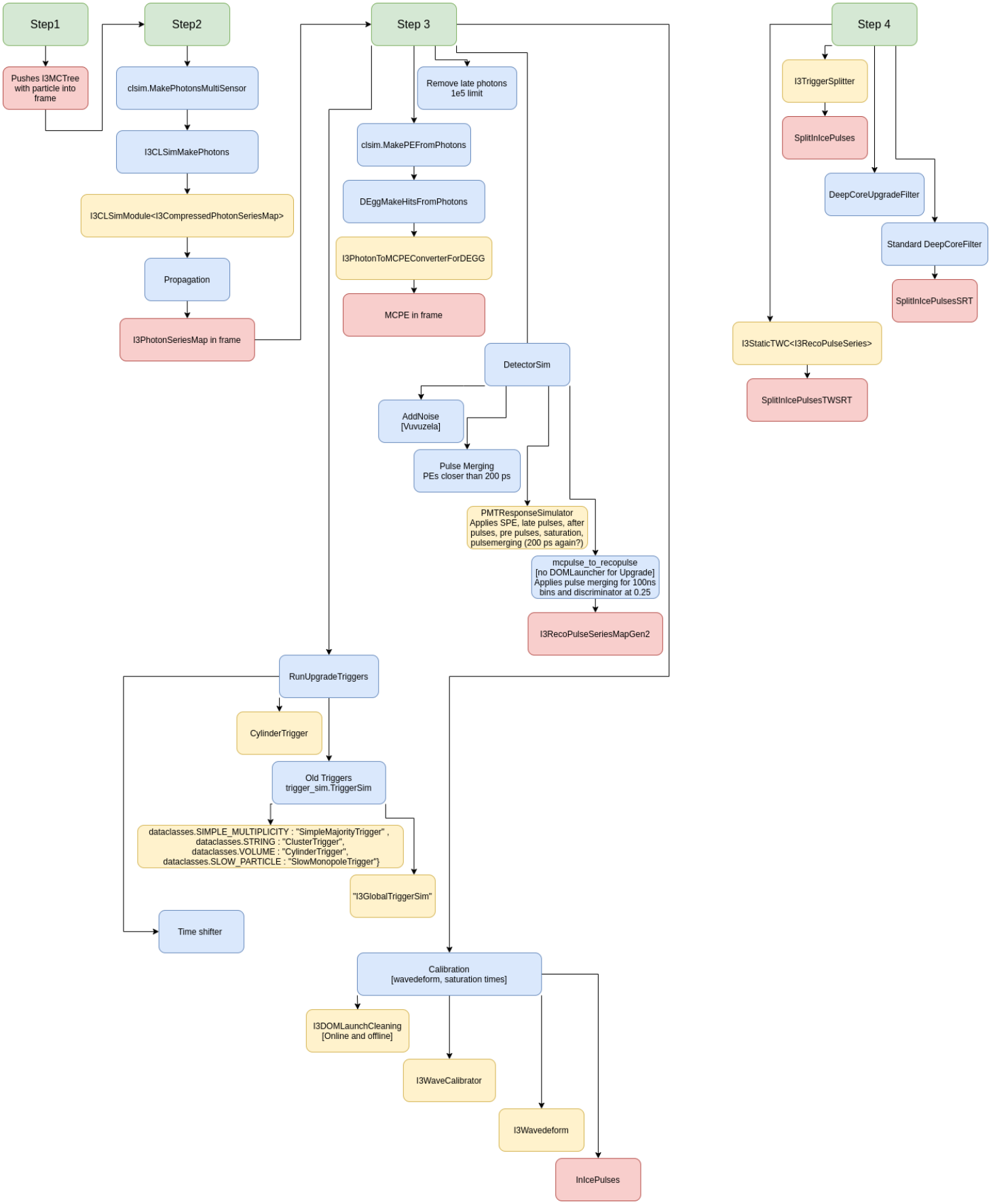

Figure F.1: The comprehensive diagram of the simulation chain used for this thesis. Arrows indicate which modules are called by which modules, while the vertical direction indicates in what order. When are step file is depleted in calls the next step file is called. Red indicates the object stored in frame, green the step functions, blue is python module and yellow is C++ module. This still does not include every object creation, but has most of the modules.